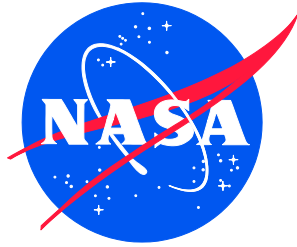# Application of Micro-Thruster Technology for Space Observatory Pointing Stability

Cornelius J. Dennehy/NESC
Langley Research Center, Hampton, Virginia

Aron A. Wolf
Jet Propulsion Laboratory, Pasadena, California

Andy Wu, and Richard Chiang
The Aerospace Corporation, El Segundo, California

Eric T. Stoneking
Goddard Space Flight Center, Beltsville, Maryland

John K. Ziemer
Jet Propulsion Laboratory, Pasadena, California

December 2020

NASA STI Program Report Series

Since its founding, NASA has been dedicated to the advancement of aeronautics and space science. The NASA scientific and technical information (STI) program plays a key part in helping NASA maintain this important role.

The NASA STI program operates under the auspices of the Agency Chief Information Officer. It collects, organizes, provides for archiving, and disseminates NASA's STI. The NASA STI program provides access to the NTRS Registered and its public interface, the NASA Technical Reports Server, thus providing one of the largest collections of aeronautical and space science STI in the world. Results are published in both non-NASA channels and by NASA in the NASA STI Report Series, which includes the following report types:

- TECHNICAL PUBLICATION. Reports of completed research or a major significant phase of research that present the results of NASA Programs and include extensive data or theoretical analysis. Includes compilations of significant scientific and technical data and information deemed to be of continuing reference value. NASA counterpart of peer-reviewed formal professional papers but has less stringent limitations on manuscript length and extent of graphic presentations.

- TECHNICAL MEMORANDUM. Scientific and technical findings that are preliminary or of specialized interest, e.g., quick release reports, working papers, and bibliographies that contain minimal annotation. Does not contain extensive analysis.

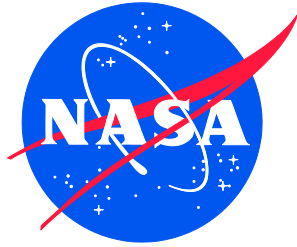- CONTRACTOR REPORT. Scientific and technical findings by NASA-sponsored contractors and grantees.

- CONFERENCE PUBLICATION. Collected papers from scientific and technical conferences, symposia, seminars, or other meetings sponsored or co-sponsored by NASA.

- SPECIAL PUBLICATION. Scientific, technical, or historical information from NASA programs, projects, and missions, often concerned with subjects having substantial public interest.

- TECHNICAL TRANSLATION. English-language translations of foreign scientific and technical material pertinent to NASA's mission.

Specialized services also include organizing and publishing research results, distributing specialized research announcements and feeds, providing information desk and personal search support, and enabling data exchange services.

For more information about the NASA STI program, see the following:

- Access the NASA STI program home page at http://www.sti.nasa.gov

- Help desk contact information:

https://www.sti.nasa.gov/sti-contact-form/
and select the "General" help request type.

NASA/TM–20205011556
NESC-RP-18-01375

Application of Micro-Thruster Technology for Space Observatory Pointing Stability

Cornelius J. Dennehy/NESC
Langley Research Center, Hampton, Virginia

Aron A. Wolf
Jet Propulsion Laboratory, Pasadena, California

Andy Wu, and Richard Chiang
The Aerospace Corporation, El Segundo, California

Eric T. Stoneking
Goddard Space Flight Center, Beltsville, Maryland

John K. Ziemer
Jet Propulsion Laboratory, Pasadena, California

December 2020

Acknowledgments

The assessment team thanks the following peer reviewers for their time and expertise: Oscar Alvarez-Salazar, Wayne Dellinger, Dan Dorney, Steve Gentz, Paul Mason, Jim O'Donnell, and John Spanos.

NASA Engineering and Safety Center
Technical Assessment Report

Application of Micro-Thruster Technology
for Space Observatory Pointing Stability

October 29, 2020

Report Approval and Revision History

NOTE: This document was approved at the October 29, 2020, NRB. This document was submitted to the NESC Director on November 5, 2020, for configuration control.

Approved:	_Original Signature on File – 11/5/2020_	
	NESC Director	Date

Version	Description of Revision	Office of Primary Responsibility	Effective Date
1.0	Initial Release	Cornelius J. Dennehy, NASA Technical Fellow for GN&C, GSFC	10/29/2020

Table of Contents

List of Figures

List of Tables

Technical Assessment Report

1.0 Notification and Authorization

This assessment was requested by the NASA Engineering and Safety Center (NESC) Guidance, Navigation, and Control (GN&C) Technical Discipline Team (TDT), which identified the topic as an unrecognized critical need for the Agency's future space science observatory-class space platforms. In 2017, the TDT identified a lack of understanding in the GN&C community of practice of micro-thruster technology application as a potential reaction wheel alternative for accomplishing observatory-class spacecraft fine pointing with low induced jitter. An initial low-fidelity feasibility study of the use of cold-gas micro-thrusters as a replacement for reaction wheels was performed in 2017 as a GN&C TDT discretionary activity [ref. 37]. The assessment documented in this final report was initiated in 2018 as a follow-on high-fidelity study with the principal focus of understanding the relative benefits of using cold gas and colloid micro-thrusters for precision observatory-class spacecraft attitude control functions. The beneficiaries of the work done in this assessment are future Science Mission Directorate (SMD) missions with demanding pointing stability requirements.

The key stakeholders for this assessment are the NASA SMD Chief Engineer, SMD Astrophysics Division leadership, and the teams generating architectures for future space observatory missions.

2.0   Signature Page

Submitted by:

Team Signature on File – 12/8/20

_____
Mr. Cornelius J. Dennehy   Date

Significant Contributors:

_____
Mr. Aron A. Wolf   Date

_____
Mr. Andy Wu   Date

_____
Dr. Richard Chiang   Date

_____
Mr. Eric T. Stoneking   Date

_____
Dr. John K. Ziemer   Date

Signatories declare the findings, observations, and NESC recommendations compiled in the report are factually based from data extracted from program/project documents, contractor reports, and open literature, and/or generated from independently conducted tests, analyses, and inspections.

3.0   Team List

Name	Discipline	Organization
Core Team		
Neil Dennehy	NESC Lead	NESC/GSFC
Aron Wolf	Technical Lead	JPL
Richard Chiang	GN&C Analyst	The Aerospace Corporation
Andy Wu	GN&C Analyst	The Aerospace Corporation
John Ziemer	Propulsion / Systems Analyst	JPL
Eric Stoneking	WFIRST GN&C Lead	GSFC
Consultants		
Brian Class	GN&C	Northrop Grumman Innovation Systems (NGIS)
Mike Hagopian	GN&C	Adnet Systems
Aaron Schutte	GN&C/Dynamics	JPL
Business Management		
Tricia Johnson	Program Analyst	LaRC/MTSO
Assessment Support		
Linda Burgess	Planning and Control Analyst	LaRC/AMA
Jenny DeVasher	Technical Editor	LaRC/AS&M
Melinda Meredith	Project Coordinator	LaRC/AMA

3.1   Acknowledgments

The assessment team thanks the following peer reviewers for their time and expertise: Oscar Alvarez-Salazar, Wayne Dellinger, Dan Dorney, Steve Gentz, Paul Mason, Jim O'Donnell, and John Spanos.

4.0   Executive Summary

Pointing repeatability and stability (i.e., jitter) requirements are key for space telescope missions of the future. Managing jitter is essential to being able to "image" planets on future exoplanet coronagraph missions. Jitter requirements for missions in this class are difficult to meet with current reaction wheel-based architectures. The reaction wheels are typically the largest pointing disturbance on the spacecraft. Disturbances from reaction wheels can be mitigated, typically by mechanically isolating the wheels, which imposes system complexity and cost.

Thrusters capable of thrust forces in the micronewton (μN) range (referred to as micro-thrusters or micronewton thrusters) have been developed to support the Laser Interferometer Space Antenna (LISA) mission, which requires drag-free control to place a test mass in near-perfect free-fall [ref. 1]. LISA continues to develop micro-thruster technology with the main objective of increasing reliability and extending lifetime to meet mission requirements (a 4-year baseline with a planned 6-year extension). Beyond the drag-free control application, micro-thrusters could be used as a substitute for reaction wheels or as a supplement to wheels for fine pointing control. Used in this fashion, micro-thrusters have potential for reducing the cost and technical risks of achieving demanding pointing stability performance on observatory-class missions. Use of micro-thrusters has also been suggested for other applications (e.g., precision formation flying/constellation maintenance and precision orbit maintenance). This assessment includes some preliminary analysis on the use of micro-thrusters for formation flying; however, the principal focus is on pointing stability.

Micro-thrusters come in different varieties, using different types of propellant. This assessment is focused on the following types, both of which have flown in space:

- **Cold-gas micro-thrusters**, using a precision piezoelectric valve for fine flow-rate control.

- **Colloid micro-thrusters**, a type of electrospray thrusters that apply a high electric potential difference to a conductive charged liquid at the end of a hollow needle emitter in such a way that a stream of charged droplets is accelerated to generate thrust.

Cold gas micro-thrusters designed by Leonardo S.p.A (formerly Finmeccanica) have been used for attitude control and fine pointing on three recent European Space Agency (ESA) missions: Microscope [ref. 10], Space Technology 7 (ST7)/LISA Pathfinder (LPF) [refs. 1, 23], and the Global Astrometric Interferometer for Astrophysics (Gaia) [refs. 18, 22]. Colloid micro-thrusters have also flown on LPF as part of NASA's technology demonstration payload ST7 [ref. 1]. On Gaia, micro-thrusters were used for fine pointing and spin-rate management. The Microscope and ST7/LPF missions used micro-thrusters for drag-free propulsion to "fly" the spacecraft around test masses, while these masses were in free-fall. LPF demonstrated Leonardo cold-gas micro-thrusters as part of ESA's LISA Technology Package, and colloid micro-thrusters developed by Busek Co. under NASA sponsorship as part of the Disturbance Reduction System (DRS) [ref. 4].

In 2017, a preliminary feasibility study [ref. 37] conducted by the NESC Guidance, Navigation, and Control (GN&C) Technical Discipline Team (TDT) showed improved jitter performance with cold-gas micro-thrusters in simulations of a large, observatory-class spacecraft. However, an accurate assessment of the potential benefits of micro-thrusters required higher-fidelity modeling and simulation of pointing noise sources.

The objective of this assessment was to assess the benefits of micro-thrusters for application on fine-pointing space observatory missions for fine pointing, in comparison to traditional architectures using reaction wheels alone. Therefore, higher-fidelity modeling of system performance was the primary focus. This work improved modeling fidelity and studied architectures, examined multiple mission application use cases, and addressed trades per the technical recommendations and feedback received on the initial 2017 feasibility study results. The scope of this assessment did not include mass or power trades of micro-thrusters vs. reaction wheels, which are to a great extent dependent on individual system implementation.

To achieve the objective, the simulation originally built by The Aerospace Corporation (Aerospace) for the 2017 preliminary feasibility study was augmented with high-fidelity disturbance models for reaction wheels and micro-thrusters. The high-fidelity simulation was used to perform a variety of scenarios representative of operational modes of space observatory missions. Flex-mode models of two representative spacecraft were obtained and used in the simulations.

In summary, the high-fidelity simulations conducted in this assessment found that using cold-gas or colloid micro-thrusters as the sole method of control actuation improves fine pointing performance by roughly an order of magnitude compared with the Hubble Space Telescope (HST), which uses reaction wheels for attitude control with carefully designed mechanical isolation. Performance using micro-thrusters was found to be roughly two orders of magnitude better than a wheels-only system without mechanical isolation. Future multi-year astronomy and astrophysics missions requiring precision pointing stability may need microthrusters with higher maximum thrust level, longer lifetimes, and higher bandwidth than have been demonstrated on-orbit to date. The simulation developed in this assessment is available for use NASA-wide.

5.0   Assessment Plan

The assessment plan had two main phases:

- Upgrade and augmentation of the Aerospace simulation built for the 2017 NESC GN&C TDT preliminary feasibility study, including:
    - Higher-fidelity modeling of reaction wheel disturbances.
    - Modeling of colloid micro-thrusters (including disturbances).
    - Modeling of reaction wheels and micro-thrusters operating simultaneously, including during shutdown of wheels and transition from wheels to micro-thrusters.
    - Modeling of spacecraft flexible body dynamics.
- Simulation studies.

Detailed descriptions of each are provided in the following paragraphs.

Simulation upgrade/augmentation. The Aerospace simulation was augmented with the reaction wheel disturbance model proposed by Rebecca A. Masterson as part of her thesis, described in Section 7.1.2.2 [ref. 6]. This was the only complete and detailed reaction wheel noise model the assessment team could find available in the public domain. All other models the team was aware of were restricted due to proprietary information concerns.

The simulation was upgraded to model operation of reaction wheels and thrusters simultaneously, allowing modeling of the transition from wheels to thrusters, including momentum dumping.

Upgrades included the addition of the Busek colloid micro-thruster model described in Section 7.1.3.8, provided by John Ziemer of the Jet Propulsion Laboratory (JPL), who led the development of colloidal micro-thrusters for ST7 and LISA. The colloid micro-thruster model was taken from JPL's performance model, which has been verified by on-orbit measurements [ref. 9]. The model includes the Busek micro-thruster control algorithm [ref. 1] with representative time response characteristics and noise models for the current, voltage, and thrust they produce. The control algorithm was developed for LISA with a low-noise bandwidth of 0.03 to 1 hertz (Hz), and a control cycle of 10 Hz.

This assessment planned to leverage work separately funded by LISA to test Busek colloid thrusters, with the goal of obtaining data at frequencies to 1000 Hz to augment the existing noise model. This was of interest to the Habitable Exoplanet Observatory (HabEx) concept study team, to assess the contribution of the thrusters to jitter at high frequencies. However, limitations of the testing instrumentation prevented gathering useful data above ~500 Hz. Measurements of thrust noise at frequencies up to 500 Hz showed levels at or below the previously measured noise from 0.01 to 5 Hz. Therefore, this higher frequency noise was not added to the simulation.

Inquiries were made to ascertain the availability of a higher-fidelity noise model for cold-gas micro-thrusters flown on ESA missions. The highest fidelity model found was incorporated into the Aerospace simulation and used in the NESC GN&C TDT preliminary 2017 study. Consequently, no upgrade was accomplished for the cold-gas thruster noise model.

To explore the effects of interaction between reaction wheel noise and spacecraft flexibility, the assessment team planned to obtain a flexible body dynamics model based on a modal representation (flexible mode model) of at least one representative observatory-class spacecraft. The team succeeded in obtaining flex-modes models from the both the Large Ultraviolet (UV)/Optical/Infrared (IR) Surveyor (LUVOIR) concept study team and the Nancy Grace Roman Space Telescope project (formerly identified as the Wide Field Infrared Survey Telescope (WFIRST). LUVOIR and The Roman Space Telescope are illustrative of different spacecraft sizes and morphologies. The mass of LUVOIR is roughly 35,000 kg, and the Roman Space Telescope mass is roughly 7,400 kg (see also Tables 7.1-1 and 7.1-3). LUVOIR has a shape representative of a spacecraft class, dominated by a telescope with a segmented mirror and a sunshade (see Figure 7.1-1). The Roman Space Telescope is a "barrel-shaped telescope," roughly similar in shape to the HST and other observatories (see Figure 7.1-4). The availability of these two flex-mode models enabled the team to use simulation to explore the response and behavior of different vehicle scales and shapes.

The LUVOIR concept study provided the assessment team with a finite element model (FEM) of the 15 m-aperture LUVOIR concept vehicle. In a planned collaboration, the team working NESC assessment TI-18-01312, Flexible Multibody Dynamics Modeling for Space Vehicles, used its toolset and methodology to create a GN&C flex-modes model from the LUVOIR FEM.

The implementation of the LUVOIR and the Roman Space Telescope flex-mode models was not identical to that of the LUVOIR concept study team or the Roman Space Telescope project, and was not intended or expected to produce identical performance. Differences included, but were not limited to:

- Reaction wheels and reaction wheel disturbance model.
- Controllers.
- Micro-thrusters, which are not used on either spacecraft.

Consequently, for the remainder of this report, the LUVOIR-like spacecraft model with a segmented mirror is referred to as "Observatory 1," and the barrel-shaped Roman Space Telescope-like spacecraft model is referred to as "Observatory 2."

Simulation studies. The simulation was used to study the following topics of interest to stakeholders:

- Sensitivity analyses investigating comparative benefits of micro-thrusters for spacecraft of different size and scale. This topic was of primary interest to the SMD Astrophysics Division and was the motivation for pursuing the two flex-modes models discussed above.

- Potential benefits of continuous wheel momentum management using micro-thrusters. Continuous operation of micro-thrusters and wheels should allow the wheels to operate within a narrow revolutions per minute (RPM) range selected for low wheel noise. Continuous momentum management should increase the time available for uninterrupted science observations since there should be no need to disrupt fine pointing for momentum unloading.

- Impact on pointing performance and science observing time of transitioning from reaction wheels to micro-thrusters (e.g., after a slew).

- Comparison of performance on cold-gas micro-thrusters, colloid micro-thrusters, and reaction wheels for science observations.

- Potential benefits of micro-thrusters for formation flight of a primary spacecraft with a secondary spacecraft (e.g., a Starshade) using micro-thrusters, including effects of small accelerations from micro-thruster firings and the effectiveness of micro-thrusters for formation flight.

Schedule. This task successfully absorbed two significant delays due to factors beyond its control with no increase in funding. The first was a 91-day delay due to the December 2018–January 2019 government shutdown and its extended ramifications, which affected finalizing contracting arrangements with Aerospace. The assessment team had planned for Aerospace to be on contract by December 17, 2018. The shutdown started December 22, further complicating plans. The second major delay was necessary to resolve issues Aerospace team members were able to identify with the flex-modes model received from the Roman Space Telescope project. This resulted in delivery of a revised model and an internal re-assessment of the project's model checking processes. This delay lasted 109 days. During these delay periods, the team was able to stand down to conserve funds. Table 5.1-1 shows the original schedule, the revised schedule at the March 25, 2019, kickoff, and completion dates of various milestones.

Table 5.1-1: Task Schedule (Original, Revised at Kickoff, and Completed)

	Original schedule				Revised schedule at kickoff			Actual completion	Comments
	Start date	End date	DT (days)		Start date	End date	DT (days)		
Request received by NESC	7/9/18				7/9/18			7/9/18	
NRB - initiai evaluation presented	7/12/18				7/12/18			7/12/18	
NRB - approval to proceed	7/12/18				7/12/18			7/12/18	
NRB - plan approval	11/15/18				11/15/18			11/15/18	
Technical assessment									
Stakeholder planning meetings	8/1/18	10/31/18	91.0		8/1/18	10/31/18	91.0	10/31/18	
Model aggregation	**12/3/18**	**3/29/19**			**3/18/19**	**6/28/19**		**8/5/19**	
Reaction wheel disturbance models								7/8/19	
Reaction wheel disturbance models	12/3/18	2/15/19	74.0		3/18/19	5/31/19	74.0	8/5/19	
Implementation of GNC flex mode model	1/14/19	3/29/19	74.0		4/15/19	6/28/19	74.0	7/8/19	
Thruster testing and noise model development	1/28/19	2/15/19	18.0		4/29/19	5/17/19	18.0	??	
On contract with Aerospace	12/17/18				3/18/19			3/18/19	91-day delay due to govt shutdov
Kickoff	12/17/18				3/25/19			3/28/19	
Simulation Architecture TIM	1/8/19				4/15/19			4/15/19	
Model Integration	2/19/19	3/29/19	38.0		5/21/19	6/28/19		8/5/19	
Incremental Progress Reports (contributions to final report)									
Initial simulation checkout and validation	4/1/19	5/17/19	46.0		7/1/19	8/16/19			
S/C jitter performance simuylation studies	5/20/19	8/16/19	88.0		8/19/19	11/15/19			
Midterm review	6/17/19				9/16/19			10/4/19	
First indication of issues with WFIRST lex-modes model								11/1/19	109-day delay to resolve issues v
Revised WFIRST model received								1/11/20	
WFIRST model required mods & checkout complete								2/18/20	
Team review of draft Aerospace rept w/completed WFIRST cases								4/20/20	
Peer review of final report	9/3/19				12/3/19			tbd	
Export control review of final report	9/3/19				12/3/19			tbd	
NRB - approval of final report	9/19/19				12/19/19			tbd	
Stakeholder briefing to customer	9/25/19				12/25/19			tbd	

6.0   Problem Description and Background

The trend in astrophysics observatory missions is toward tighter and more demanding requirements for pointing stability and jitter management. Managing and mitigating jitter has proved costly to past projects, necessitating the formation of dedicated teams of specialists. More challenging jitter requirements require higher model fidelity, more detailed error budgets, and more attention to the identification of error sources. Microvibration is a system-level problem. The tougher the requirements, the stronger the inter-subsystem dependencies, and the harder it becomes to solve a problem inside a single subsystem. The project team working on

microvibration requirements can drive system-level design, architecture, and testing, which can impact technical content, cost, and schedule. Table 6.0-1, taken from Reference 11, shows how increasingly demanding pointing stability requirements can drive design decisions and complexity.

Table 6.0-1: Rules of Thumb for Design of Fine-Pointing Spacecraft

Case	Stability/ Accuracy/ Reconstruction (arc-seconds, 1-σ)	Keys/Drivers to Micro-Vibration Design					
		Architecture	Model/ Simulation	ACS	Structural	Instrument Control	Testing
1	100 ++	ACS	Low Fidelity	HW	Low Freq modal	Functional	Interfaces @ I&T
2	10 → 100	Thermal & ACS	Low Freq & Fidelity	HW, CSI	Mid Freq Modal	Functional	Subsystem V&V @ I&T
3	0.1 → 10	Thermal, ACS & Jitter	Med. Freq & Fidelity, @ PDR	HW, CSI	Mid Freq Modal + Asymptotes	Functional + Compensation	Subsystem V&V @ I&T
4	0.01 → 0.1	Thermal, ACS & Jitter	High Freq & Fidelity @ PDR	HW, CSI Operational	High Freq Modal + Asymptotes	Functional + Compensation	Subsystem @ I&T, Component @ CDR
5	$1e^{-3} \rightarrow 1e^{-2}$	Calibration Thermal, ACS & Jitter	High Freq & Fidelity @ SRR	HW, CSI, Operational, algorithms	High Freq Modal + Tailoring	Functional + distributed Control	System @ I&T, Subsystem @ CDR
6	$1e^{-4} \rightarrow 1e^{-3}$	Calibration Thermal, ACS & Jitter	High Freq & Fidelity @ SRR	HW, CSI Operational, algorithms	High Freq Modal + Tailoring	Functional + distributed Control	System @ I&T, Subsystem @ CDR

Known Designs	Drives System	State of the Art	Beyond State of the art → Risk

Passive mitigation measures are generally preferable to active jitter suppression. These can include avoiding microvibration-producing events during science observations when possible, or momentum management of reaction wheels to avoid specific wheel speed ranges producing undesired structural modes.

If passive measures are not sufficient to meet the requirement, other actions can be taken to improve the performance of microvibration sources. Balancing of reaction wheels can be improved, the frequency content of forcing functions of other input sources can be changed to avoid problem modes, or problem modes can be shifted in frequency by tailoring structural dynamics (e.g., adding isolation or stiffness control at critical interfaces). Adjustable and swappable structural mount components can be added at critical interfaces to tune jitter modes, or tuning masses or mass dampers can be added at critical response areas. The more difficult the jitter requirement is to meet, the more complex the implementation of a solution can become, increasing cost, technical risk, and schedule length.

The HST serves as a performance benchmark for a fine-pointing system using reaction wheels for attitude control. HST met a pointing stability requirement of 7 milliarcseconds (mas) over a period of 60 seconds to 24 hours [refs. 38, 39]. This falls in the second-to-last row of Table 6.0-1. This was accomplished by mechanically isolating the optical telescope assembly from the outer body on which the wheels and other active mechanical devices were mounted. Before launch, all active components were individually tested and modified as required to suppress

potential sources of vibration. A system-level jitter test was performed in which the spacecraft was suspended from an isolating air bag and all active components were exercised.

The Roman Space Telescope has also baselined reaction wheels for Attitude Control System (ACS) with a total pointing stability requirement of 14 mas, which, interestingly, is double that of HST.

Over the past few decades, pointing stability and jitter requirements for astrophysics missions have become more demanding as goals and objectives grew more ambitious. This trend is expected to continue. Pointing stability requirements for the four recent NASA astrophysics mission concepts studies (HaBeX, LUVOIR, Origins Space Telescope (OST), and the Lynx X-ray Observatory) all fall in the range shown in the last row of Table 6.0-1, essentially challenging the current state of the art. Because reaction wheels can be a significant and sometimes dominant source of microvibration, finding a substitute control actuator that can meet the requirements of a fine-pointing control system and produce significantly less disturbance at reduced system complexity and cost is highly desirable. Micro-thrusters show potential to fill this need.

As discussed, cold-gas and colloid micro-thrusters have flown in space. The ST7 LPF mission demonstrated both micro-thruster types: cold-gas thrusters developed by Leonardo were part of ESA's LISA Technology Package flown on that mission, and colloid micro-thrusters developed by Busek Co. were part of NASA's ST7 DRS. The ST7 colloid micro-thrusters operated for more than 2,400 hours (100 days) in flight during commissioning activities, a 90-day experiment and the extended mission. This mission was the first validated demonstration of electrospray thrusters in space, providing precision spacecraft control and drag-free operation in a flight environment with applications to future gravitational wave observatories like LISA. LISA continues to develop colloid micro-thrusters to meet its 10-year mission lifetime requirement.

Retiring reaction wheels allows mission architects to bypass the use of isolation and other mitigation approaches involving structural design modifications or adaptations to avoid undesired resonant structural modes. This reduces the associated system engineering effort and cost and affords structural designers more flexibility. In addition, micro-thrusters allow on-orbit modifications to system-level response and behavior by modifying a control algorithm, while modifications to isolators and similar systems are difficult or impossible to implement in flight.

It is possible to envision the use of micro-thrusters in several operating scenarios:

1. **Reaction wheels are used for large slews, but spun down during science observations, with micro-thrusters used as the sole control actuator for fine pointing**. Any need to isolate the reaction wheels is eliminated because the wheels are shut down during fine pointing.

2. **Traditional reaction control system (RCS) thrusters (hydrazine or biprop) are used for large slews, with micro-thrusters used as the sole control actuator for fine pointing**. HaBeX is baselining this architecture.

3. **Reaction wheels are used for large slews, with frequent large slews required, prohibiting the spinning down of the wheels**. Micro-thrusters are the sole control actuator while wheels are spinning at a quiet constant speed or in conjunction with wheels, with both actuators used simultaneously for fine pointing. This architecture could prove suitable for OST, which has an operational mode requiring frequent slews exceeding the control authority of micro-thrusters.

During the course of this study, the assessment team identified a relevant example of a spacecraft ACS architecture using micro-thrusters for precision control actuation in tandem with reaction wheels used for slews, but shut down during science observations. The team learned that the ESA Euclid spacecraft design is incorporating the Leonardo nitrogen cold-gas micro-thrusters for fine pointing during science observations, in a fashion similar to Scenario 1. Euclid is a cosmology mission dedicated to the investigation of the properties of dark energy and dark matter, and will operate in a quasi-halo orbit about the Sun-Earth L2 point [ref. 34]. The Euclid observatory's image quality requirements demand precise pointing and ultra-low jitter, while its sky survey requirements call for fast and accurate attitude slews. Euclid has a relative pointing error requirement of 75 mas (3-σ) normal to the instrument's boresight, a more than 700-second science observation period. The cold gas micro-thrusters, with their micronewton resolution, provide an appropriate level of attitude control actuation torque to maintain the observatory's fine pointing without introducing undesirable jitter. The micro-propulsion subsystem employed for fine attitude control has two redundant manifolds with six cold gas micro-thrusters in each. Four tanks provide storage for 70 kg of nitrogen, sufficient for 7 years' operation of the Euclid observatory with a nearly 100% margin. Four reaction wheels on the Euclid spacecraft execute all the attitude slews (i.e., 50 to 100 arcsec observational dithers, small field slews, and large attitude slews between different sky zones). After each slew maneuver, the reaction wheels are controlled to slow until friction stops their rotation. Maintaining the reaction wheels at rest during science observation periods ensures noise-free science exposures by eliminating the microvibration primarily associated with reaction wheel flywheel static, dynamics mass imbalances, and wheel bearing mechanical noise. The last, but critical, elements of the Euclid spacecraft ACS architecture are two redundant hydrazine RCS manifolds, each manifold comprising 10 20N thrusters used to unload momentum from the reaction wheels and execute observatory trajectory correction maneuvers [ref. 35].

Sections 6.1 and 6.2 present detail on the design and operation of existing colloid and cold-gas micro-thruster systems.

6.1   Busek Colloid Micronewton Thrusters (CMNT)

As mentioned above, these thrusters have flown as part of the ST7-DRS demonstration. Figure 6.1-1 shows a single ST7 colloid thruster emitter, a single thruster "head," and a thruster "cluster" as flown on ST7 with four heads [refs. 12, 13]. In the ST7-DRS configuration, a thruster head contains nine emitters.
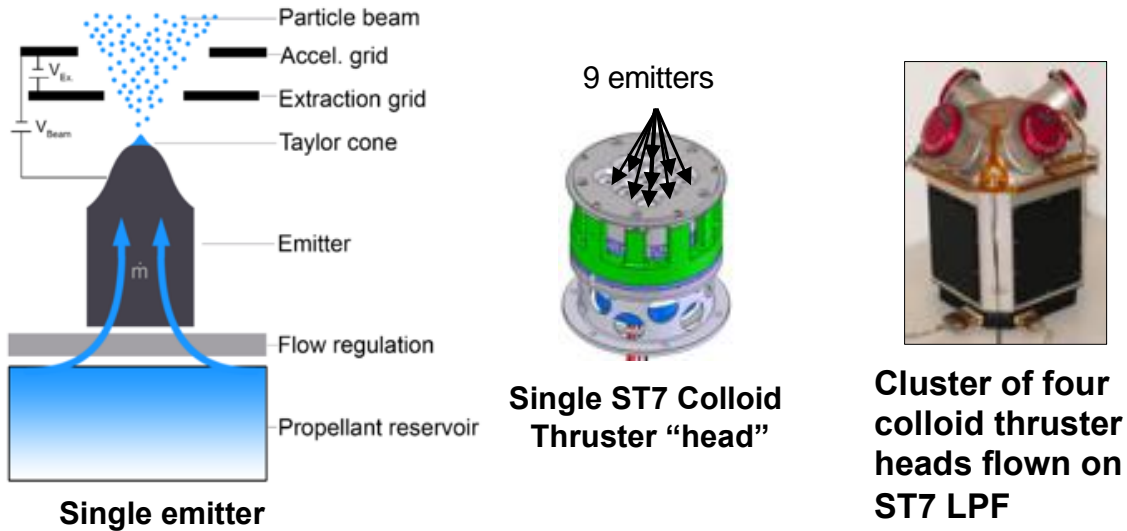

Single emitter

Single ST7 Colloid Thruster "head"

Cluster of four colloid thruster heads flown on ST7 LPF

Figure 6.1-1. Cluster of Four Colloid Thrusters Flown on ST7 LPF

The demonstrated performance of these thrusters is listed in Table 6.1-1 [ref. 1].

Table 6.1-1. Busek CMNT Specs

Top Level DRS Colloid Thruster Requirements and Delivered Performance

	Requirements	Demonstrated Performance
Thrust Range	T = 5-30 µN $(T_{max}/T_{min} = 6)$	T=5–35.8µN >36µN for short periods $(T_{max}/T_{min} \sim 7)$
Thrust Resolution and Adjustability	$\Delta T \leq 0.1$ µN	$\Delta T \sim 0.01$ µN
Thrust Noise	$\Delta T \leq 0.1$ µN in frequency interval of 1 to 4,000 mHz	$\Delta T \leq 0.01$ µN in frequency interval of 1 to 3,000mHz and $\Delta T \leq 0.1$ µN in frequency interval of 3,000 to 4,000mHz
Life and Starts	2,200 total operating hours 10 starts/stops	3,500 hours and hundreds of starts/stops
Specific Impulse	>150sec	240sec, 400sec possible under some ops conditions
Plume Half Angle	<35degrees, 95% of beam current	<23 degrees

The resolution of the colloid micro-thrusters is illustrated in Figure 6.1-2, which shows that these thrusters can be commanded to a resolution of 5 to 10 nanonewtons (nN).

Micro-Valve Resolution
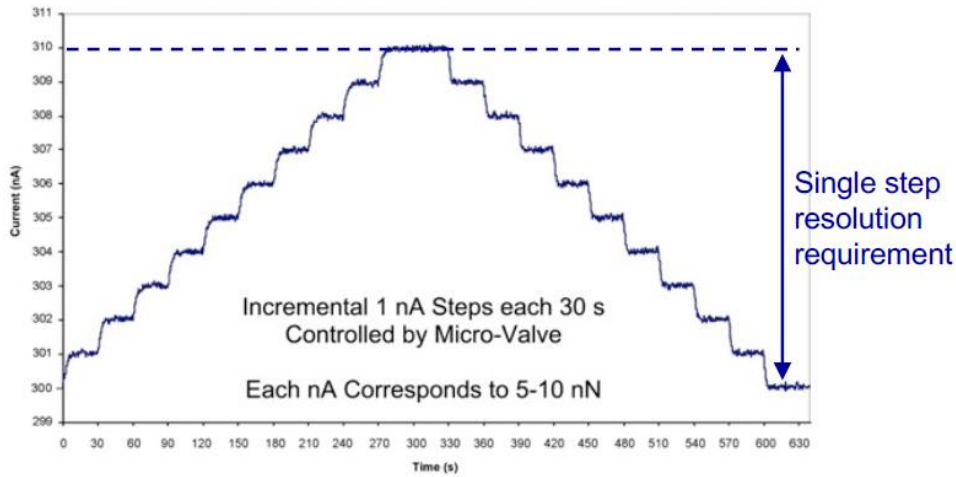
Figure 6.1-2. Busek CMNT Resolution

Figure 6.1-3 shows the power spectral density (PSD) of the colloid thruster noise level from 1 mHz to 5 Hz from direct current (DC) thrust commands of 5 and 30 μN. The noise level of the micro-thrusters is under 0.01 μN of thruster noise below 3 Hz, and under 0.1 μN of noise between 3 and 4 Hz. Thrust noise is calculated from measurements of beam current and voltage using a physics-based model of thruster performance that has been validated on orbit [ref. 9]. Busek has conducted more recent measurements of thrust noise based on beam current and voltage measurements at higher frequency, shown in Figure 6.1-4 [ref. 9]. Since the thrust noise did not significantly increase above 1 Hz, the response and noise of the system above the control bandwidth was not considered significant.
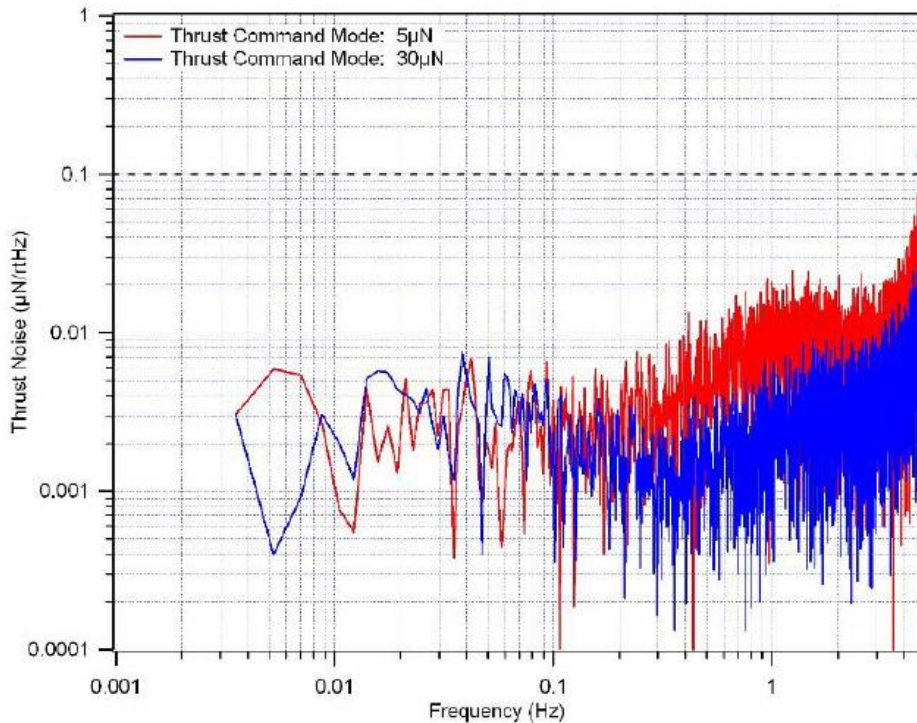
Figure 6.1-3. Busek CMNT Thrust Noise
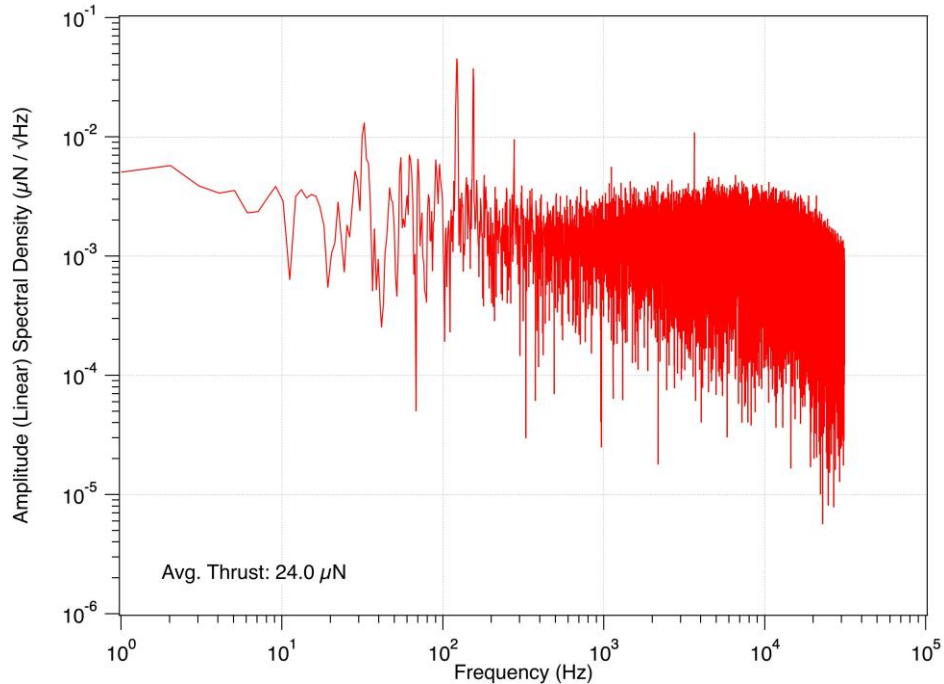
Figure 6.1-4. Colloid Micro-Thruster Thrust Noise from 1 Hz to 10 kHz
Note: Above 500 Hz, beam current electrometer circuitry may be interacting with power processing unit electronics, artificially affecting noise measurements. Data above 500 Hz should be considered.

6.2   Leonardo's Cold Gas Micro Propulsion System

No known commercial cold gas thruster system has the combined range and resolution of Leonardo's Cold Gas Micro Propulsion System [ref. 2]. The official data sheet is provided in Table 6.2-1, and an example thruster is shown in Figure 6.2-1 [ref. 37].

Table 6.2-1. Data Sheet for Leonardo Cold Gas Micro Propulsion System

Parameter	Value	Notes/Remarks
Operating Gas	N_2 (nominal)	Compatibility with He, Ar, Kr, Xe
Inlet Pressure (P_{IN})	• 310 bar, at BOL (Begin of Life) • 3 bar, at EOL (End of Life) • 4 bar, at EOL (End of Life) • 1 bar, 1,5 bar*	Max Operating Pressure (MEOP) at the high pressure MPFM inlet MEOP at the MTA inlet (GAIA, LISA Pathfinder, Microscope) * for EUCLID
Leakage	• $< 10^{-6}$ scc/s gaseous He (internal) • $< 10^{-7}$ scc/s gaseous He (external)	Referred to a single MT
Thrust Range	0 to 1000 μN	At P_{IN} = 1bar; commandable in 0.1 μN steps Thrust range extendable varying inlet pressure
Max thrust resolution	0.1 μN	
Thrust Accuracy	≈1% of thrust level	Referred to the thrust scale factor knowledge error
Mass Flow Range	0 to 100 scc/m	Gaseous N_2, for a single MT Mass flow range extendable up to 200 scc/m
Specific Impulse	> 50 sec at thrust ≥ 10 μN	For N_2
Thrust Noise	≈1 μN/√Hz from 0.01 Hz to 1 Hz and 0.045 μN/□Hz above 1 Hz	
Total Impulse	10000 Ns	For each thruster
Lifetime in orbit	> 5 years	No stopping factor for achieving a higher figure
Physical Properties (GAIA Like Configuration)	*Micro Thruster (MT)* • Mass: 390 g • Dimens.:184,3 x 62 x 52,5 each *Micro Propul. Feed Module (MPFM)* • Mass: 8 kg • Dimens.: 650 x 340 x 200 *Micro Propulsion Electronics (MPE)* • Mass: 4.9 kg • Dimens.: 250 x 150 x 120	with Cables approach based on a Mechanical Pressure Regulator. An Electronic Pressure Regulator is considered for future MPS product evolutions
Inlet filtration	2 μm	
Temperature Range	Operating: 0 to +50°C	Non-Operating: -30 to +60°C
Time response	250 ms@63% of the new commanded thrust level	at a command frequency of 4 Hz
On-off Cycles	>100000	demonstrated by test
Power Demand	8.4 W (idle), 22.1 W (max. operat.)	28 W (warm-up)

Figure 6.2-1. Leonardo Cold Gas Thruster

While most thrusters are designed with a solenoid valve that releases pressurized gas, which expands in the chamber and exits through a throat of constant cross-section, Leonardo's thruster valve is similar to a proportional valve in that it varies the throat cross-section to modulate the thrust. This description can be found in Reference 3:

> "The basic principle is that gas at constant pressure is fed to the thruster. This gas expands through a nozzle, thus creating a thrust. This thrust ought to be adjustable, and that action is performed using a needle that will let flow the needed quantity of gas, hence managing the thrust."

and

> *"The TV (thruster valve) is maintained normally closed using pre-load springs. Its throat section is adjusted with a needle to let flow the needed amount of gas. This needle is actuated by a stack of piezoelectric disks. Several disks compensate the spring load and are submitted to a constant voltage, V_{base}. Other disks regulate the needle displacement and are fed by an adjustable voltage, V_{reg}. The valve's nozzle is millimeters long and its throat diameter is around several hundreds of microns."*

Coupled with the 0.1 μN resolution and *0 to 1000 μN* thrust range is a very low noise profile (Figure 6.2-2). The profile in Figure 6.2-3 is provided as part of the same document that gives the data sheet [ref. 2].
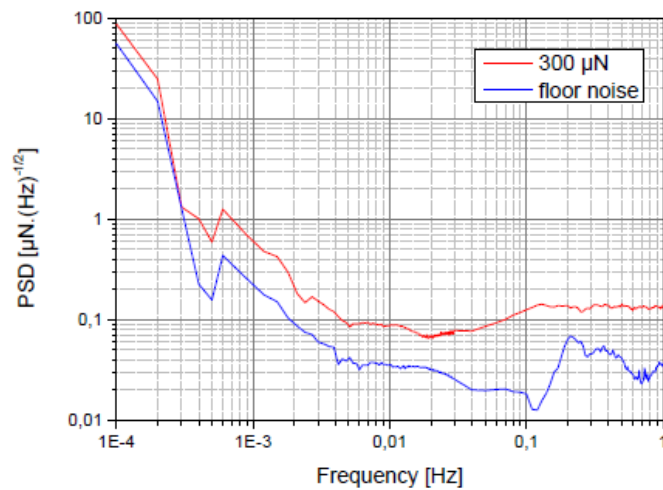
Figure 6.2-2. Thruster Noise
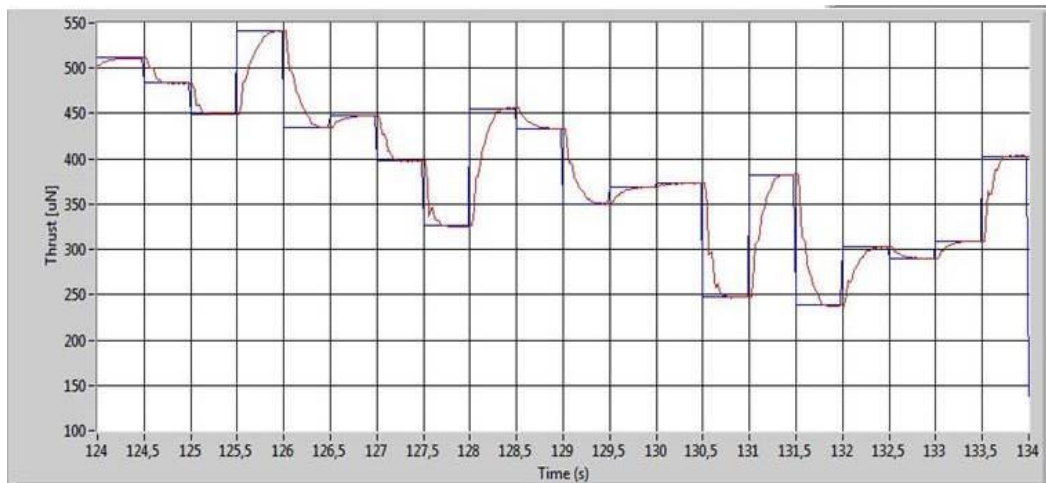
Figure 6.2-3. Thrust Profile from Leonardo

Finally, the thrusters were designed to comply with a response time requirement of 0.25 sec at 63% of the command thrust step in the thrust range from 0 to 1000 μN (Figure 6.2-1).

7.0 Data Analysis

7.1 Simulation Modeling and Design

A block diagram showing an overview of the simulation built and used in this assessment appears in Figure 7.1-1.
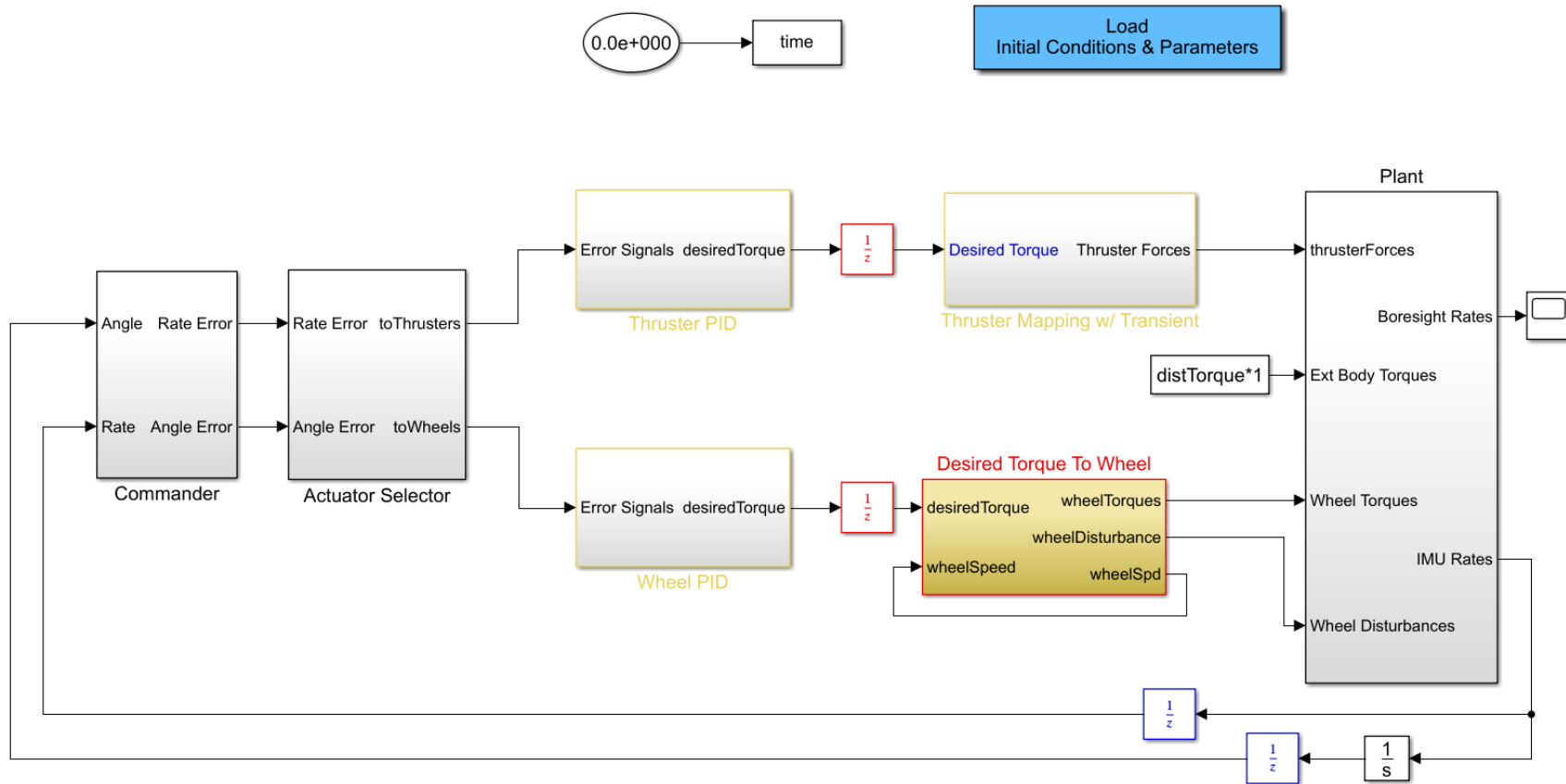
Figure 7.1-1. Overall Simulation Model

7.1.1 Candidate Reference Missions and Respective Environments

The assessment team considered two space observatory missions for the analysis: Observatory 1, a large spacecraft with a segmented mirror like LUVOIR or the James Webb Space Telescope; and Observatory 2, a barrel-shaped telescope spacecraft like the Roman Space Telescope or HST.

7.1.1.1 Observatory 1 Spacecraft Model

Observatory 1, shown in Figure 7.1-2, is a large L_2 NASA space observatory concept spacecraft. Its mass properties are provided in Table 7.1-1.
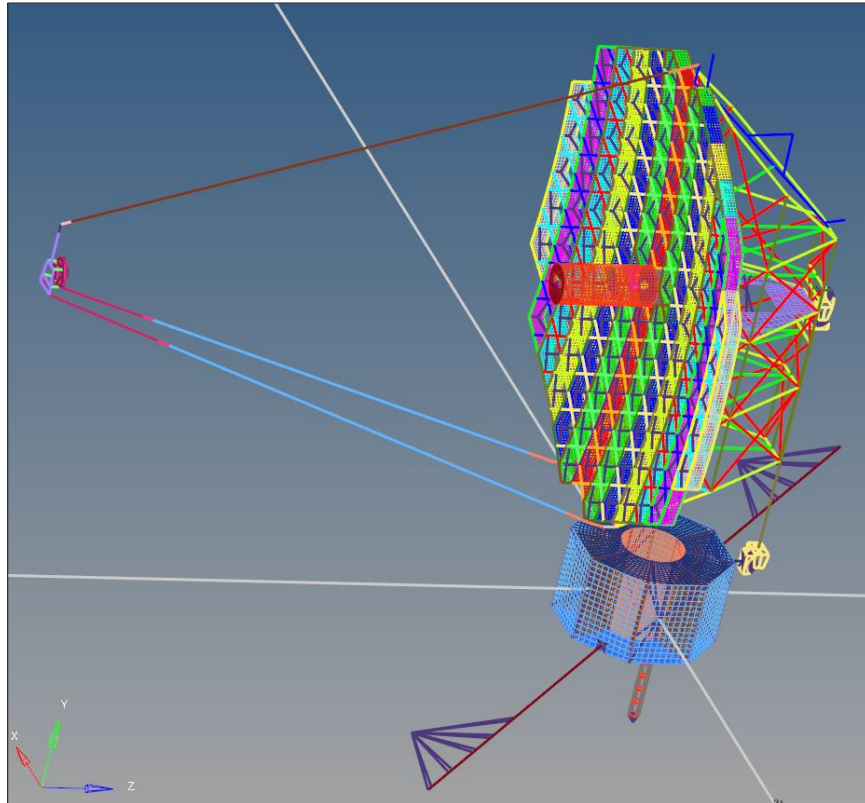
Figure 7.1-2. Observatory 1

Table 7.1-1. Observatory 1 Mass Properties

Mass [kg]	34711
Center of Mass from O, [m]	[0.0141, -3.5443, 1.4666]
Bus Moment of Inertias [I_{xx} ,I_{yy}, I_{zz}], [kg m^2]	[1498543, 912915, 1456938]
Bus Products of Inertia [I_{xy}, I_{xz}, I_{yz}], [kg m^2]	[5162, -26738, 112991]

For Observatory 1, the assessment team assumed 16 micro-thrusters with the location and thrust vectors specified in Table 7.1-2. The number of thrusters and their locations and thrust vector orientations were chosen to provide full three-axis control. The thruster configuration was not optimized or studied extensively in this assessment. However, an in-depth study would be an integral part of architecture for any future observatory mission and would be critical to ensure adequate control torques and control saturation.

Table 7.1-2. Observatory 1 Thruster Locations and Force Vectors

Thruster	Location from O, [m]	Force Vector
1	[0, -11.101, 0.062]	[-0.707 0.500 0.500]
2	[0, -11.101, 0.062]	[0.707 -0.500 0.500]
3	[-1.602, -11.101, 0.626]	[-0.146 0.500 0.854]
4	[-1.602, -11.101, 0.626]	[0.854 -0.500 -0.146]
5	[-2.266, -11.101, 2.328]	[0.500 0.500 0.707]
6	[-2.266, -11.101, 2.328]	[0.500 -0.500 -0.707]
7	[-1.602, -11.101, 3.930]	[0.854 0.500 0.146]
8	[-1.602, -11.101, 3.930]	[-0.146 -0.500 -0.854]
9	[0, -11.101, 4.594]	[0.707 0.500 -0.500]
10	[0, -11.101, 4.594]	[-0.707 -0.500 -0.500]
11	[1.602, -11.101, 3.930]	[0.146 0.500 -0.854]
12	[1.602, -11.101, 3.930]	[-0.854 -0.500 0.146]
13	[2.266, -9.138, 2.516]	[-0.500 0.500 -0.707]
14	[2.266, -9.138, 2.516]	[-0.500 -0.500 0.707]
15	[1.602, -11.101, 0.726]	[-0.854 0.500 -0.146]
16	[1.602, -11.101, 0.726]	[0.146 -0.500 0.854]

An example of thruster placement on the main bus is provided in Figure 7.1-3.
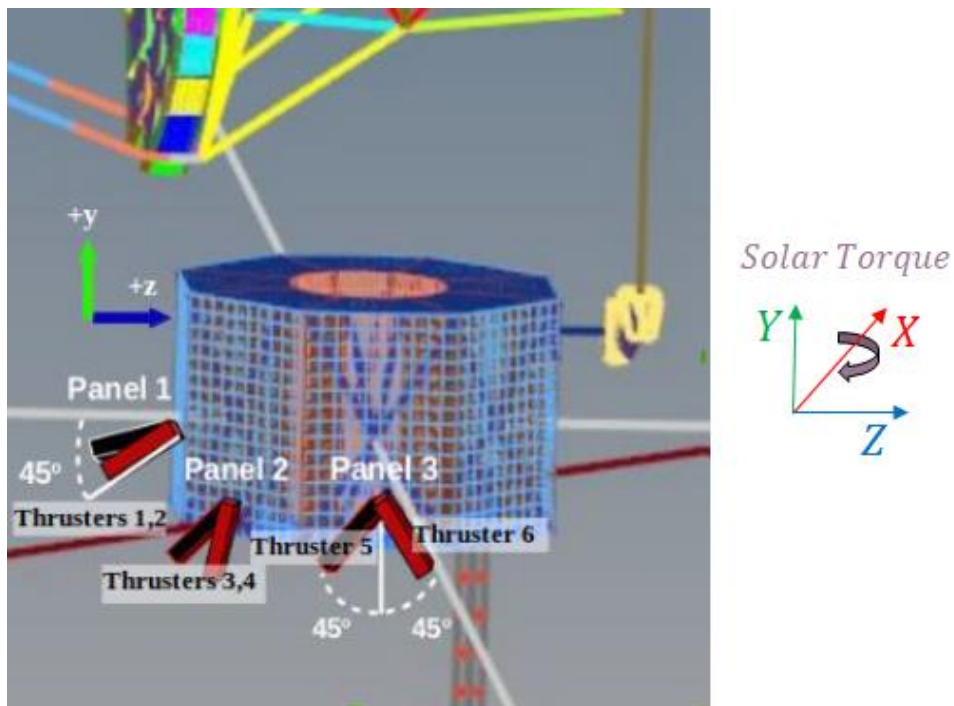
Figure 7.1-3. Example of Observatory 1 Thruster Location

Since Observatory 1 is in a Sun-Earth L$_2$ orbit, solar radiation pressure caused by solar wind is the only significant environmental disturbance. The disturbance torque on Observatory 1 caused by solar radiation was set to:

$$T_s = [1 \times 10^{-3}, 0, 0] \, N \cdot m$$

The Observatory 1 FEM used in this simulation was a 432-state flexible state-space model with a cutoff frequency of 15 Hz. To give a better idea of the flexible modes that exist in this FEM, Figure 7.1-4 shows the plot of the singular value of the frequency response from the 3-axis torque inputs to the output rates.
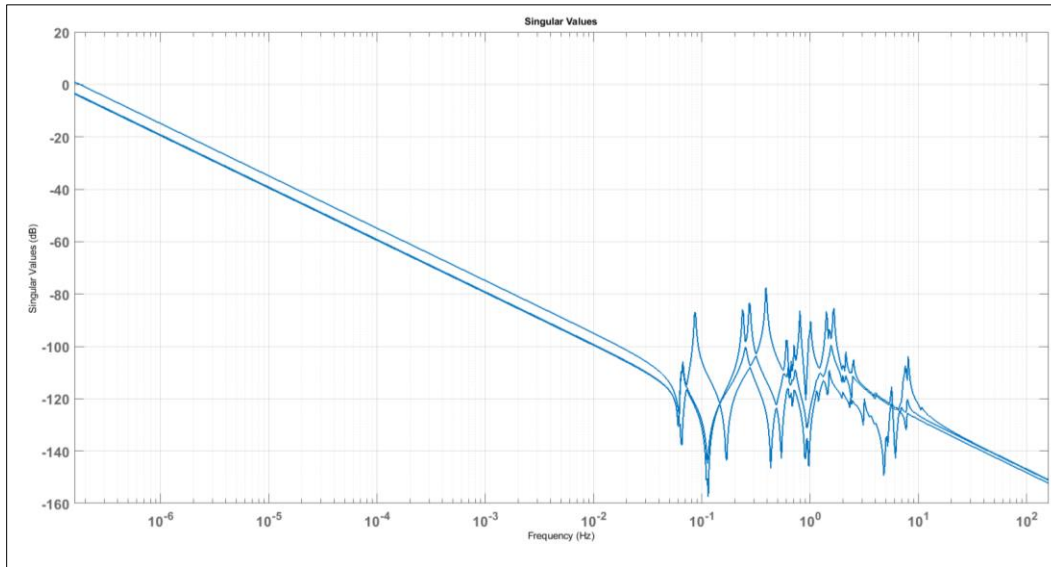
Figure 7.1-4. Singular Values of Observatory 1 Frequency Response

The spikes between 0.05 and 10 Hz are the flexible modes that exist in the FEM, which will present a challenge in the controller design.

7.1.1.2 Observatory 2 Spacecraft Model

Observatory 2, shown in Figure 7.1-5 [ref. 5], is an L_2 NASA space observatory and is considerably less massive than Observatory 1. Its mass properties are given in Table 7.1-3.

Figure 7.1-5. Observatory 2

Table 7.1-3. Observatory 2 Mass Properties

Mass, [kg]	7438.48
Center of Mass from O, [m]	[2.5969, 0.0293, 0.0180]
Moment of Inertias [I_{xx} ,I_{yy}, I_{zz}], [kg m^2]	[19030.95, 34895.87, 34809.16]
Products of Inertia [I_{xy}, I_{xz}, I_{yz}], [kg m^2]	[658.85, 914.83, -237.00]

The spacecraft has eight micro-thrusters used for attitude control. The thruster locations and thrust unit vectors are given in Table 7.1-4. Approximate locations of thrusters are shown in Figure 7.1-6.

Table 7.1-4. Observatory 2 Thruster Location and Force Direction

Thruster	Location from O (m)	Force Vector
1	[0.756, -1.075, -1.827]	[-0.574, 0.174, 0.801]
2	[0.756, 1.057, -1.829]	[-0.574, -0.174, 0.801]
3	[0.760, 0.931, 1.974]	[-0.588, -0.174, -0.624]
4	[0.760, -0.922, 1.962]	[-0.588, 0.174, -0.624]
5	[1.934, 0.931, 1.974]	[0.574, -0.174, -0.801]
6	[1.934, -0.923, 1.962]	[0.574, 0.174, -0.801]
7	[1.930, 1.049, -1.830]	[0.559, -0.174, 0.657]
8	[1.947, -1.075, -1.827]	[0.559 0.174, 0.657]
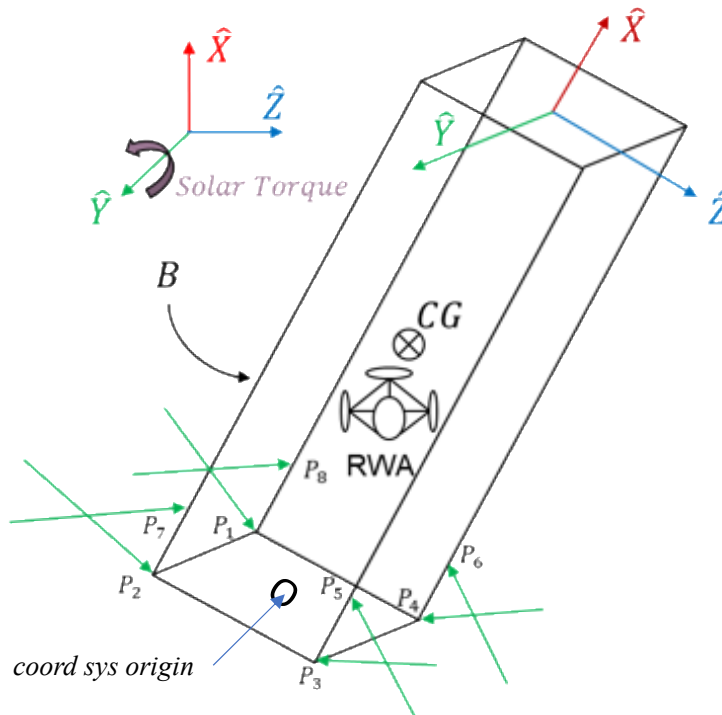
Figure 7.1-6. Example Approximate Observatory 2 Thruster Locations

Like Observatory 1, Observatory 2 is assumed to be in a Sun-Earth L$_2$ orbit, so the only environmental disturbance is the torque due to solar pressure. For simplicity, the solar radiation torque disturbance for Observatory 2 was set to:

$$T_s = [0, 1 \times 10^{-3}, 0] \ N \cdot m$$

The Observatory 2 FEM provided for this simulation was a 342-state flexible state-space model that included 171 modes. In this delivered model, the frequency response had unusual behavior at low frequencies. The plot of the singular value of the frequency response of the original FEM from the three-axis torque inputs to the output rates is shown in Figure 7.1-7.
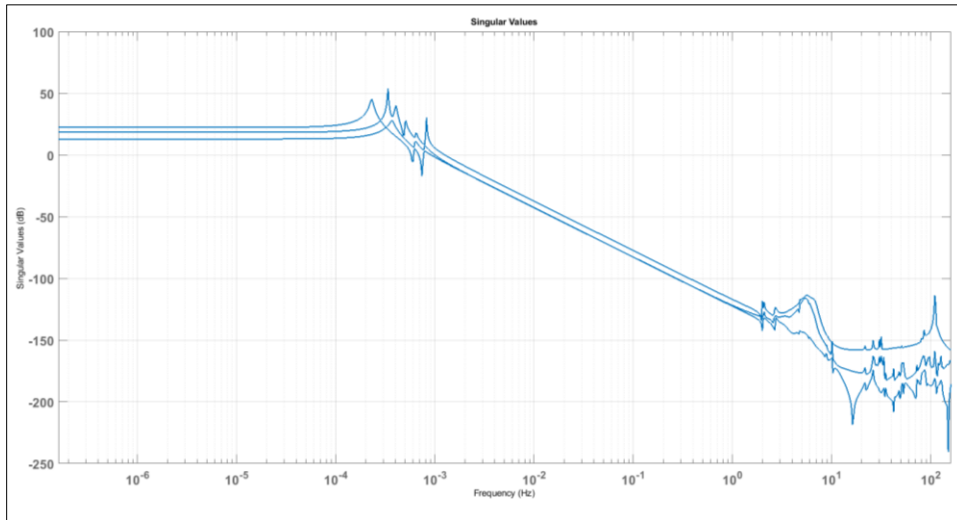
Figure 7.1-7. Singular Values of Frequency Response of Original Observatory 2 Model

Due to the low frequency of the unusual dynamics, the assessment team suspected the error was due to numerical issues in the generation of the state-space model. The Roman project (from which the team received the Observatory 2 model) was unable to generate a revised model on the timescale needed for this assessment. However, in consultation with the project, the assessment team implemented an ad-hoc method in which a singular value decomposition was applied to the state space "A" matrix, the 12 smallest singular values (i.e., magnitudes smaller than 1e-4) were set to zero, and the "A" matrix was reconstructed. The frequency response of the resulting system is shown in Figure 7.1-8.
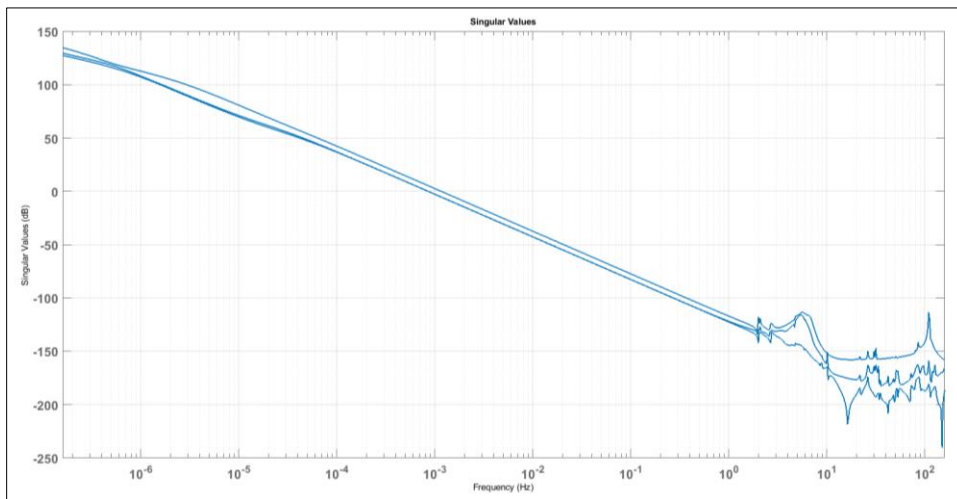
Figure 7.1-8. Singular Values of Frequency Response of Modified Observatory 2 Model

Although the method did not result in a pure double integrator response at low frequencies, it removed the unusual dynamics. The assessment team judged it suitable and used the model for simulations.

7.1.2 Reaction Wheel Modeling

Figure 7.1-9 shows the reaction wheel model used in the simulation.
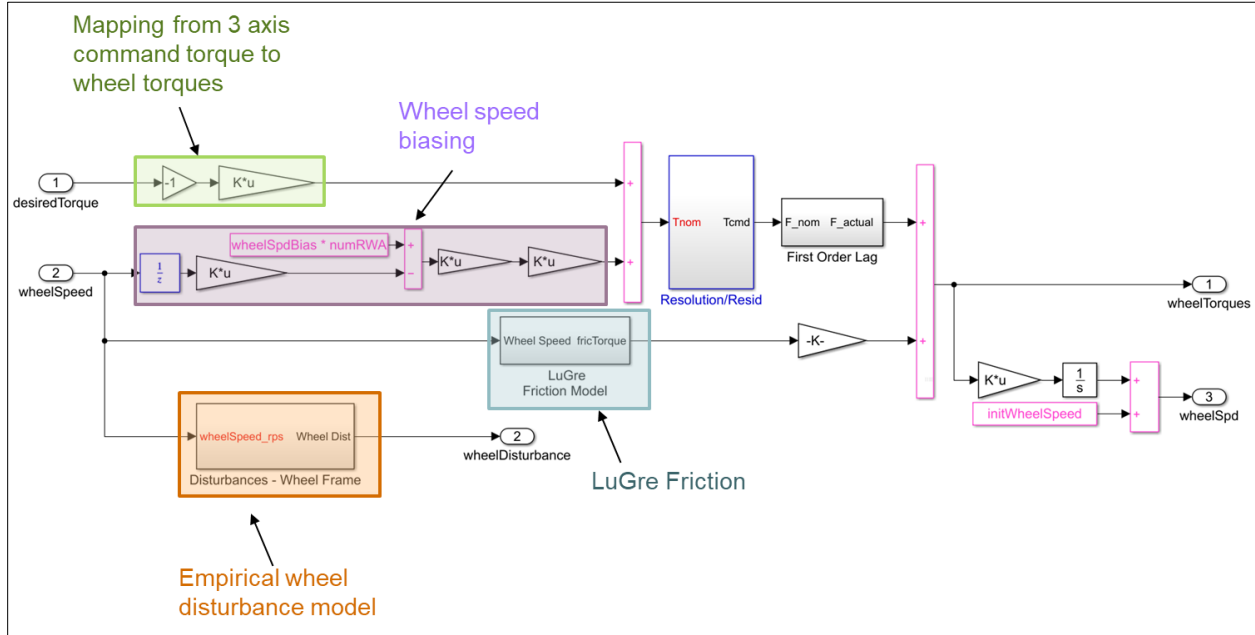
Figure 7.1-9. Reaction Wheel Model

For Observatory 2, the wheels have inertia $0.4\ kg \cdot m^2$ while the wheels for Observatory 1 are $20\ kg \cdot m^2$. Such large inertia was assumed for the Observatory 1 wheels because of the vehicle's high mass properties. The assessment team acknowledges that the Observatory 1 wheels are unrealistically large, and a spacecraft this large would likely use control moment gyros in a final design.

7.1.2.1. Wheel Control Design

In our simulations, both Observatory 1 and Observatory 2 use a simple proportional-integral-derivative (PID) reaction wheel controller cascaded with filters to notch out specific resonant modes or roll off the response at higher frequencies (Figure 7.1-10).
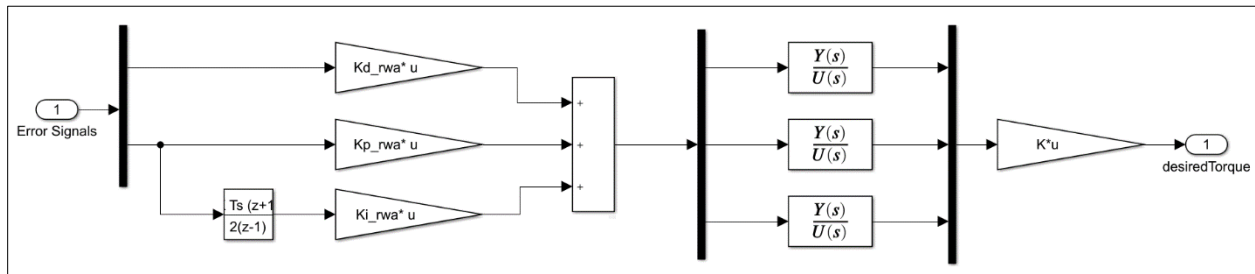
Figure 7.1-10. Reaction Wheel Controller

For Observatory 1, the reaction wheel PID gains were chosen to achieve a controller bandwidth of 0.01 Hz, resulting in the following values:

$$Kp_{rwa} = [0.0013, 0.0013, 0.0013]$$
$$Ki_{rwa} = [0.1300, 0.1300, 0.1300] \times 10^{-4}$$

$Kd_{rwa} = [\,0.0500, 0.0500, 0.0500]$The Observatory 2 reaction wheel gains were chosen to achieve the same 0.01-Hz controller bandwidth as Observatory 1, resulting in the following values:

$$Kp_{rwa} = [0.6317, 0.6317, 0.6317] \times 10^{-3}$$
$$Ki_{rwa} = [0.3158, 0.3158, 0.3158] \times 10^{-5}$$
$$Kd_{rwa} = [0.0422, 0.0422, 0.0422]$$

7.1.2.2. Wheel Disturbance Model

The wheel disturbance model is an empirical disturbance model [ref. 6]. The governing equation for the disturbance inputs is given in Figure 7.1-11.

$$m(t) = \sum_{i=1}^{n} C_i \Omega^2 \sin(2\pi h_i \Omega t + \alpha_i)$$

- $m(t)$ -- the disturbance force & torque in N, or Nm
- n -- the number of harmonics included in the model
- C_i -- the amplitude of the ith harmonic in N2/Hz, or Nm2/Hz
- Ω -- the wheel speed in Hz
- h_i -- the harmonic number
- α_i -- a random phase (uniform distributed between [0, 2pi].

Figure 7.1-11. Governing Equation for Wheel Disturbance Model

Empirically derived coefficients for the Ithaco B and Ithaco E wheels were identified as model inputs in Reference 6. These are given in Figures 7.1-12 and 7.1-13.

Table 3.3: Empirical Model Parameters for Ithaco B Wheel

Radial Force, $n_{rad} = 13$		Radial Torque, $n_{tor} = 11$		Axial Force, $n_{axi} = 4$	
Harmonic Number, h_i	Amplitude Coefficient, C_i N/rpm^2 x10e^{-7}	Harmonic Number, h_i	Amplitude Coefficient, C_i N/rpm^2 x10e^{-7}	Harmonic Number, h_i	Amplitude Coefficient, C_i N/rpm^2 x10e^{-7}
0.99	0.2134	0.99	0.0630	0.99	0.0727
1.99	0.0510	1.99	0.0314	1.41	0.0497
2.46	0.0609	3.16	0.0089	2.82	0.0975
3.16	0.0783	4.56	0.0119	5.95	0.1989
3.87	0.0528	5.28	0.0261		
4.56	0.0905	5.97	0.0372		
5.28	0.1752	6.23	0.0237		
5.98	0.3040	6.68	0.0276		
6.71	0.2053	7.38	0.0335		
8.09	0.3246	8.09	0.0477		
8.83	0.3517	8.80	0.0400		
9.54	0.2991				
10.25	0.3183				

Figure 7.1-12. Ithaco B Wheel Disturbance Coefficients

Table 3.4: Empirical Model Parameters for Ithaco E Wheel					
Radial Force, $n_{rad} = 7$		Radial Torque, $n_{tor} = 6$		Axial Force, $n_{axi} = 5$	
Harmonic Number, h_i	Amplitude Coefficient, C_i N/rpm^2 x10e^{-7}	Harmonic Number, h_i	Amplitude Coefficient, C_i N/rpm^2 x10e^{-7}	Harmonic Number, h_i	Amplitude Coefficient, C_i N/rpm^2 x10e^{-7}
1.00	0.4155	1.00	0.2205	1.00	0.3038
2.00	0.0832	2.00	0.0609	1.98	0.2818
3.00	0.0543	3.00	0.0242	2.96	0.0719
4.00	0.0621	4.00	0.0243	4.00	0.0685
4.42	0.1097	4.42	0.0485	4.33	0.1011
5.37	0.0542	5.58	0.0498		
5.57	0.0690				

Figure 7.1-13. Ithaco E Wheel Disturbance Coefficients

Since deriving coefficients for new wheel models would require extensive wheel data and additional post-processing, the simulations in the following sections will use the existing Ithaco B wheel disturbance model. Note that the disturbance model was kept the same for Observatory 1 and Observatory 2, and was not scaled for the size of the Observatory 1 wheels. Because the wheel disturbance is the same, it is expected that the wheels impart more disturbance to Observatory 2 due to its smaller mass properties.

7.1.2.3   Wheel Speed Bias Loop

The primary function of the wheel speed bias loop is to drive the wheels from zero shaft speed. To accomplish this, the wheel speed bias loop commands a zero net torque increase in the wheel speeds until the average speed is equal to the bias speed. Specifically, the equation used is:

$$T_{bias} = K_{bias} \cdot (n_{rwa} \cdot \omega_{bias} - \omega \cdot sign(V_{null}))V_{null}$$

where K_{bias} is the gain (1×10^{-3} for Observatory 2, 1×10^{-1} for Observatory 1), n_{rwa} is the number of reaction wheels (i.e., six for Observatory 2, and four for Observatory 1), ω_{bias} is the desired bias speed, ω is the current wheel speeds, and V_{null} is a vector in the null space of the wheel configuration matrix. For every simulation with a nonzero bias, the desired wheel bias speed was set to be 100 RPM. This speed was chosen as a speed that was sufficiently far from zero RPM, but not large enough to impart consequential disturbance on the vehicle. The magnitude of the wheel disturbance in the model used increases proportionally to the square of the wheel speed.

7.1.2.4   LuGre Friction Model

To model all the friction effects that may exist in reaction wheels, the assessment team included a LuGre friction model in the simulation [ref. 7]. This dynamic friction model can be described by:

$$F = \sigma_0 z + \sigma_1 \frac{dz}{dt} + \sigma_2 v$$

where F is the friction force, v is the rate, σ_0, σ_1, and σ_2 are constant coefficients, and z can be obtained from the differential equation:

$$\frac{dz}{dt} = v - \frac{|v|}{g(v)}z, \quad \sigma_0 g(v) = F_C + (F_S - F_C)e^{-\left(\frac{v}{v_s}\right)^2}$$

Here, F_C is the Coulomb friction level, F_s is the stiction force, and v_s is the Stribeck velocity. For Observatory 2 and Observatory 1: $\sigma_0 = 2.0\ Nm/rad$, $\sigma_1 = 3.0e^{-3}Nms/rad$, $v_s = 0.4\ rad/s$, $F_s = 0.66 \times 10^{-3}\ N$, and $F_c = 5.0 \times 10^{-3}\ N$ [ref. 8]. The viscous friction coefficient (σ_2) was set to $6.4 \times 10^{-5}\ Nms/rad$ for Observatory 2 [ref. 8], and $5.12 \times 10^{-3}\ Nms/rad$ for Observatory 1. The viscous friction coefficient for Observatory 1 was increased to allow the disproportionately large wheels to decrease in speed in a reasonable amount of time.

7.1.2.5. Wheel Isolator Model

A wheel isolator model was included in the simulation to compare the effectiveness of current passive disturbance rejection methods against micro-thrusters. The design of the isolator takes the form of a filter between the wheel disturbance model and the flexible spacecraft model. The original isolator filter design was intended to have 0 dB DC gain with a -20 dB/decade decrease starting at 4 Hz and remaining -20 dB gain at frequencies $\geq$ 40 Hz. However, due to the relatively low sample time of the simulation, the assessment team shifted the filter to avoid aliasing effects in the transfer function. The applied filter has 0 dB DC gain with a -20 dB/decade decrease starting at 1 Hz and has a -20 dB gain at frequencies $\geq$ 10 Hz. The bode plot for this filter is shown in Figure 7.1-14.
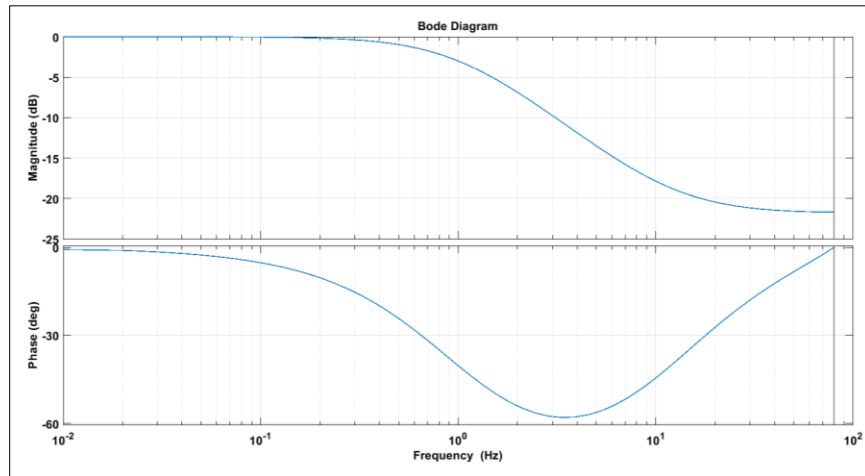
Figure 7.1-14. Isolator Filter

Note that this isolator filter is applied only in a subset of Observatory 2 cases.

7.1.3 Thruster Modeling

A visual representation of the thruster model is shown in Figure 7.1-15.
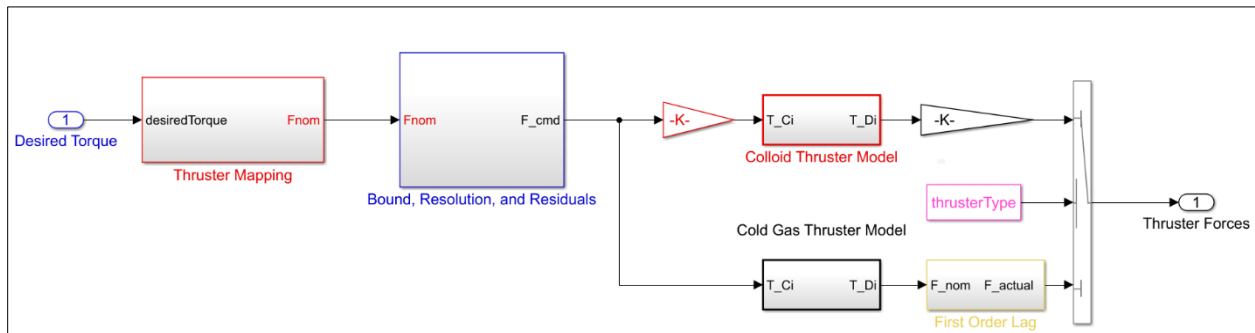
Figure 7.1-15. Thruster Model

Due to the control authority needed to reject transient disturbances and the small thrust force from a single ST7 colloid thruster head (35 µN), the assessment team increased maximum force by including a multiplier (i.e., 4 for Observatory 1 and 30 for Observatory 2, since the disturbances on the smaller Observatory 2 were expected to be larger than on the more massive Observatory 1) for the colloid thrusters. This could be interpreted as collocating multiple ST7-style colloid thruster heads in a single location or assuming a single larger thruster head (configured differently than ST7) in that location. For simplicity, this was implemented in the simulation as an increase in the maximum force.

In the simulation, the minimum deliverable force and thrust resolution remained as specified above. If multiple thruster heads using the existing ST7 design are collocated in a group, the minimum thrust would increase. However, other micro-thruster architectures are available that allow a wider dynamic range. For example, each ST7 thruster head has 9 emitters, producing a total of 35 μN maximum thrust. A grouping of four ST7 heads has a total of 36 emitters—the maximum and minimum thrust would increase by a factor of 4. However, a thruster head with 1, 3, 12, and 36 emitters allows spanning the full dynamic range from 1 to 170 μN (1 μN from running only one emitter, 170 μN from running all in parallel).

7.1.3.1 Thruster Mapping

Mapping for the thrusters was determined using a non-negative least squares method. In this method, the component torques provided by each thruster are placed into a matrix and then a thruster mapping that can provide a unit torque in a given direction is determined by solving a set of linear equations.

7.1.3.1.1 *Non-negative Least Squares*

Given the normalized thruster (force) vector, $\vec{F}_i$, and the position of the thruster relative to the center of mass $\vec{r}_i$, the unit torque provided by a unit force can be given by:

$$\vec{\tau}_i = \vec{r}_i \times \vec{F}_i$$

Stacking the torques from each thruster into a matrix results in:

$$T_{config} = [\vec{\tau}_1, \ ... , \vec{\tau}_{n_{thr}}]$$

The necessary force from each thruster, F_{thrust}, to obtain a desired torque, $T_{desired}$, is given as the solution to the following linear equation:

$$T_{config} \, F_{thrust} = T_{desired}, \ \ F_{thrust} \geq 0$$

With n_{thr} thrusters and three rotational axes, a solution is guaranteed if T_{config} is full row rank. This problem can be restated as:

$$AX = B, \ \ X \geq 0,$$

If A has full row rank, then there is guaranteed to be a solution to $AX = B$. Otherwise, the optimization problem can be converted into

$$\min_{X}|AX - B| \, s.t. X \geq 0,$$

which would find the X that minimizes $AX - B$. Efficient algorithms exist for solving these problems. Note that this approach can be applied to the translational motion, but translation was not considered in this assessment.

7.1.3.1.2 Solving for Forces from Thrusters

In this simulation, the assessment team took a non-negative least squares approach to obtain thruster mapping, or solving for the F_{thrust} that satisfies the equations.

$$T_{config}\ F_{thrust} = T_{desired}, \quad T_{desired} = \{\begin{bmatrix} \pm 1 \\ 0 \\ 0 \end{bmatrix}, \begin{bmatrix} 0 \\ \pm 1 \\ 0 \end{bmatrix}, \begin{bmatrix} 0 \\ 0 \\ \pm 1 \end{bmatrix}\}$$

The full thruster mapping is shown in Figure 7.1-16.
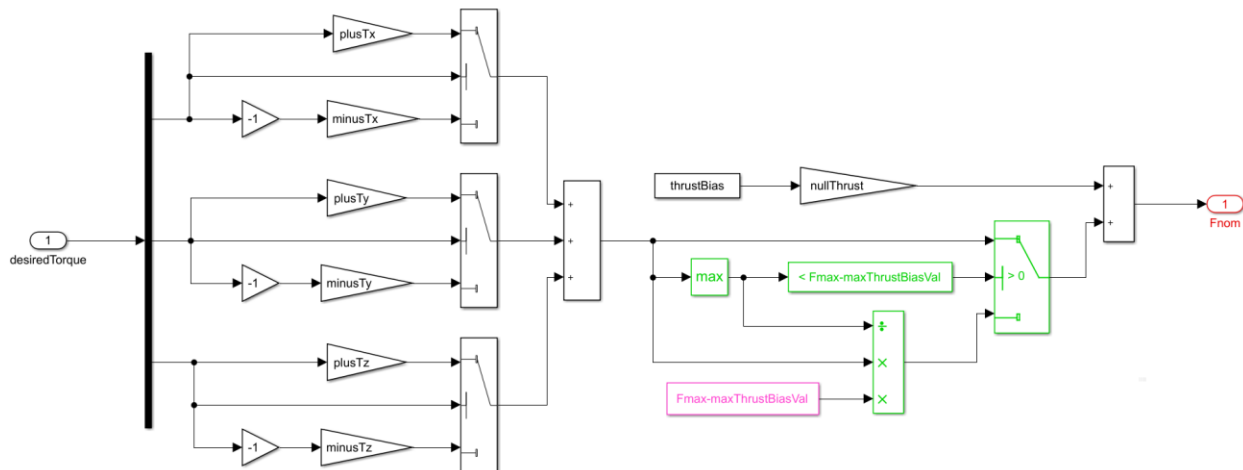
Figure 7.1-16. Thruster Mapping

In Figure 7.1-16 the left half of the model multiplies the commanded torque by the unit torque thruster mapping. The contributions from each axis are summed to obtain the necessary total force from each thruster. The right half includes the addition of a thrust bias, which is applied in the null space of the thruster configuration matrix (T_{config}) (i.e., thrusters are fired to achieve zero torque) with the minimum force being greater than the bias. The remaining section scales the commanded thrusts to prevent saturation of the thrusters.

The thrust bias for both vehicles and micro-thruster types was set to 5 μN.

7.1.3.2 Thruster Control Design

The control design for the thrusters used PID control in the same manner as the reaction wheel controller. The block diagram for the thruster PID control is shown in Figure 7.1-17.
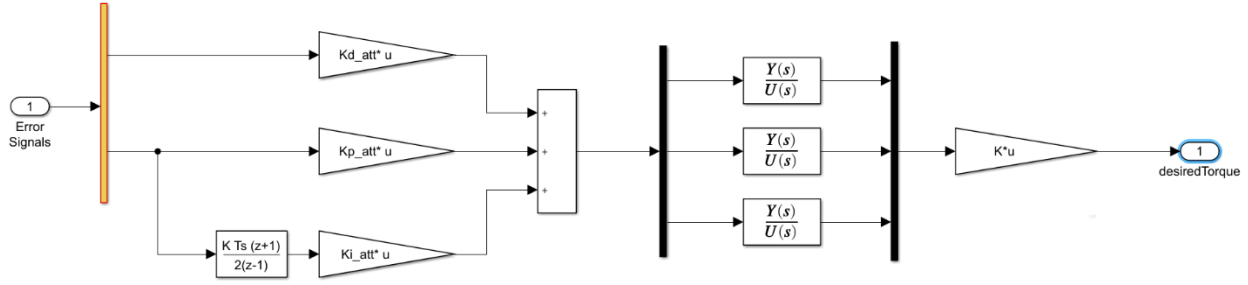
Figure 7.1-17. Thruster Control

For Observatory 1, the thruster PID gains were chosen to achieve a controller bandwidth of 0.05 Hz, resulting in the following values:

$$Kp_{att} = [0.0065, 0.00325, 0.0065]$$
$$Ki_{att} = [0.3250, 0.3250, 0.3250] \times 10^{-4}$$
$$Kd_{att} = [0.3500, 0.1750, 0.3500]$$

For Observatory 2, the thruster PID gains were chosen to achieve a controller bandwidth of 0.1 Hz, resulting in the following values:

$$Kp_{att} = [0.062, 0.0632, 0.0632]$$
$$Ki_{att} = [0.9475, 0.9475, 0.9475] \times 10^{-3}$$
$$Kd_{att} = [0.4398, 0.4398, 0.4398]$$

7.1.3.3   Thrust Bound, Resolution, and Residual Feedback

Along with the thruster control, mapping, and transient, bounds were added on the commanded thruster force, command resolution, and residual feedback (Figure 7.1-18).
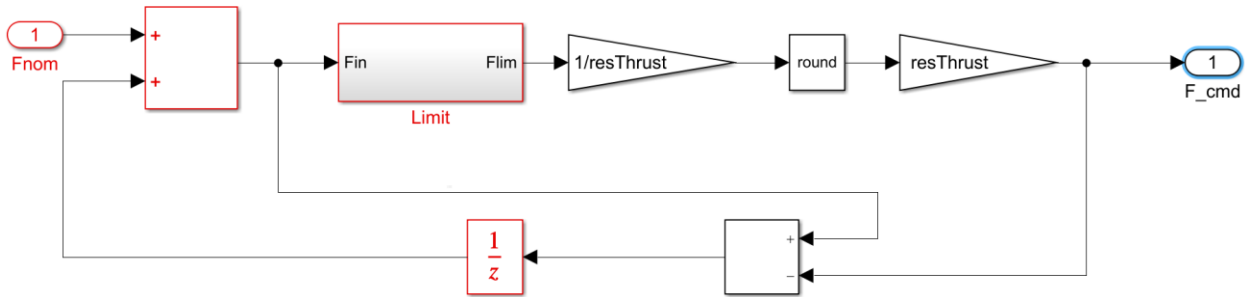
Figure 7.1-18. Residual Feedback, Bound, and Resolution

First the command was bound to a given thruster by the minimum and maximum forces, then the resolution of output was limited by multiplying against the inverse of the desired max resolution, rounded, and multiplied by the desired resolution. For example, a command force of $0.25\ mN$ with a resolution of $0.1\ mN$ would be rounded to a commanded force of $0.3\ mN$; $round(0.25 \times 10) \times 0.1 = 0.3\ mN$.

Finally, the assessment team implemented a pulse accumulated residual feedback, which fed back the difference between the desired value from the controller and the final commanded value after bounding and resolution.

7.1.3.4 Colloid Thruster Model

Outside the general thruster mapping and controller, each thruster had its own micro-thruster-specific model. In the case of the Busek CMNT, the inner loop controller implemented to control the desired thrust to true commanded thrust was the same controller used on-orbit for ST7-DRS. The primary elements of the controller are shown in Figure 7.1-19 [ref. 9].

Read back delivered (measured) values of I_{BD}, V_{BD} from the PPU

$$T_{Di} = C_1 I_{BDi}^{3/2} V_{BDi}^{1/2}$$

Calculate delivered thrust (with limited I_B).
Receive thrust command from IAU.
Calculate thrust change between commanded and delivered thrust.

$$\left(\frac{dT}{dt}\right)_a = \frac{T_{ci} - T_{D(i-1)}}{\Delta t}$$

Calculate the beam current, I_B, then limit it and the change in it in 1 cycle.

$$I_{Bi} = \left[\frac{\langle T_{ci}\rangle}{C_1\sqrt{V_{BNOM}}}\right]^{\frac{2}{3}}$$

$$\frac{dV_{Bi}}{dt} = V_{B(i-1)}\left[\frac{2}{T_{ci}}\left(\frac{dT}{dt}\right)_a - \frac{3}{I_{Bi}}\left\langle\frac{dI_B}{dt}\right\rangle_i\right]$$

Calculate the beam voltage, V_B, then limit it and the change in it in 1 cycle.

$$V_{Bi} = V_{B(i-1)} + \frac{dV_{Bi}}{dt}dt$$

$$I_{Berri} = I_{Bi} - I_{BDi}$$
$$V_{pi} = \left[K_p I_{Berri}\right] + \left[K_i \sum_i I_{Berri}\right]$$

Calculate the valve voltage, V_v, then limit it.

$$V_{Ei} = K_{Gain} I_{BDi} + K_{offset}$$

Send set points V_{pi}, V_B, V_{Ei} to PPU

Wait for next thrust command

T = thrust
I_B = beam current
V_B = beam voltage
$\langle T_{ci}\rangle$ = Thrust running average

Δt = 0.1 s
i-1 = previous time step
V_{BNOM} = nominal beam voltage
Subscript C = commanded
Subscript D = delivered
Subscript a = actual

Figure 7.1-19. Primary Elements of the CMNT Thrust Control Algorithm

The controller converted the commanded thrust to desired voltages and currents. Noise was added to these voltages and currents, and the resulting value was converted to the force applied to the vehicle. The characteristics of the noise and the thruster performance model were validated on-orbit during ST7 [ref. 9]. Figure 7.1-20 shows a typical time series during ST7 in science mode, with a minor micrometeorite impact, showing the typical colloid micro-thruster response and the difference between commanded and achieved thrust [ref. 9]. The figure shows a comparison of commanded and direct thrust measurements based on applied electrostatic forces and test mass displacements during an intentional excursion in thrust commands during "attitude only" mode on ST7. In this mode, the capacitive sensing and forcing signals were in a low-resolution, high-force mode with a higher level of noise than in science mode. The measured thrust noise in science mode was shown to be lower than 0.1 μN/rtHz, meeting requirements over the measurement bandwidth.
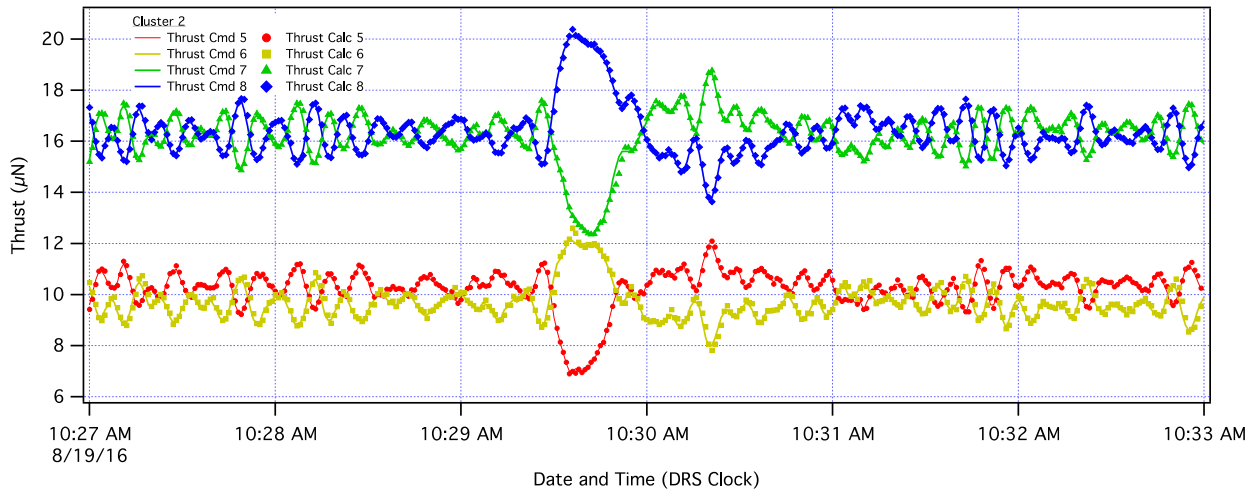
Figure 7.1-20. Colloid Thruster Commands (solid lines) and Response (dots), Based on Current and Voltage Measurements from all Four Thrusters on Cluster 4 During Science Mode on ST7
Note: Around 10:29 am, a micrometeorite impact caused a deviation in thruster commands where the thruster response was accurate enough to maintain spacecraft and test mass stability.

7.1.3.5   Cold Gas Thruster Model

By comparison, the model for the cold gas micro-thruster is simpler than the colloid thruster. It is described by additive white noise and a time lag for the transient response.

7.1.3.5.1   Additive Noise Model

The thruster noise was implemented as simple additive white noise, as shown in Figure 7.1-21, with T_Ci being the commanded thrust and T_Di being the delivered thrust.
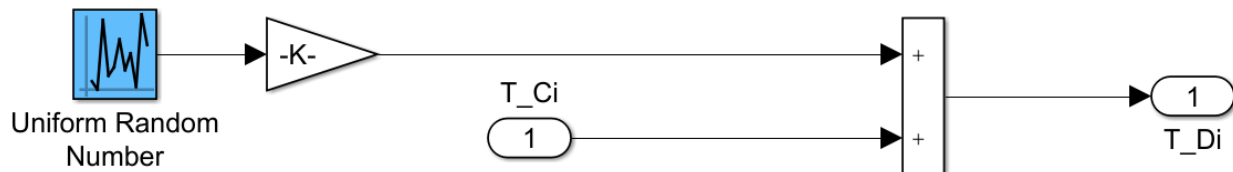
Figure 7.1-21. Additive Noise to Cold Gas Thrusters

Specifically, the input noise was designed such that the PSD would match the specified maximum RMS value for the thruster noise 3.22 *µN* that was specified as a requirement in Microscope's design [ref. 10]. The PSD for the additive white noise is shown in Figure 7.1-22.
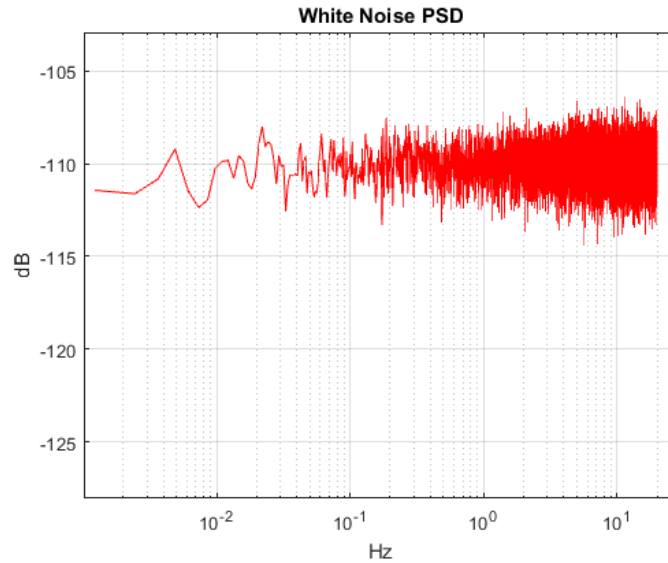
Figure 7.1-22. PSD for Cold Gas Thruster Additive White Noise

In the Figure 7.1-22 PSD, the noise level is calculated to be $\sqrt{10^{-\frac{110}{10}}} = 3.16 \times 10^{-6}$. In comparison, the measured axial thruster noise of the Microscope thrusters during satellite thermal vacuum is given in Figure 7.1-23 [ref. 3].
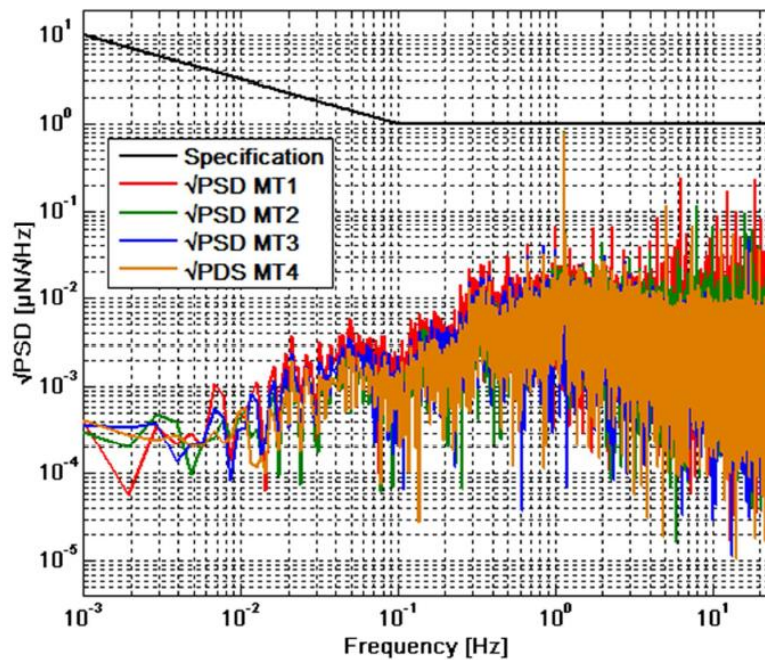
Figure 7.1-23. Axial Thrust Noise During Satellite Thermal Vacuum

To further compare the additive noise to the commanded thrust, Figure 7.1-24 shows the thrust resolution of a Leonardo cold gas thruster inside a thermal vacuum [ref. 3] while Figure 7.1-25 displays the thruster command after the PID controller, mapping, and transient, and the realized thrust after applying the additive noise.
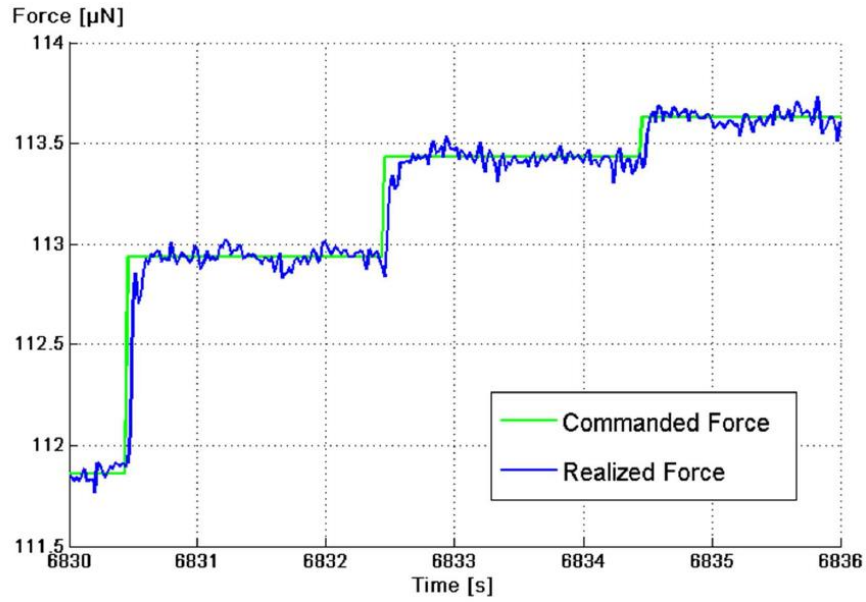
Figure 7.1-24. Cold Gas Thrust Resolution Inside Thermal Vacuum
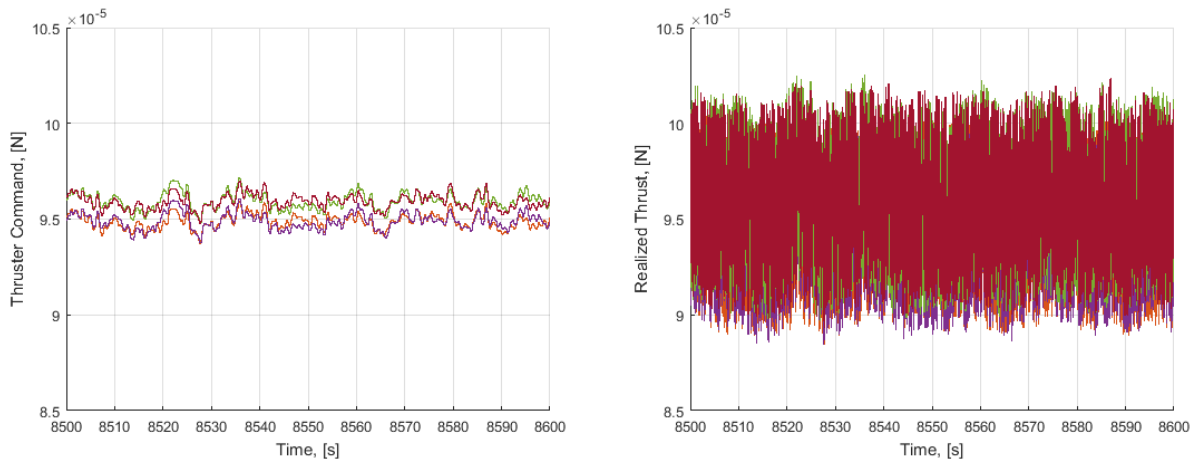
Figure 7.1-25. Cold Gas Thruster Command After PID and Mapping (L), Realized Thrust Command from Thrusters (R)

The magnitude of noise added is significantly higher than observed for the Leonardo cold gas thrusters. This was intentional, to compensate for potentially unmodeled effects.

7.1.3.5.2   Transient Response

The implementation of this first-order filter is given in Figure 7.1-26.
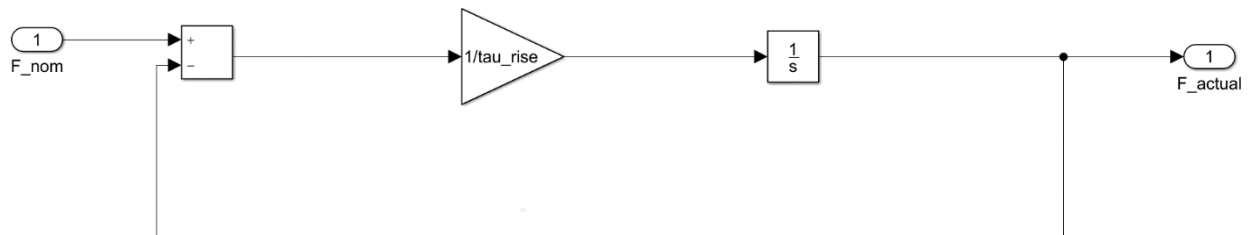
Figure 7.1-26. Implementation of Thruster Transient

In the Figure 7.1-26 block diagram, a nominal desired force is sent from the controller and passed through a continuous time representation of a low pass filter. Based on the data provided by Leonardo, the time constant for the low pass filter was determined to be $\tau = 0.08\ sec$.

7.2 Evaluation and Analysis

7.2.1 Stability Analysis

The linear stability analysis for the control design for each of the actuators was performed by breaking each loop individually, linearizing the resulting system, and generating the Bode and Nichols plots.

For example, evaluating the open-loop transfer function and corresponding gain and phase margins for the thruster X-axis torque loop would involve breaking the closed-loop system between the thruster PID and mapping for the X-axis torque, as shown in Figure 7.2-1.
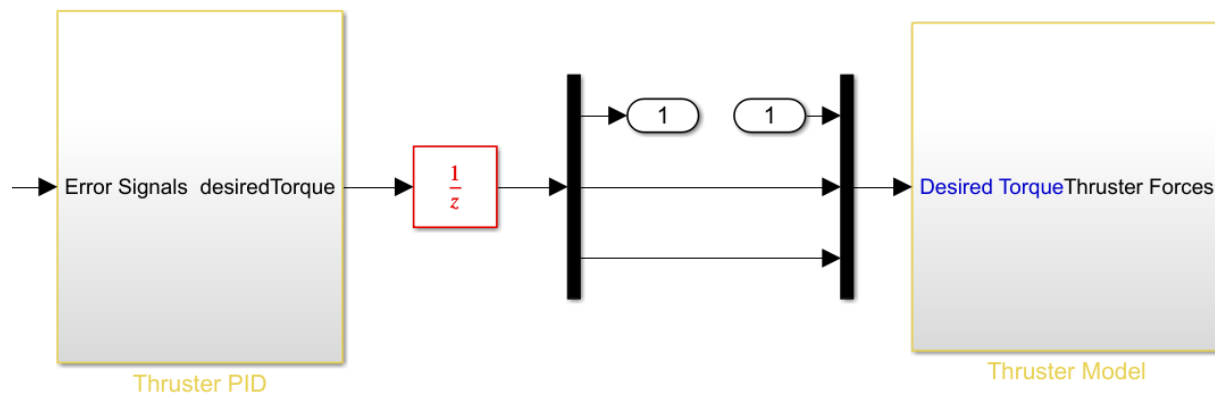
Figure 7.2-1. Example of Evaluating Thruster X-axis Torque Loop

The linearization of the Simulink model was performed by using the built-in MATLAB function *dlinmod* to obtain a discrete-time linear state-space model of the system. Finally, the analysis was done using the built-in MATLAB functions *Nichols* and *margin,* which provide the Nichols plots and bode plots, respectively. The evaluation for all the control loops can be found in Appendix B.

7.2.2 Time-domain Simulations

The following time-domain simulations cover a wide range of possible scenarios to evaluate the effectiveness of various attitude control actuators. Specifically, the simulations include:
- Fine pointing controlled by a single actuator (i.e., reaction wheels or micro-thrusters).
- Fine pointing controlled solely by micro-thrusters, with wheels spinning at 100 RPM as discussed in Section 7.1.2.3. It is assumed that some operational restriction prevents shutting off the wheels.
- Fine pointing controlled by micro-thrusters and reaction wheels simultaneously. (As in the previous scenario, it is assumed that some operational restriction prevents shutting off the wheels; however, here both wheels and micro-thrusters are used for fine pointing control, with each actuator using the same attitude knowledge information but operating at different control bandwidths, nominally 0.01 Hz for wheels and 0.1 Hz for micro-thrusters). Wheel speed bias was set to 100 RPM; the wheel controller typically varies speed slightly for fine pointing.

- Slewing with reaction wheels, then transitioning to fine pointing controlled by micro-thrusters only with wheels shut down.
- Slewing with RCS thrusters, then transitioning to fine pointing controlled solely by micro-thrusters.
- Slewing with reaction wheels, then transitioning to fine pointing controlled by micro-thrusters and reaction wheels at 100 RPM simultaneously.
- Slewing with reaction wheels, then transitioning to fine pointing controlled solely by micro-thrusters, with wheels spinning at 100 RPM.

All the slew cases follow the same ramp-up/ramp-down profile of [-5, 10, 15] degrees (i.e., no coasting) before transitioning to the specified actuators for fine pointing.

Each simulation lasts for 5,000 seconds, except cases 17 and 25. For those cases, the simulation was run for 7,500 seconds to allow some operating time after reaching wheel speed of 0 RPM. Any actuator changes included in the scenario (e.g., transition from wheels to micro-thrusters) occurred at 2,500 seconds.

7.2.3   Pointing Analysis

To evaluate the pointing performance of the different test cases, the assessment team took the pointing error of the last 1,000 seconds of the simulation and performed a 10-second root-mean-square (RMS) sliding window analysis of the error. The assessment team calculated the RMS angle error over a given 10-second window, shifted the window by one sample point, and repeated the process. For brevity, only the 95th percentile RMS values were included for each of the axes. The pointing performance for every tested scenario is shown in Tables 7.2-1, 7.2-2, and 7.2-3, and illustrated in Figure 7.2-2. Detailed results plotted for each case can be found in Appendix A.

7.2.4   Discussion of Results of Fine-Pointing Simulations

The simulation utilized for this study was "generic" in scope. Resource limitations prohibited detailed tailoring or optimization of model parameters, controller gains, and other features individually for the two Observatories. Nevertheless, results of our simulations with micro-thrusters indicate an improvement of at least an order of magnitude compared with HST's 7 mas. Improved tailoring of controller parameters could possibly further improve performance results with micro-thrusters only.

In concert with the analysis plan, the team implemented a simulation of a "continuous" momentum management mode using the micro-thrusters to unload the wheels. This mode fired the thrusters if the wheels exceeded a threshold speed, and turned them off once it fell below another threshold speed. However initial simulations in this mode showed no improvement in pointing performance because the pointing error was dominated by the wheel disturbance. Thus, use of this mode was discontinued in favor of a simultaneous wheel/micro-thruster operating mode. Consequently, results in the continuous momentum management mode are not shown in Tables 7.2-1 through 7.2-3 and Figure 7.2-2 below.

The "wheels-only" results (842 mas for Observatory 2 without isolators, 573 mas for Observatory 2 with isolators, 37.8 mas for Observatory 1) are worse than the observed performance of HST (7 mas) and the Roman Space Telescope's requirement of 14 mas. Both HST and the Roman Space Telescope incorporate mechanical isolation, and HST's wheels were carefully balanced. The assessment team lacked access to the HST wheel disturbance model, but

it is likely that the "generic" wheel disturbance model used in the simulations is "noisier" than the model that applies to HST. Therefore, it is also likely that the simulation results in cases using both wheels and micro-thrusters could be pessimistic compared with potential real-world performance with well-balanced wheels operated at low RPM.

In addition, the wheel-only PID control law for Observatories 1 and 2 was chosen to have a bandwidth of 0.01 Hz. The thruster PID gains for Observatory 1 had a bandwidth of 0.05 Hz, and Observatory 2 had a bandwidth of 0.1 Hz. Comparing Figures A.1-3 and A.1-4, the difference in frequency content is apparent. The 5x to 10x difference in controller bandwidth may be a contributing factor to the large difference in pointing performance between wheels and micro-thrusters observed in the simulations.

7.2.4   Potential Requirements of Future Fine-Pointing Missions on Micro-Thrusters

For future observatory missions, higher maximum thrust than demonstrated on ST7/LPF may be needed with lifetimes roughly equivalent to LISA's. For example, HaBeX is working toward a maximum thrust of 350 μN on each S/C axis [ref 42]. For "DC" solar pressure torque stabilization, worst case analysis shows that one or more spacecraft axis will need >300 μN.

To reach 350 μN while allowing the lowest possible minimum thrust, it is necessary to arrange multiple thruster heads in a "thruster head assembly" or THA, with different numbers of emitters per head pointing in the same direction, as discussed in section 7.1.3. The current HaBeX configuration defines a THA consisting of a primary and redundant set of thruster heads with ~200 total emitters per THA, split between 8 thruster heads (4 primary, 4 redundant). One primary and one redundant thruster head in each THA has 90 emitters (10 times as many as ST7). The current HaBeX configuration has 12 thrust directions. With 200 emitters pointing in each direction, this adds up to 2,400 total emitters on the S/C [ref 43].

Micro-thruster technology development work may be needed in a few areas to meet the needs of HaBeX. Scaling the number of emitters per thruster head by a factor of 10 could lower the TRL of the thruster head, requiring technology development preparatory to flight. Building emitters is a time-consuming process done largely by hand. Currently it takes ~ 6 months to build 100 emitters, so building the 2,400 emitters required for HaBeX would be prohibitive, This provides motivation for investigating alternatives to the emitter design (possibly with higher maximum thrust per emitter, which would reduce the total number of emitters required) or developing new manufacturing techniques for the existing ST7-style emitters.

HaBeX is also looking at other thrusters with higher maximum thrust, but those will also be lower TRL for this application as they are most commonly not designed for precision thrust, but for accomplishing delta-v on smallsats.

7.2.4   Analysis of Potential Benefits of Micro-Thrusters for Formation Flying – Starshade

Various modes of formation flying have been used or proposed for different missions. Formation flying generally requires maneuvers for small attitude and/or velocity changes to maintain a constellation of multiple spacecraft within specified position and/or attitude requirements. The requirements can vary significantly depending on the mission. The plan for this assessment included preliminary evaluation of the use of micro-thrusters for an example formation flying mission. The example chosen was a Starshade mission concept studied by GSFC [ref 40].

This mission pairs a space-based telescope observatory with a separate Starshade spacecraft for observations of planets orbiting about distant stars. The Starshade is used to occult the star,

blocking its light to enable observations of the darker planet or planets orbiting the star using the telescope observatory. The separation distance required between the telescope and Starshade is 10,000 to 50,000 km (depending on concept details).

The pointing requirement for the Starshade is ~1 deg (not stringent). However, the Starshade must observe a more stringent requirement of staying within a 1-m radius of the line of sight to the telescope observatory [ref. 41]. Thrusters must be strong enough to balance differential solar pressure accelerations and gravity gradient accelerations due to the separation between the two spacecraft (10,000 km to 50,000 km, depending on concept details). Differential gravity gradient acceleration was estimated at 1e-5 m/s^2, and acceleration due to differential solar radiation pressure was less than that.

In the GSFC Starshade mission concept, the telescope observatory is the position sensor, relaying measurements to the Starshade via inter-spacecraft radio frequency (RF) communications link. Consequently, there is no need for onboard accelerometer measurements onboard Starshade.

Mass of the Starshade is estimated to be 2500 kg. Assuming a thruster head of perhaps 50 ST7 emitters, each of which produces a maximum thrust of (30/9)=3.3 µN for a total of 166.7 µN or 1.67e-4N, the maximum acceleration produced by a single thruster head is 6.7e-8 m/s^2. This is roughly 3 orders of magnitude less than the estimated 1e-5 m/s^2 required to balance differential gravity gradient acceleration (equivalent to 7,500 emitters, or approximately 3 times the number of emitters required for HaBeX) This indicates that micro-thrusters probably are not a good fit for this Starshade formation flying concept. However, progress made in packaging large numbers of emitters for HaBeX, or in increasing the maximum thrust per emitter, could change this.

A statement that micro-thrusters are not a good fit for Starshade should not be taken as a blanket statement applying to formation flying missions in general. A wide variety of mission concepts employ different modes of formation flying, many of which could have requirements that differ considerably from those of Starshade. Formation flying missions with tight fine-pointing requirements could benefit from micro-thrusters in the same way as the two Observatory concepts examined in this assessment. Less massive spacecraft with smaller disturbance forces to overcome could also use micro-thrusters for position control. For concepts like this, micro-thrusters could require less frequent firing and reduced propellant requirements compared to larger thrusters.

Table 7.2-1. Pointing Stability Performance: Observatory 2 Cases Without Isolator

		10s Sliding Window Angle Error RMS – 95%			
Case #	Case	X-axis (mas)	Y-axis (mas)	Z-axis (mas)	RSS xyz (mas)
8	Colloid micro-thrusters only	0.016	0.06	0.016	0.064
9	Wheels only	585.758	537.408	278.483	842.302
10	Cold gas micro-thrusters only	0.095	0.224	0.097	0.262
11	Colloid micro-thruster fine pointing with constant 100 RPM wheel speed	14.079	9.702	7.723	18.761
12	Colloid micro-thruster + wheel fine pointing	16.144	9.178	9.198	20.724
13	Cold gas micro-thruster fine pointing with constant 100 RPM wheel speed	13.952	9.741	7.359	18.539
14	Cold gas micro-thruster + wheel fine pointing	12.823	8.067	6.671	16.553
16	RCS thruster slew to colloid micro-thruster fine pointing	0.123	0.756	0.055	0.768
18	Wheel slew to colloid micro-thruster fine pointing	0.011	0.069	0.005	0.070
20	Wheel slew to colloid micro-thruster + wheel fine pointing	13.77	8.547	7.023	17.663
22	Wheel slew to colloid micro-thruster fine pointing with constant 100 RPM wheel speed	13.709	9.017	7.372	17.989
24	RCS thruster slew to cold gas micro-thruster fine pointing	0.143	0.799	0.077	0.815
26	Wheel slew to cold gas micro-thruster fine pointing with 0 RPM wheel speed	0.091	0.235	0.094	0.269
28	Wheel slew to cold gas micro-thruster + wheel fine pointing	14.091	8.107	7.109	17.743
30	Wheel slew to cold gas micro-thruster fine pointing with constant 100 RPM wheel speed	13.551	8.388	7.585	17.650

Table 7.2-2. Pointing Stability Performance: Observatory 2 Cases with Isolator

		10s Sliding Window Angle Error RMS – 95%			
Case #	Case	X-axis (mas)	Y-axis (mas)	Z-axis (mas)	RSS xyz (mas)
9	Wheels only	270.19	494.175	104.92	572.905
11	Colloid micro-thruster fine pointing with 100 RPM wheel speed	8.691	5.497	4.839	11.365
12	Colloid micro-thruster + wheel fine pointing	8.087	5.201	4.212	10.497
13	Cold gas fine pointing with 100 RPM wheel speed	8.681	5.543	4.94	11.423
14	Cold gas micro-thruster + wheel fine pointing	7.988	5.289	4.57	10.614

Table 7.2-3. Pointing Stability Performance: Observatory 1 Cases

		10s Sliding Window Angle Error RMS – 95%			
Case #	Case	X-axis (mas)	Y-axis (mas)	Z-axis (mas)	RSS xyz (mas)
1	Colloid micro-thrusters only	0.249	0.023	0.028	0.252
2	Wheels only	14.054	9.585	33.802	37.841
3	Cold gas micro-thrusters only	0.296	0.167	0.088	0.351
4	Colloid micro-thruster fine pointing with constant 100 RPM wheel speed	2.574	3.11	4.613	6.130
5	Colloid micro-thruster + wheel fine pointing	2.731	2.57	4.089	5.548
6	Cold gas micro-thruster fine pointing with constant 100 RPM wheel speed	2.685	3.001	4.658	6.157
7	Cold gas micro-thruster + wheel fine pointing	2.316	1.933	3.777	4.834
15	RCS thruster slew to colloid micro-thruster fine pointing	0.426	0.042	0.13	0.447
17	Wheel slew to colloid micro-thruster fine pointing with 0 RPM wheel speed	0.252	0.026	0.031	0.255
19	Wheel slew to colloid micro-thruster + wheel fine pointing	2.32	1.453	3.163	4.183
21	Wheel Slew to colloid micro-thruster fine pointing with constant 100 RPM wheel speed	2.706	3.471	6.314	7.697

23	RCS thruster slew to cold gas micro-thruster fine pointing	0.389	0.164	0.133	0.443
25	Wheel slew to cold gas micro-thruster fine pointing with 0 RPM wheel speed	0.297	0.099	0.107	0.331
27	Wheel slew to cold gas micro-thruster + wheel fine pointing	2.957	2.09	2.983	4.692
29	Wheel Slew to cold gas micro-thruster fine pointing with constant 100 RPM wheel speed	3.719	4.211	4.379	7.123
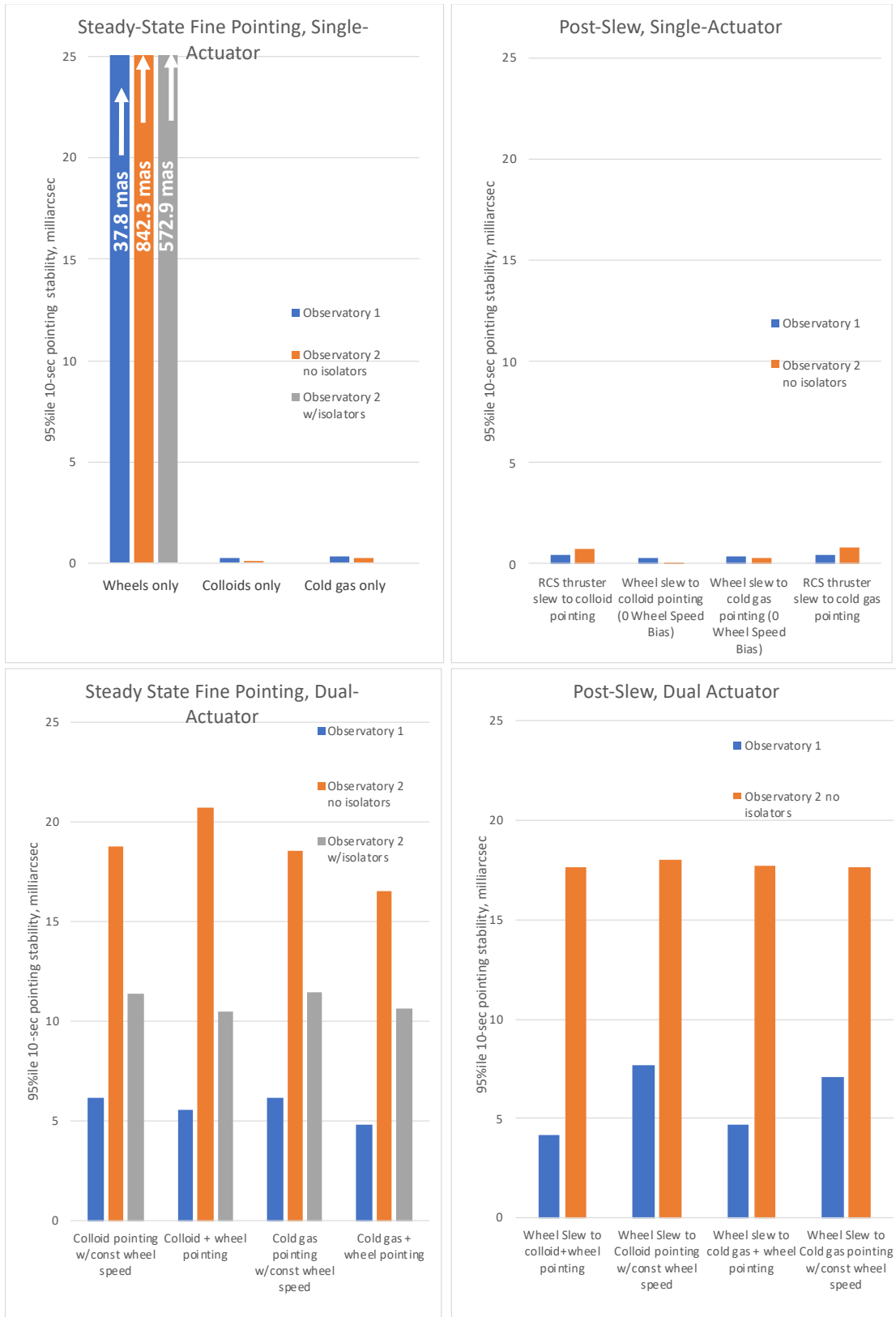
Figure 7.2-2. Graphical Representation of Results Shown in Tables 7.2-1, 7.2-2, and 7.2-3

8.0   Findings and Observations

8.1   Findings

The assessment team identified the following findings:

F-1.   Using either cold gas or colloid micro-thrusters instead of reaction wheels as the sole control method for fine pointing improves pointing stability performance by roughly an order of magnitude compared with the HST (a system with wheels-only control and tailored isolation), or almost two orders of magnitude compared with simulations of two representative wheels-only systems without isolation.

F-2.   Cold-gas and colloidal micro-thrusters produce similar pointing stability performance.

F-3.   If reaction wheels cannot be shut down due to operational constraints (e.g., for frequent slews), micro-thrusters can be used with wheels to achieve improved pointing stability performance roughly equivalent to the HST, without wheel isolation.

F-4.   Colloidal micro-thrusters have a higher specific impulse (Isp ~200 sec) and consequently a lower propellant requirement than cold-gas micro-thrusters (Isp ~60 sec), which may be a discriminating factor for some missions.

F-5.   Thrust precision and noise of current-technology cold gas and colloid micro-thrusters (~0.1 μN) are adequate for improved pointing stability of observatories in the class of those examined.

F-6.   A separate control method (e.g., wheels or RCS thrusters) is likely to be required for large attitude changes due to the limited control authority of micro-thrusters.

F-7.   It is likely that refinements to the "generic" reaction wheel disturbance model with information that is currently proprietary could improve estimates of pointing stability with reaction wheels. In addition, resource limitations prevented study of alternative architectures with large reaction wheels and smaller "vernier" wheels, mass and power trades associated with wheels vs micro-thrusters, and impact on reaction wheel lifetime due to frequent stops and starts of the large wheels. These are candidates for investigation as part of future studies of observatory attitude control systems.

F-8.   The simulation developed in this assessment is suitable for use in mission studies involving reaction wheels and micro-thrusters, and is available for use NASA-wide.

F-9.   Future multi-year astronomy and astrophysics missions requiring precision pointing stability may need microthrusters with higher maximum thrust levels, longer lifetimes, and higher bandwidth than have been demonstrated on-orbit to date. Technology development would be required to achieve these goals.

8.2   Observations

The following observations were identified:

O-1.   Micro-thrusters may impose less systemwide implementation complexity than other methods of achieving fine pointing (e.g., extensive system-level jitter testing, detailed disturbance characterization testing, or reaction wheel isolation), with the potential for improved performance.

O-2. Micro-thrusters make it easier to "test as you fly" than systems like isolators, whose behavior in flight may not be replicated in a ground-testing environment.

O-3. Micro-thrusters allow on-orbit modifications to system-level response and behavior by modifying a control algorithm, while modifications to isolators and similar systems are difficult or impossible to implement in flight.

O-4. Micro-thruster placement and number are critical to ensure adequate control torques and control saturation.

O-5. While this assessment explored one formation flying mission concept and found micro-thrusters unsuitable for that concept, it is possible that they could be a good fit for other formation flying concepts, especially with technology advancements.

9.0 Alternative Viewpoint(s)

No alternative viewpoints were identified during the course of this assessment by the NESC team or the NESC Review Board quorum.

10.0 Other Deliverables

No deliverables aside from the final report were produced during this assessment.

11.0 Lessons Learned

No lessons learned were generated during the course of this assessment.

12.0 Recommendations for NASA Standards and Specifications

No recommendations for NASA standards and specifications were identified as a result of this assessment.

13.0 Definition of Terms

Finding   A relevant factual conclusion and/or issue that is within the assessment scope and that the team has rigorously based on data from their independent analyses, tests, inspections, and/or reviews of technical documentation.

Observation   A noteworthy fact, issue, and/or risk, which may not be directly within the assessment scope, but could generate a separate issue or concern if not addressed. Alternatively, an observation can be a positive acknowledgement of a Center/Program/Project/Organization's operational structure, tools, and/or support provided.

14.0   Acronyms and Nomenclature

ACS	Attitude Control System
CMNT	Colloid Micronewton Thrusters
dB	Decibel
DC	Direct Current
DRS	Disturbance Reduction System
ESA	European Space Agency
FEM	Finite Element Model
GAIA	Global Astrometric Interferometer for Astrophysics
GN&C	Guidance, Navigation, and Control
GSFC	Goddard Space Flight Center
HabEx	Habitable Exoplanet Observatory
HST	Hubble Space Telescope
Hz	Hertz
JPL	Jet Propulsion Laboratory
LISA	Laser Interferometer Space Antenna
LPF	LISA Pathfinder
LUVOIR	Large UV/Optical/IR Surveyor
mas	Milliarcseconds
μN	Micronewtons
nN	Nanonewtons
N	Newtons
NESC	NASA Engineering and Safety Center
NGIS	Northrop Grumman Innovation Systems
OST	Origins Space Telescope
PID	Proportional-Integral-Derivative
PSD	Power Spectral Density
RCS	Reaction Control System
RMS	Root-Mean-Square
RPM	Revolutions Per Minute
SMD	Science Mission Directorate
ST7	Space Technology 7
TDT	Technical Discipline Team
TV	Thruster Valve
WFIRST	Wide Field Infrared Survey Telescope

15.0 References

1. V. Hruby, D. Spence, N. Demmons, T. Roy, E. Ehrbar, J. Zwahlen, R. Martin, J. Ziemer, W. Connolly, S. Rhodes and W. Tolman, "ST7-DRS Colloid Thruster System Development and Performance Summary," 44th AIAA/ASME/SAE/ASEE Joint Propulsion Conference & Exhibit, 2008.

2. F. Boldrini, "Ultra-Fine Controlled Cold Gas Micro Propulsion," 2016.

3. T. Liénart, G. Doulsier and V. Cipolla, "First In-flight Observations of the Cold Gas Propulsion System for CNES," in 53rd AIAA/SAE/ASEE Joint Propulsion Conference, Atlanta, GA, 2017.

4. F. Boldrini, Interviewee, Email Chain. [Interview]. 16 October 2017.

5. Wikipedia, "Wide Field Infrared Survey Telescope," Wikipedia, [Online]. Available: https://en.wikipedia.org/wiki/Wide_Field_Infrared_Survey_Telescope.

6. R. A. Masterson, "Development and Validation of Empirical and Analytical Reaction Wheel Disturbance Models," 1997.

7. C. Canudas de Wit, H. Olsson, K. J. Astrom and P. Lischinsky, "A New Model for Control of Systems with Friction," IEEE Transactions on Automatic Control, vol. 40, pp. 419-425, 1995.

8. V. Carrara, A. Graciano da Silva and H. K. Kuga, "A Dynamic Friction Model for Reaction Wheels," in IAA-AAS Conference of Dynamics and Control of Space Systems, 2012.

9. J. Ziemer, C. Marrese-Reading, C. Cutler, C. Dunn, A. Romero-Wolf, S. Javidnia, T. Le, I. Li, P. Barela, N. Demmons, V. Hruby, J. Slutsky, J. I. Thorpe, P. Maghami, O. Hsu and J. O'Donnell, "In-Flight Verification and Validation of Colloid Micro-thruster Performance," *2018 AIAA Joint Propulsion Conference,* Cincinnati, OH, July 2018. AIAA-2018-4643.

10. V. Cipolla, Y. Andre, P.-Y. Guidotti, A. Robert, P. Prieur, B. Pouilloux and L. Perraud, "Microscope: A Scientific Microsatellite Development," 2016.

11. C. Dennehy and O. Alvarez-Salazar, "Spacecraft Micro-Vibration: A Survey of the Problems, Experiences, Potential Solutions, and Some Lessons Learned," NASA TM-2018-220075.

12. [Online]. Available: https://www.nasa.gov/image-feature/jpl/lisa-pathfinder-carries-advanced-nasa-thruster-tech

13. D.G. Courtney, P. Wright, D. Lafko, E. Metivier, and N. Demmons, "Electrospray Propulsion for Precise Attitude and Position Control," paper AAS 17-088 in 40th Annual AAS Guidance and Control Conference, Breckenridge, CO, 2017.

14. B. Bialke, "High-Fidelity Mathematical Modeling of Reaction Wheel Performance," Advances in Astronautical Sciences, 1998.

15. [Online]. Available: https://directory.eoportal.org/web/eoportal/satellite-missions/m/microscope.

16. S. R. Starin and J. Eterno, "Attitude Determination and Control Systems," in Space Mission Engineering: The New SMAD, Microcosm Press, 2013, pp. 565-591.

17. S. E. Hall, M. J. Lewis and D. L. Akin, "Design of a High-Density Cold-Gas Attitude Control System," in AIAA, SAE, ASME, and ASEE, Joint Propulsion Conference and Exhibit, Monterey, CA, 1993.

18. [Online]. Available: http://www.esa.int/Our_Activities/Space_Science/Gaia/ Frequently Asked Questions About Gaia.

19. [Online]. Available: https://directory.eoportal.org/web/eoportal/satellite-missions/l/lisa-pathfinder.

20. S. Delavault, P. Prieur, T. Liénart, A. Robert and P.-Y. Guidotti, "Microscope Mission: Drag-free and attitude control system expertise activities toward the scientific team," in 10th International ESA Conference on Guidance, Navigation & Control Systems, Salzburg, Austria, 2017.

21. F. Boldrini, L. Ceruti, L. Fallerini, G. Matticari, M. Molina, G. Noci and C. E. Atzei, "A Cold-Gas Micropropulsion System as Actuator of Fine Pointing and Attitude Control Missions on Science and Earth Observation Satellites," 37th Annual AAS Guidance and Control Conference, Breckenridge, Colorado, 2014.

22. J. Jarrige, P. Thobois, C. Blanchard, P.-Q. Elias, D. Packan, L. Fallerini and G. Noci, "Thrust Measurements of the Gaia Mission Flight-Model Cold-Gas Thrusters," Journal of Propulsion and Power, vol. 30, no. 4, pp. 934-943, 2014.

23. G. Morris, N. Dunbar, P. Bianco and C. Edwards, "Design of a Cold-Gas Micropropulsion System for LISA Pathfinder," in 49th AIAA/ASME/SAE/ASEE Joint Propulsion Conference, San Jose, CA, 2013.

24. [Online]. Available: http://www.cubesat-propulsion.com/.

25. [Online]. Available: https://gomspace.com/Shop/subsystems/propulsion/default.aspx.

26. [Online]. Available: http://www.sitael.com/wp-content/uploads/2017/02/Cold-Gas-Micro-Propulsion-System.pdf.

27. [Online]. Available: http://www.moog.com/literature/Space_Defense/Spacecraft/ Propulsion/Proportional_Micro_Thruster.pdf.

28. E. T. Stoneking, Interviewee, Email Chain. [Interview]. 28 August 2017.

29. G. Henderson, "Managing Observatory Line-of-Sight Jitter (with an emphasis on micro-vibrations): A 'Jitter 101' Process Overview," tutorial presentation at 42nd Annual AAS Guidance and Control Conference, Breckenridge, Colorado, United States, February 2019.

30. R.L. Lucke, S.W. Sirlin, and A.M. San Martin, "New Definitions of Pointing Stability: AC and DC Effects," The Journal of the Astronautical Sciences, Vol. 40, No. 4, October-December, 1992, pp. 557-576.

31. G. Anderson et al, "Experimental Results from the ST7 Mission on LISA Pathfinder," Physical Review D 98, 102005 (2018).

32. [Online]. Available: https://directory.eoportal.org/web/eoportal/satellite-missions/l/lisa-pathfinder.

33. Carmain, A. et al., "Space Technology 7 Disturbance Reduction System—Precision Control Flight Validation," 2006 IEEE Aerospace Conference, Big Sky, MT, 2006, pp. 7. doi: 10.1109/AERO.2006.1655770.

34. R. Sanchez Maestro, A. Agenjo Diaz, D.A. Ardura Lumeras, L. Meijer, M. Saponara, C. Rosso, and G. Saavedra Criado, "Euclid Dark Universe Mission—High Stability and Pointing Performance Control," paper IAC-19-C1.6.1, 70th International Astronautical Congress, Washington D.C., October, 2019

35. F. Bouquet, interviewee, personal communication, 23 October, 2019

36. https://spaceflight101.com/lisa-pathfinder/cold-gas-micro-propulsion-system/

37. A. Wu, R. Chiang, "Quick-Look Feasibility Study of Micro Cold-Gas Thrusters for Precision Spacecraft Attitude Control," Aerospace Corp. report under contract no. NNL11AA01B, 10 November, 2017

38. P.Y. Bely, B.S. May, "The Pointing Stability of the Hubble Space Telescope and Proposed Concepts for the Pointing Control of the Next Generation Space Telescope (NGST)," IFAC proceedings Volume 25, Issue 22, September, 1992, pp. 457-462

39. L. Blackmore et al, "Instrument Pointing Capabilities: Past, Present, and Future", paper AAS 11-091, AAS Guidance and Control Conference, Breckenridge, Colorado, February 4, 2011

40. https://science.gsfc.nasa.gov/sed/index.cfm?fuseAction=projects.view&navOrgCode=660&navTab=nav_about_us&project_id=392

41. E. Stoneking vugraph package, "StarShade Rendezvous Spacecraft Design Review: Attitude Control System," Oct 19, 2017

42. HabEx Final Report, "HabEx: Exploring New Worlds, Understanding Our Universe", https://www.jpl.nasa.gov/habex/documents/

43. J. Ziemer, Interviewee, Email Chain. [Interview]. 23 Oct., 2020

Appendices

A. Plots of Simulation Results

B. Bode and Nichols Plots for Micro-Thruster and Reaction Wheel Control

Appendix A: Plots of Simulation Results

A.1   Observatory 2 without Isolator

Case 8: Colloid Thruster Pointing

Observatory 2

Case 8 - Pointing Error
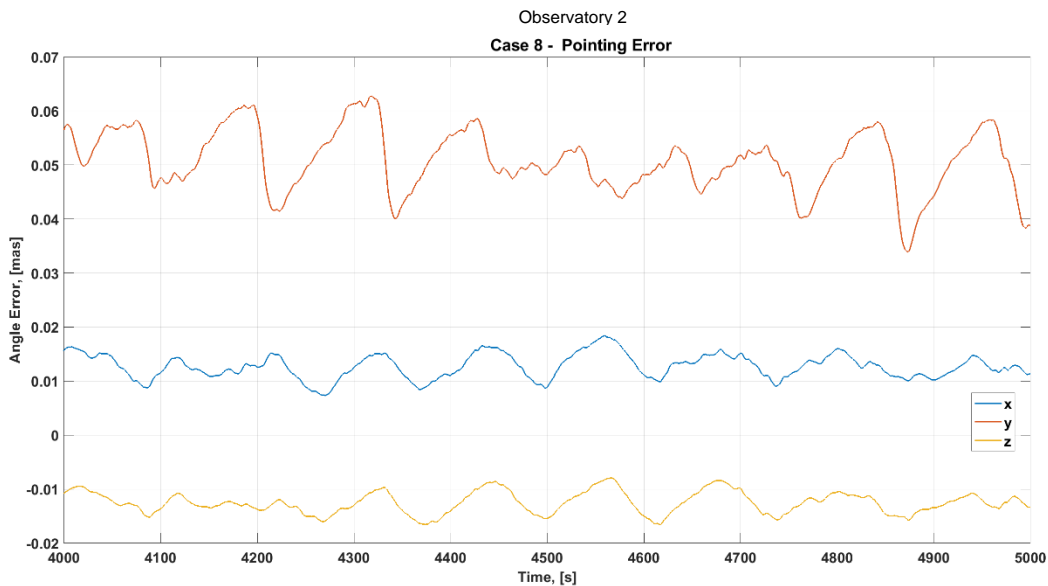
Figure A.1-1. Case 8 Steady-State Pointing Error in mas

- No slew.
- Colloid micro-thrusters for fine pointing only; wheels off.

Observatory 2

Case 8 - Thrust Command
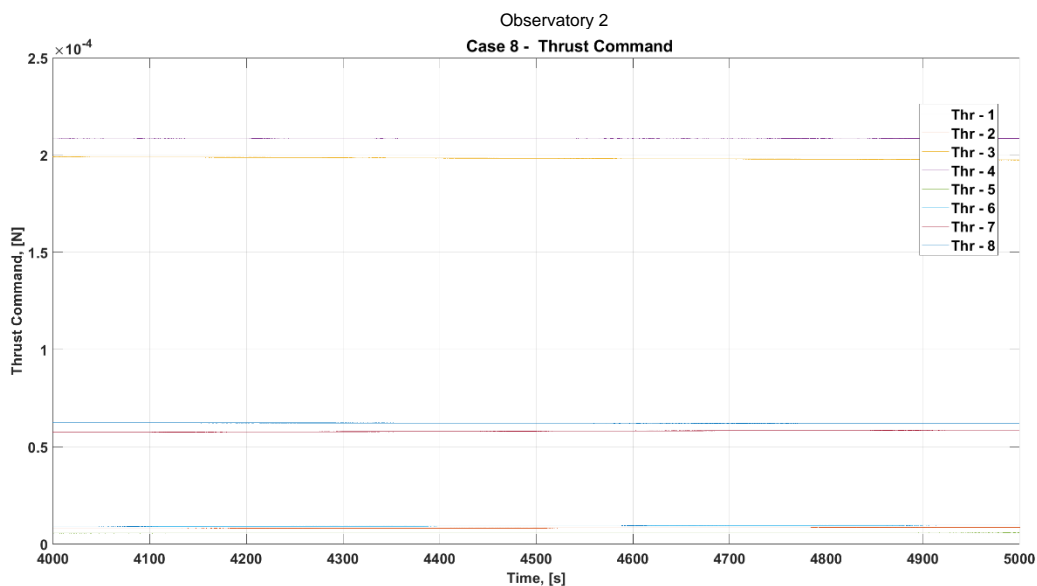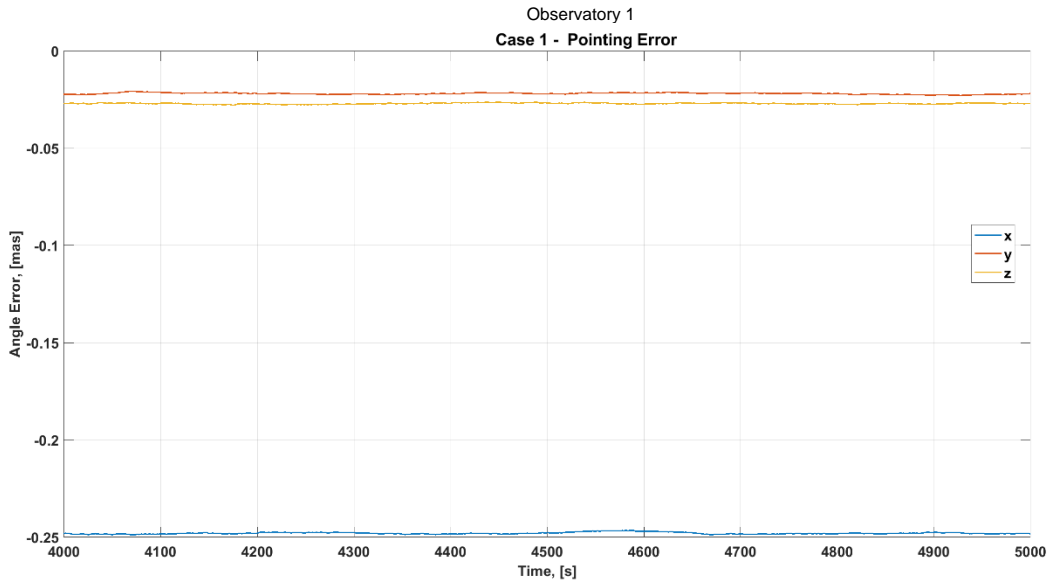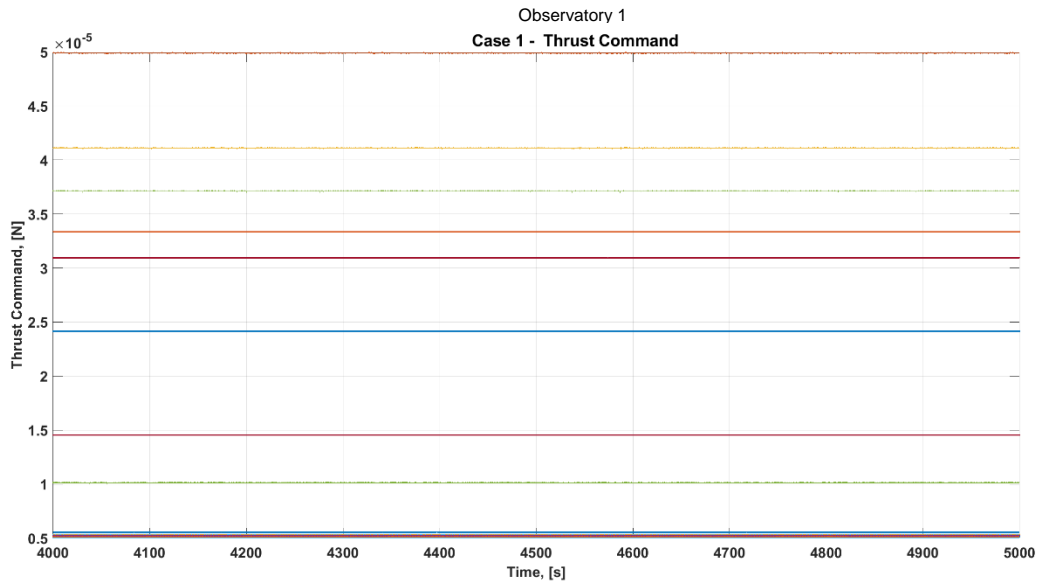

Figure A.1-2. Case 8 Steady-State Thrust Commands

Case 9: Reaction Wheel Pointing

Observatory 2
Case 9 - Pointing Error
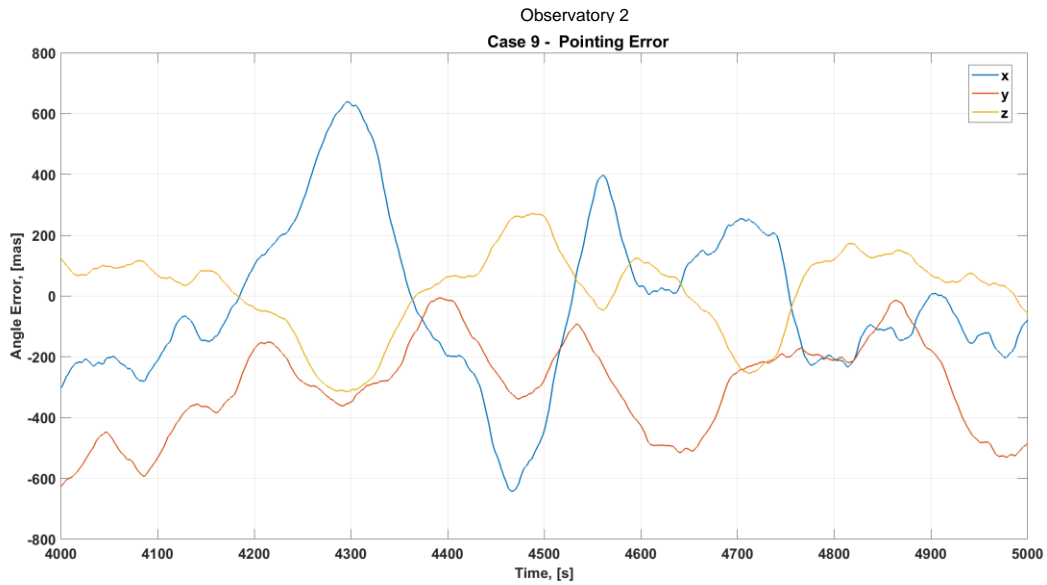
Figure A.1-3. Case 9 Steady-State Pointing Error in mas

- No slew.
- Reaction wheel fine pointing only with 100 RPM bias; micro-thrusters off.
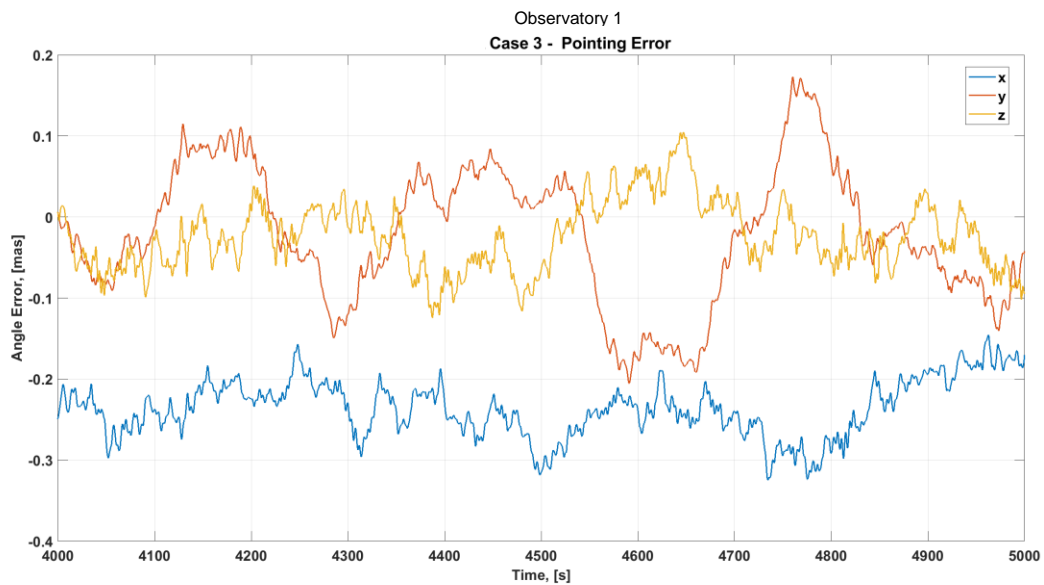
Case 10: Cold Gas Thruster Pointing

Observatory 2
Case 10 - Pointing Error
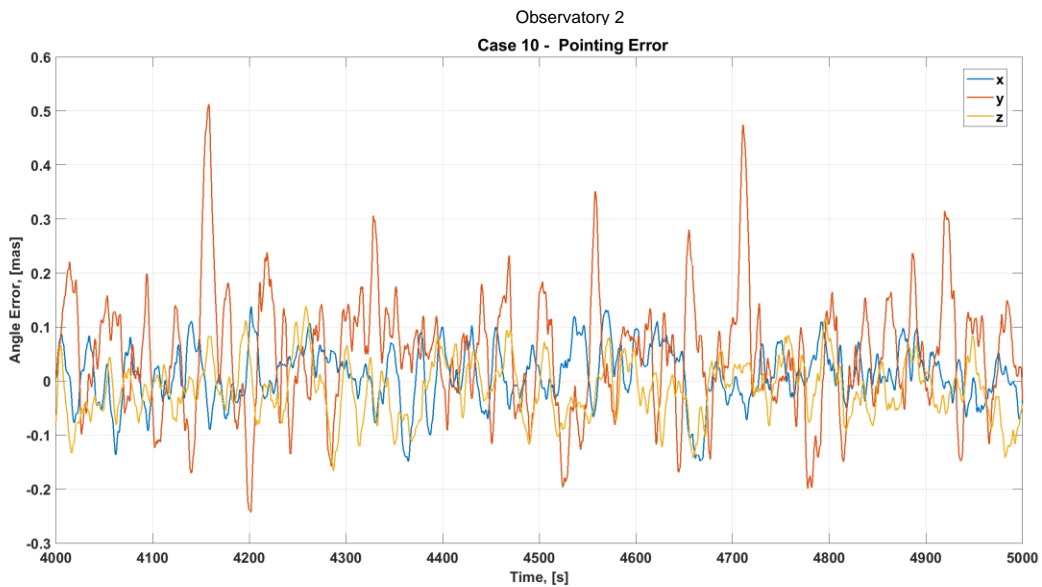
Figure A.1-4. Case 10 Steady-State Pointing Error in mas

- No slew.
- Cold gas micro-thrusters for fine pointing only; wheels off.
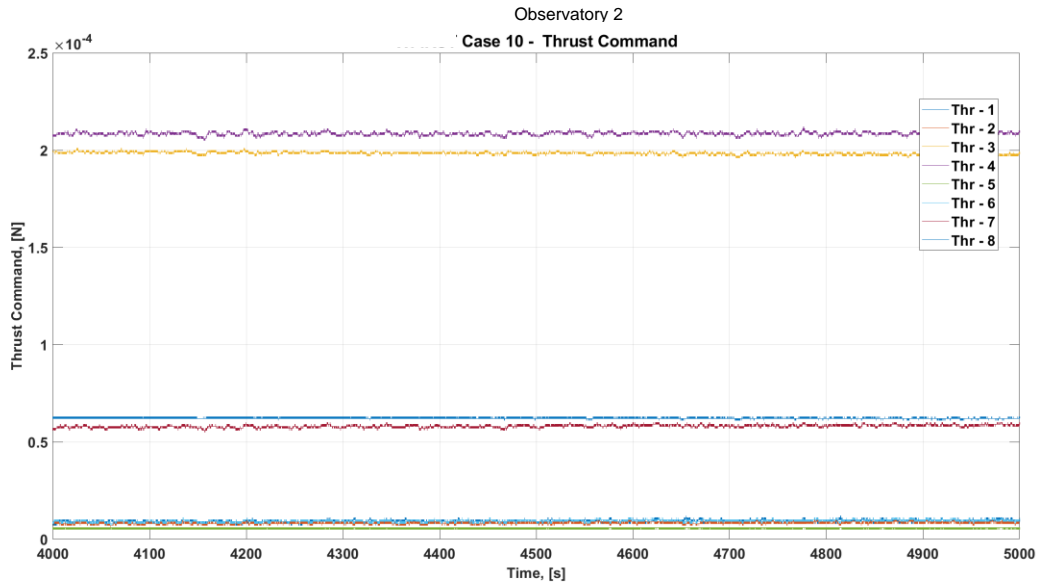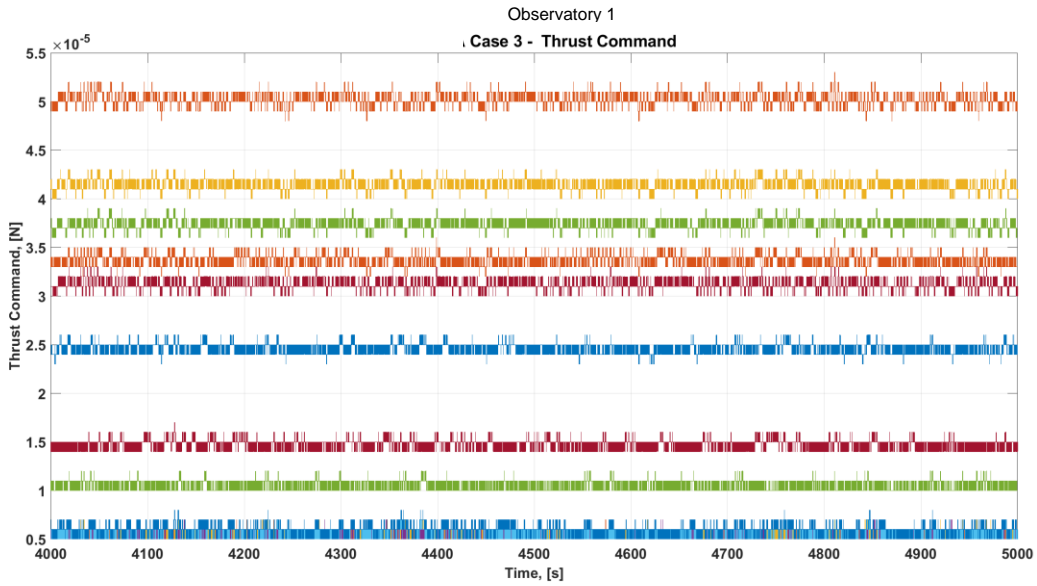
Figure A.1-5. Case 10 Steady-State Thrust Command
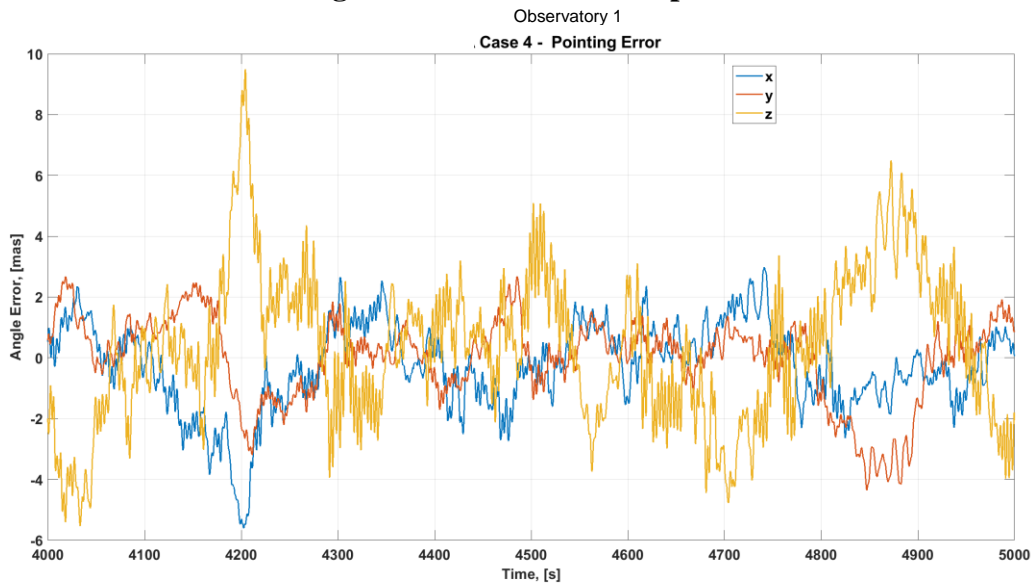
Case 11: Colloid Thruster Pointing with Constant Wheel Speed
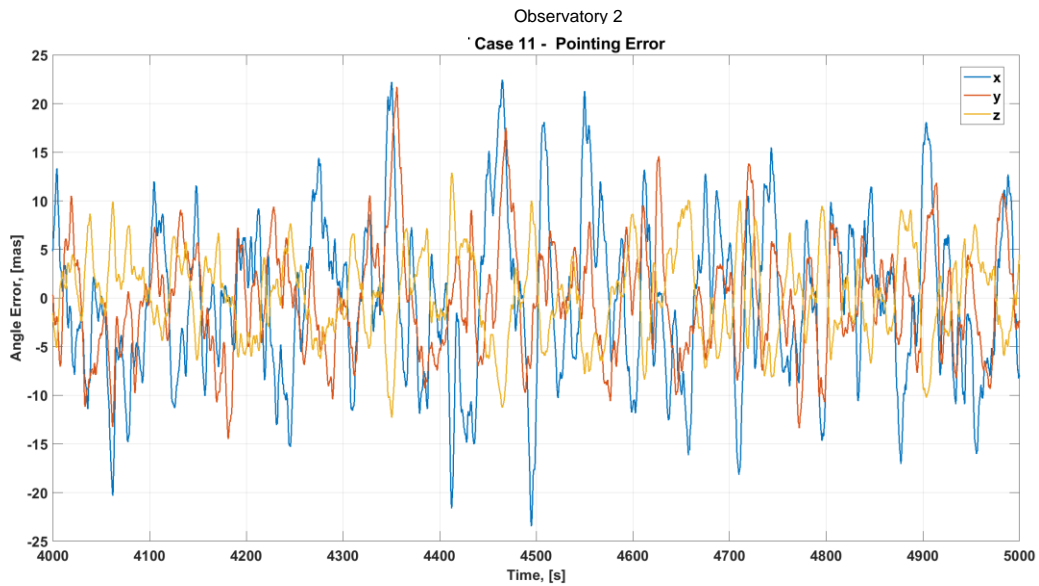
Figure A.1-6. Case 11 Steady-State Pointing Error in mas

- No slew.
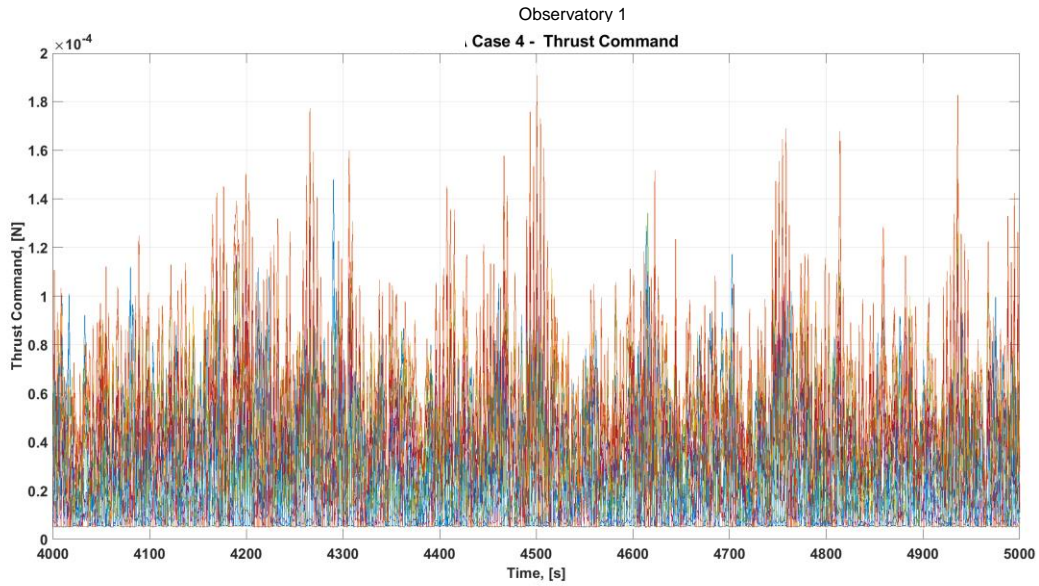- Colloid micro-thrusters for fine pointing only; 100 RPM wheel bias.

Observatory 2

Case 11 - Thrust Command
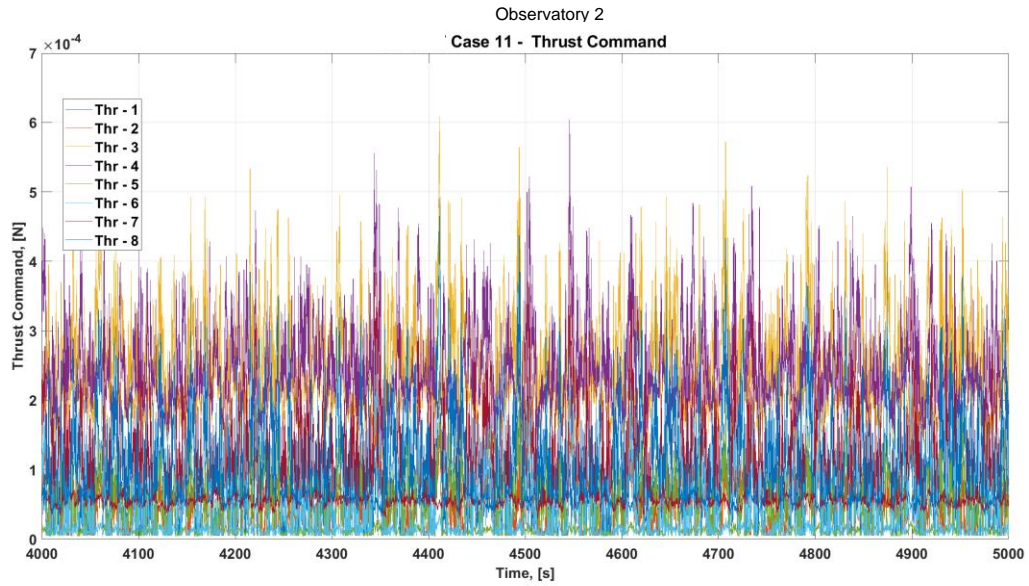
Figure A.1-7. Case 11 Steady-State Thrust Command

Case 12: Simultaneous RWA and Colloid Thruster Pointing

Observatory 2
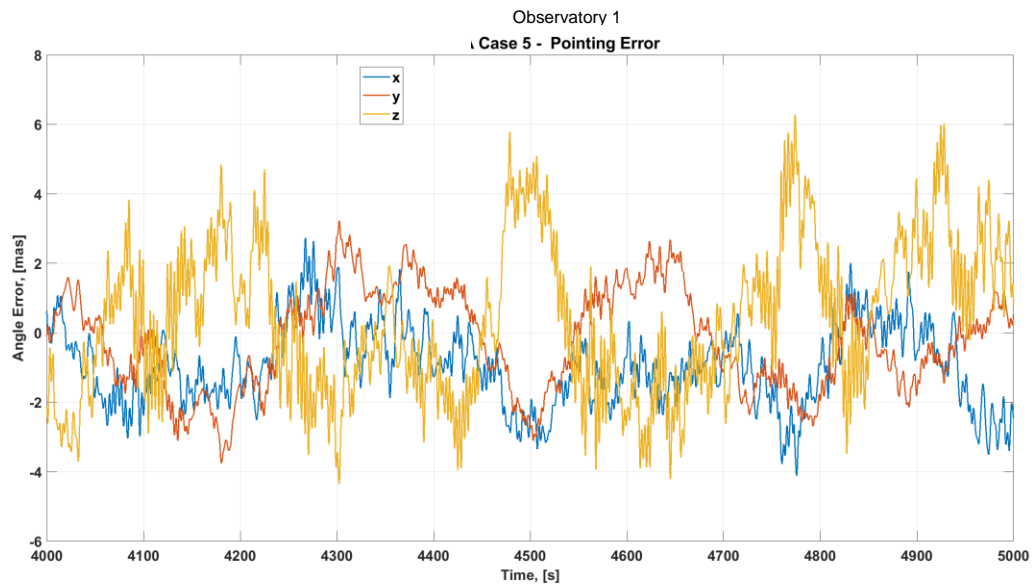
Case 12 - Pointing Error
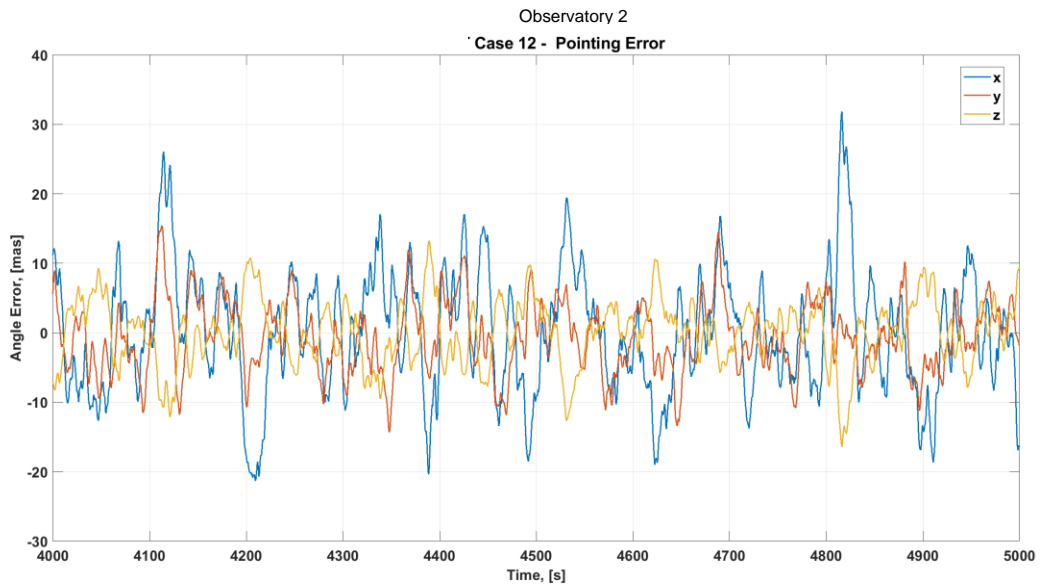
Figure A.1-8. Case 12 Steady-State Pointing Error in mas

- No slew.
- Colloid micro-thrusters and RWA used for fine pointing; 100 RPM wheel bias.
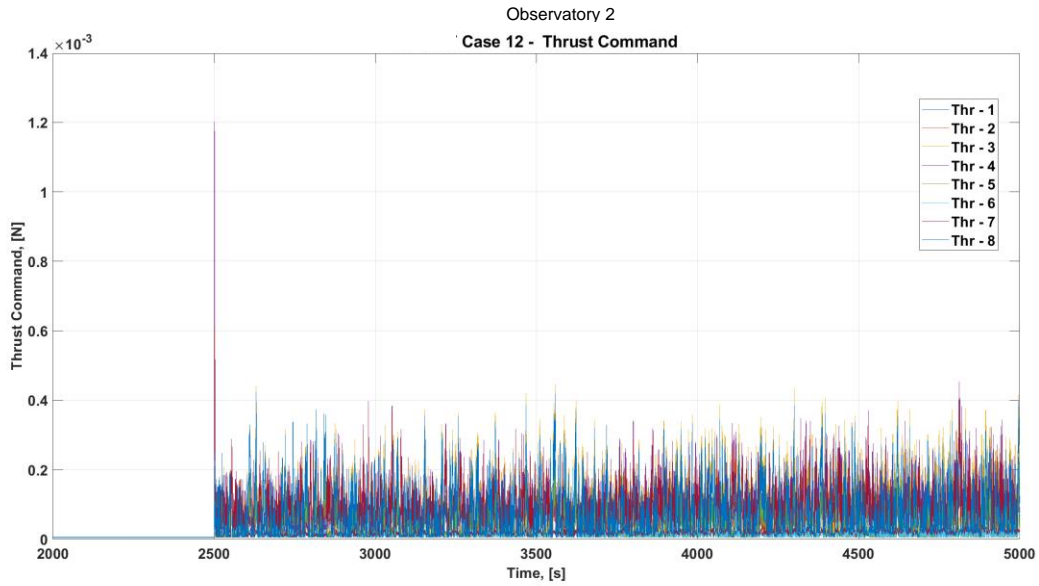
Figure A.1-9. Case 12 Thrust Command

Case 13: Cold Gas Thruster Pointing with Constant Wheel Speed
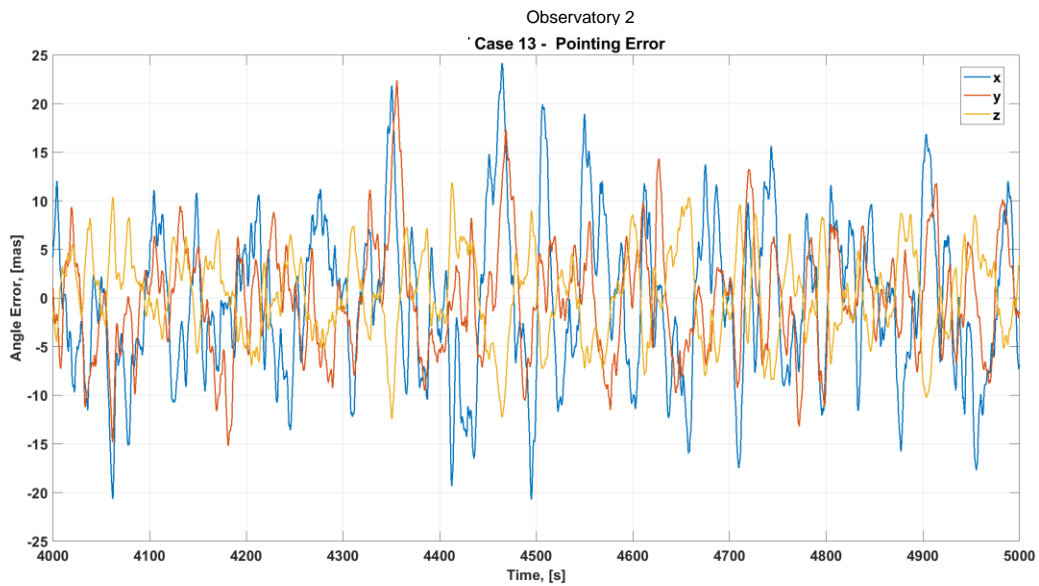
Figure A.1-10. Case 13 Steady-State Pointing Error in mas

- No slew.
- Cold gas micro-thrusters for fine pointing only; 100 RPM wheel bias.

Observatory 2
Case 13 - Thrust Command
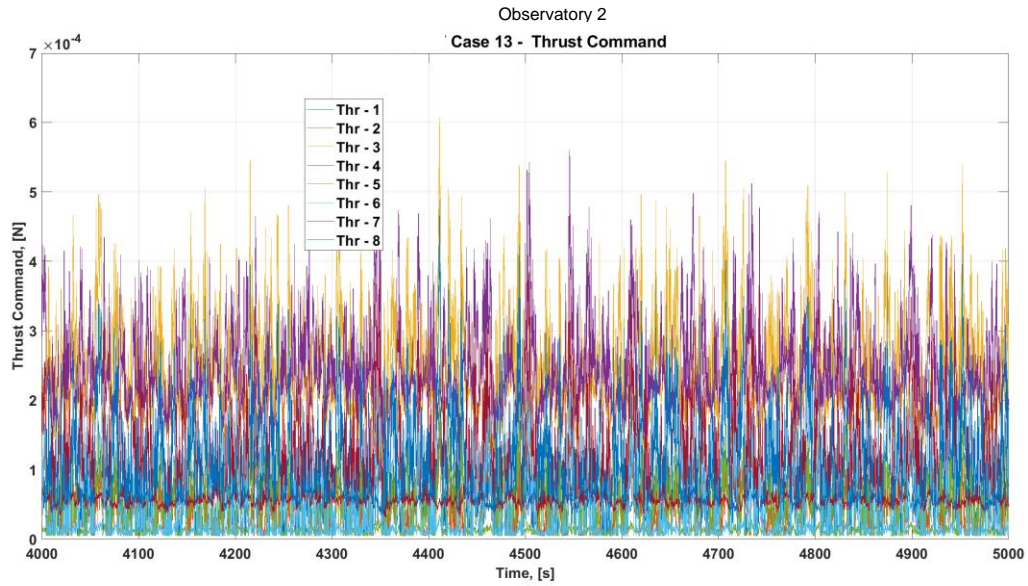
Figure A.1-11. Case 13 Steady-State Thrust Command

Case 14: Simultaneous RWA and Cold Gas Thruster Pointing

Observatory 2
Case 14 - Pointing Error
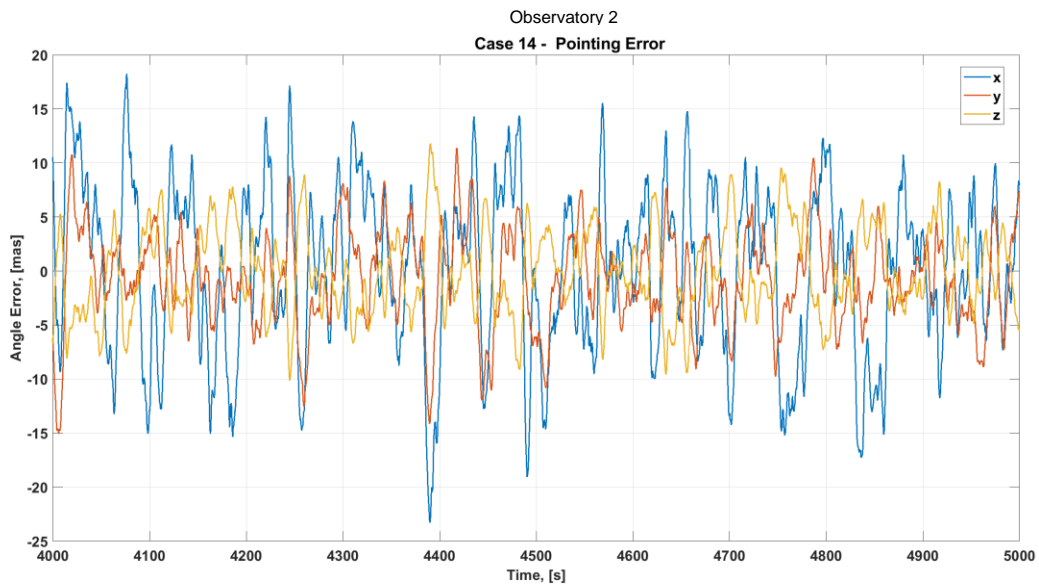
Figure A.1-12. Case 14 Steady-State Pointing Error in mas

- No slew.
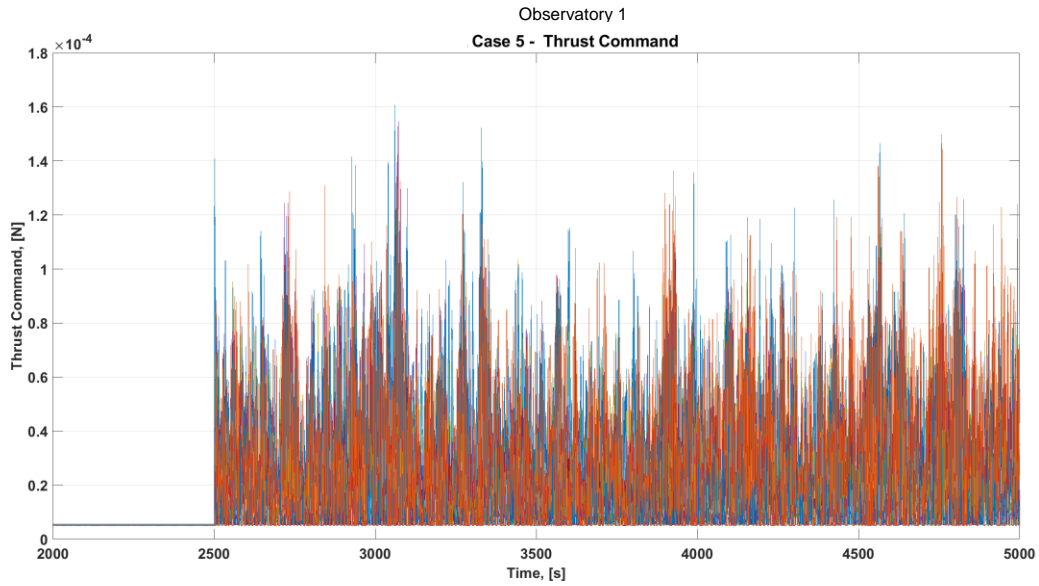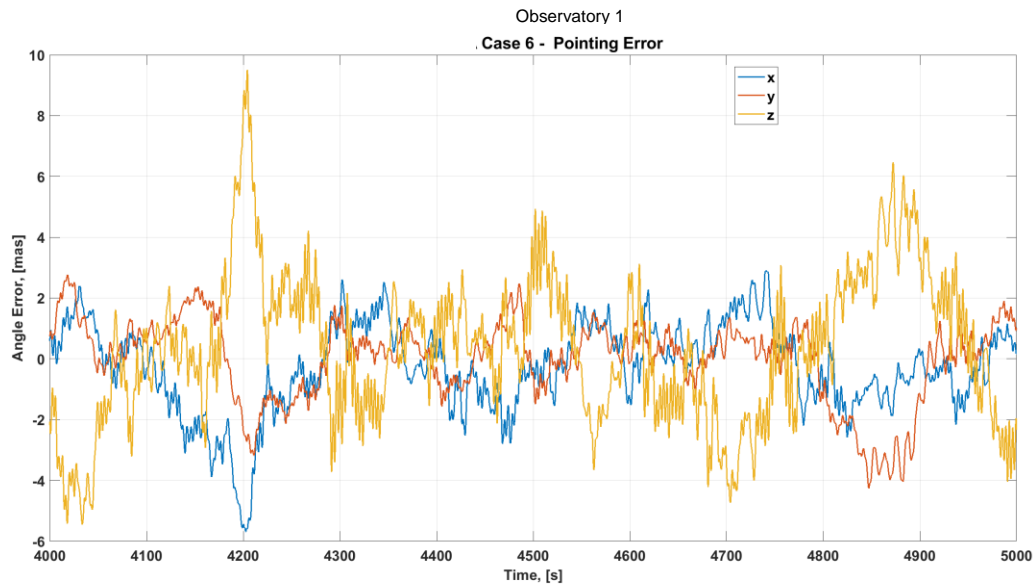- Cold gas micro-thrusters and RWA used for fine pointing; 100 RPM wheel bias.
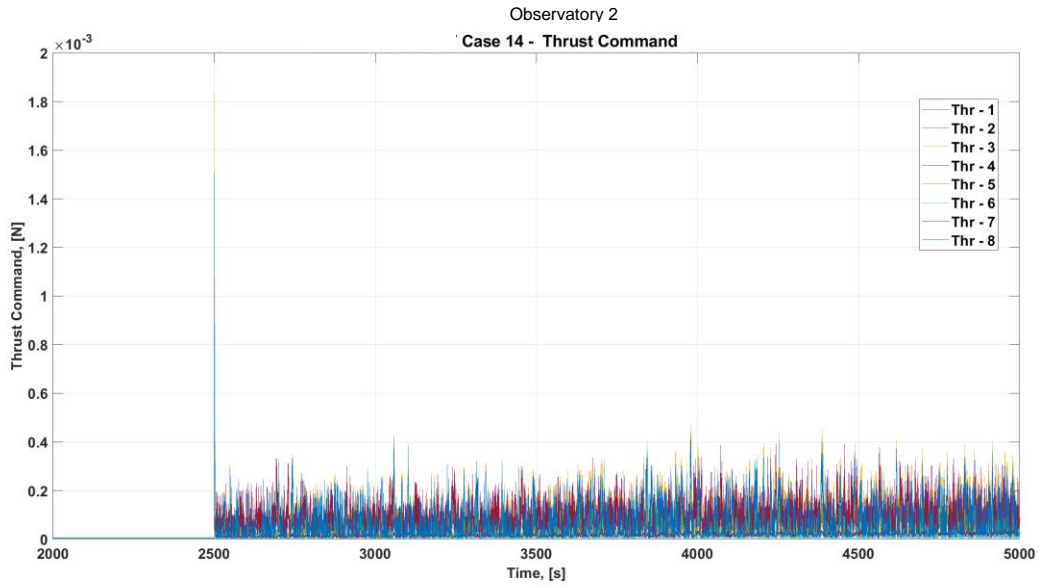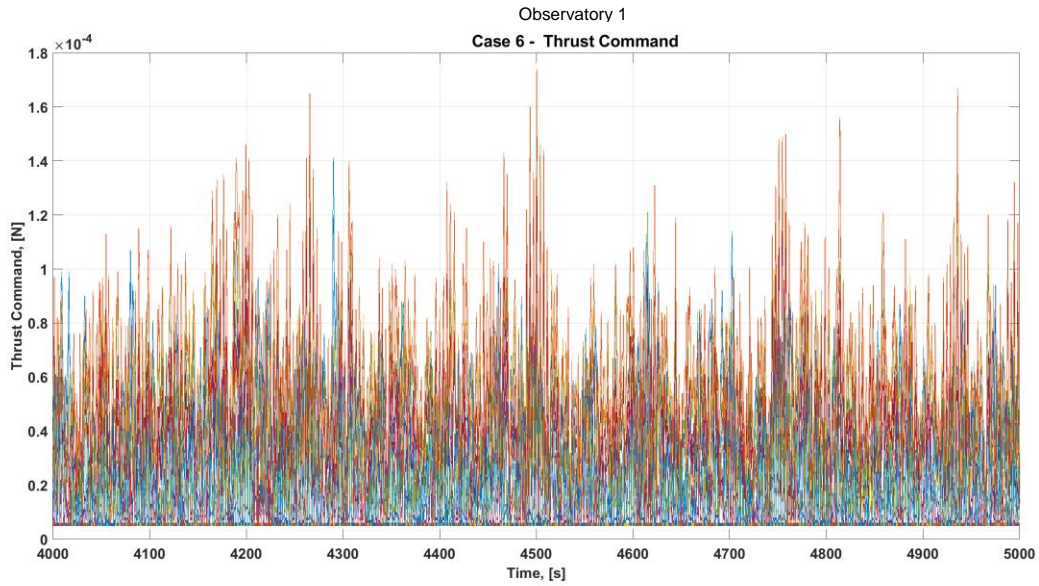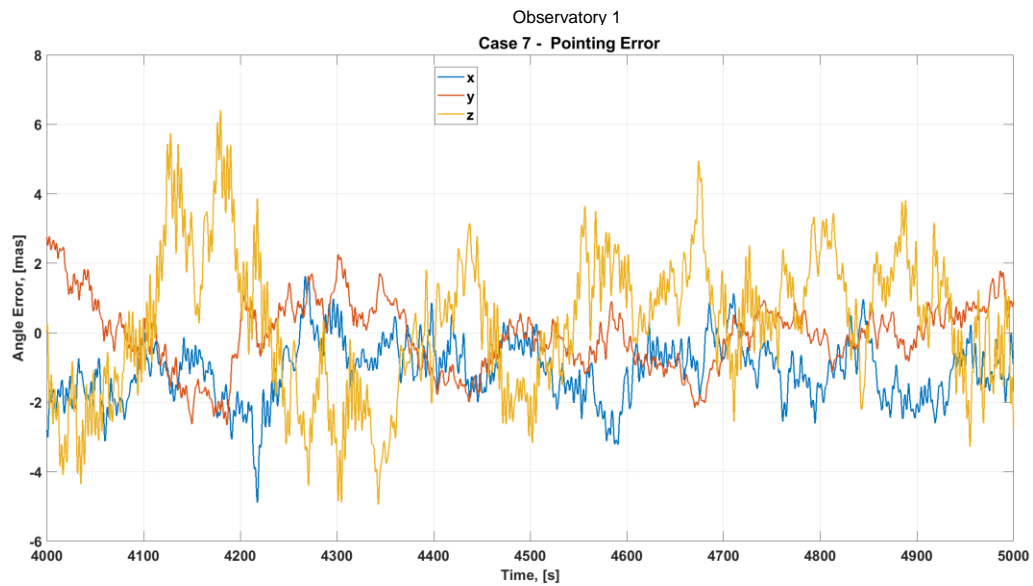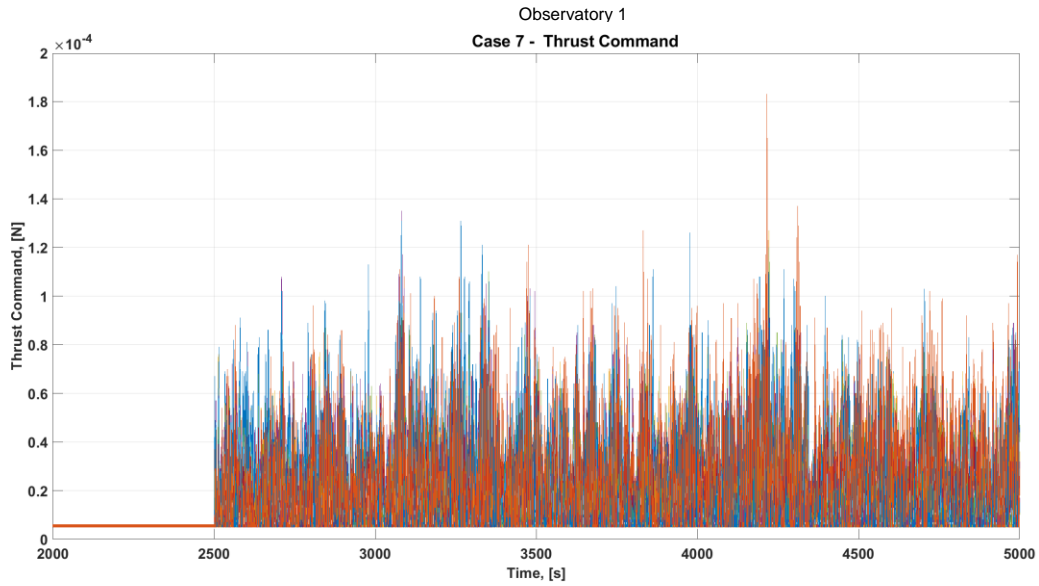
Figure A.1-13. Case 14 Thrust Command

Case 16: RCS Thruster Slew to Colloid Thruster Pointing
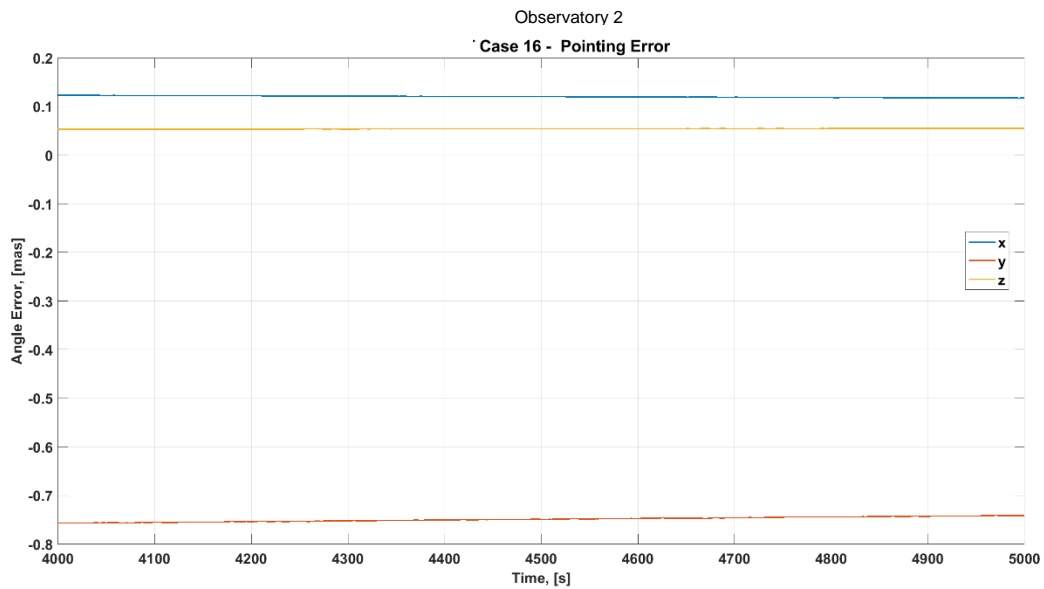
Figure A.1-14. Case 16 Steady-State Pointing Error in mas

- Slew by RCS thrusters to [-5,10,15] deg; transition to colloid thruster pointing.
- Wheels off.
- Increased maximum thrust to avoid saturation (see below).

Case 16 - Thrust Command
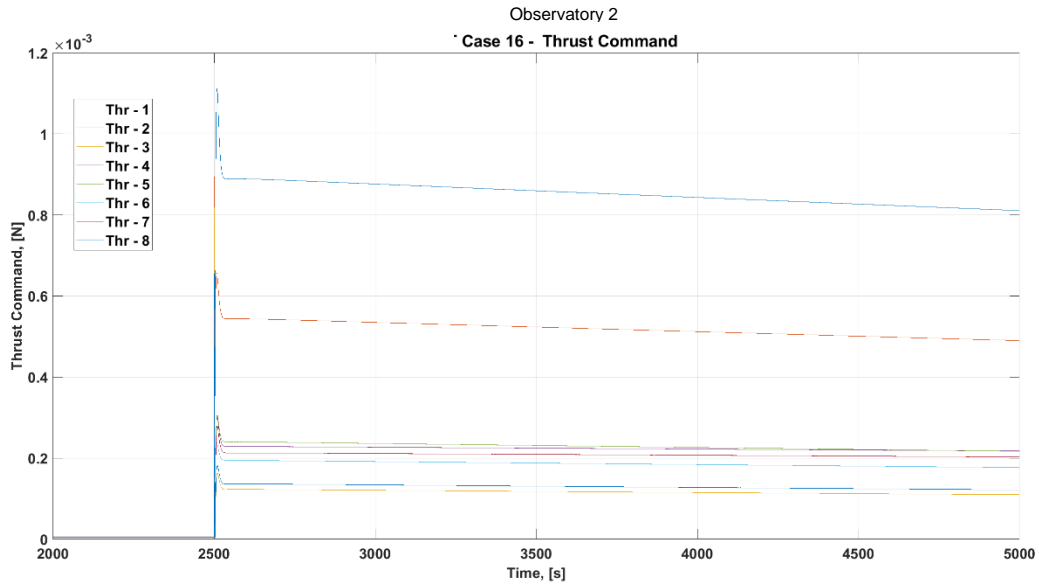
Figure A.1-15. Case 16 Thrust Command

Case 18: RWA Slew to Colloid Thruster Pointing (Zero Wheel Speed Bias)
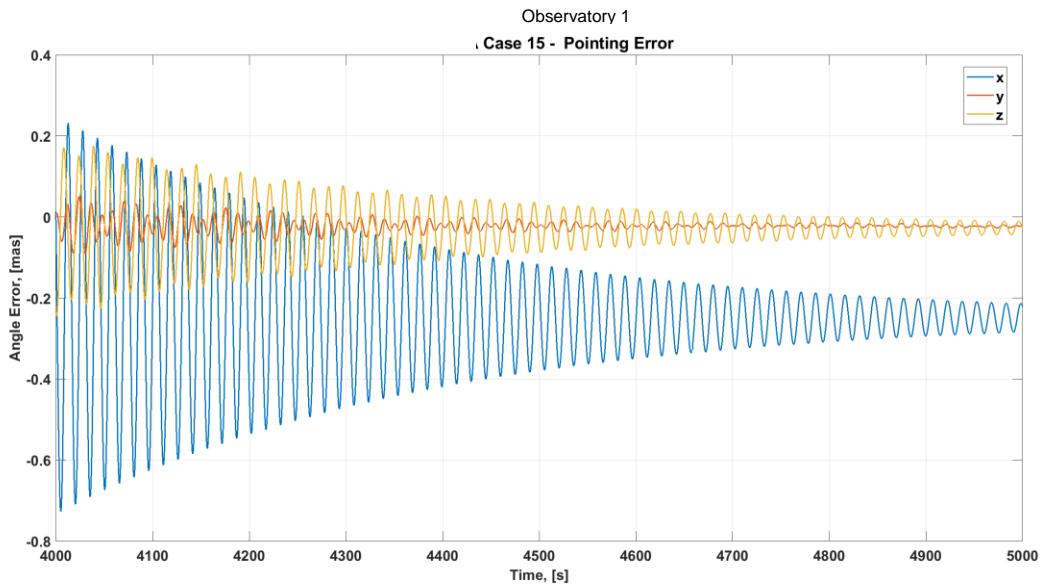
Observatory 2

Case 18 - Pointing Error
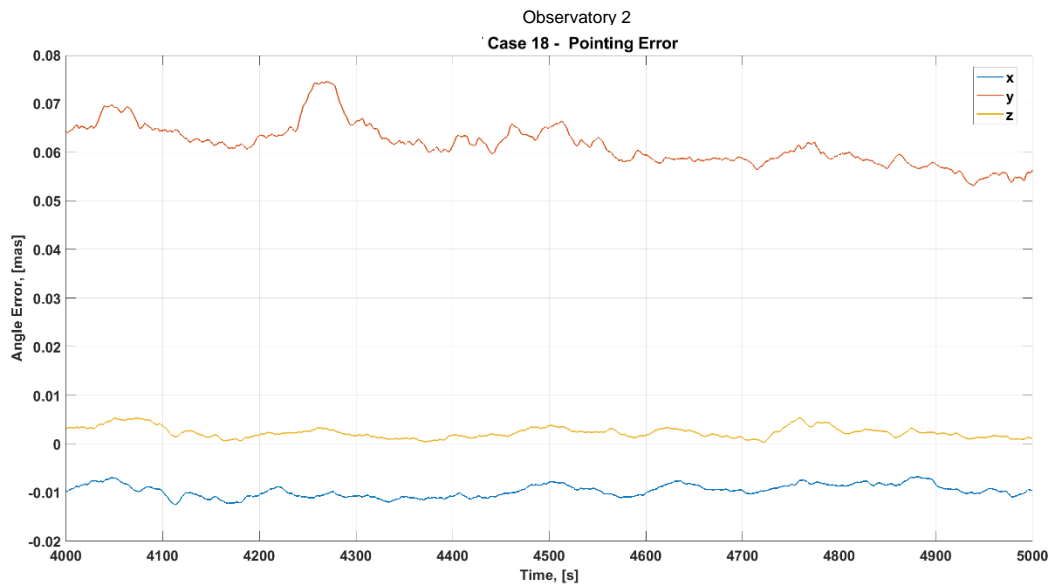
Figure A.1-16. Case 18 Steady-State Pointing Error in mas

- Slew by RWA to [-5,10,15] deg; transition to colloid thruster fine pointing.
- 0 RPM wheel speed bias.
- Increased maximum thrust to avoid saturation (see below).
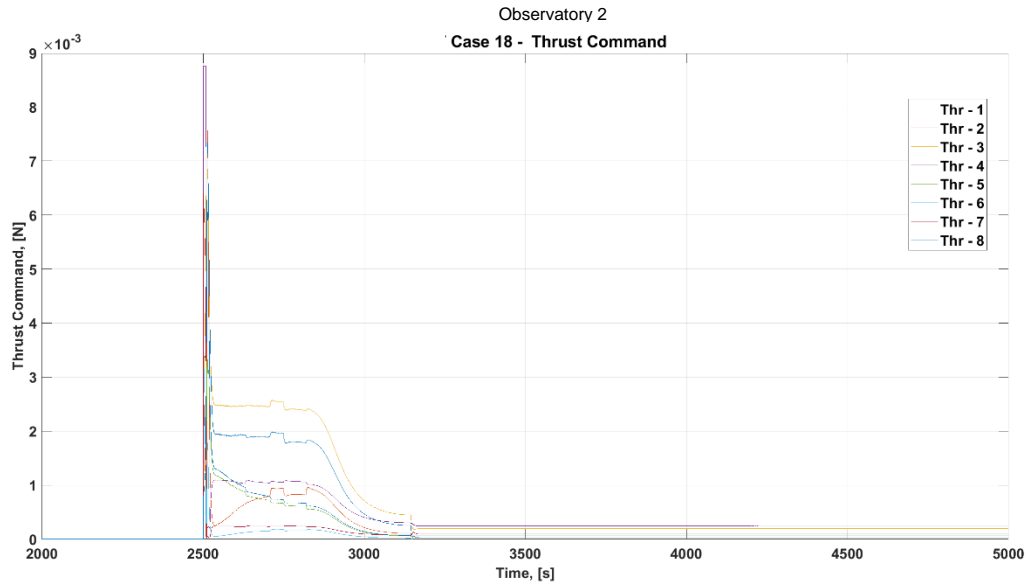
Figure A.1-17. Case 18 Thrust Command
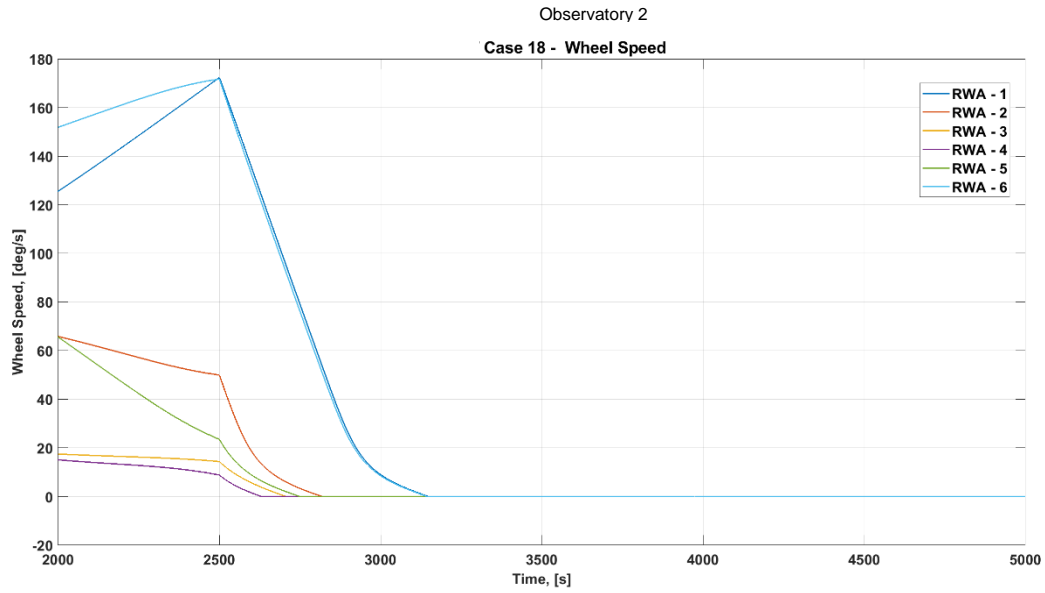
Figure A.1-18. Case 18 Wheel Speed

Case 20: RWA Slew to Simultaneous Colloid Pointing

Figure A.1-19. Case 20 Steady-State Pointing Error in mas

- Slew by RWA to [-5,10,15] deg; transition to simultaneous colloid thruster fine pointing.
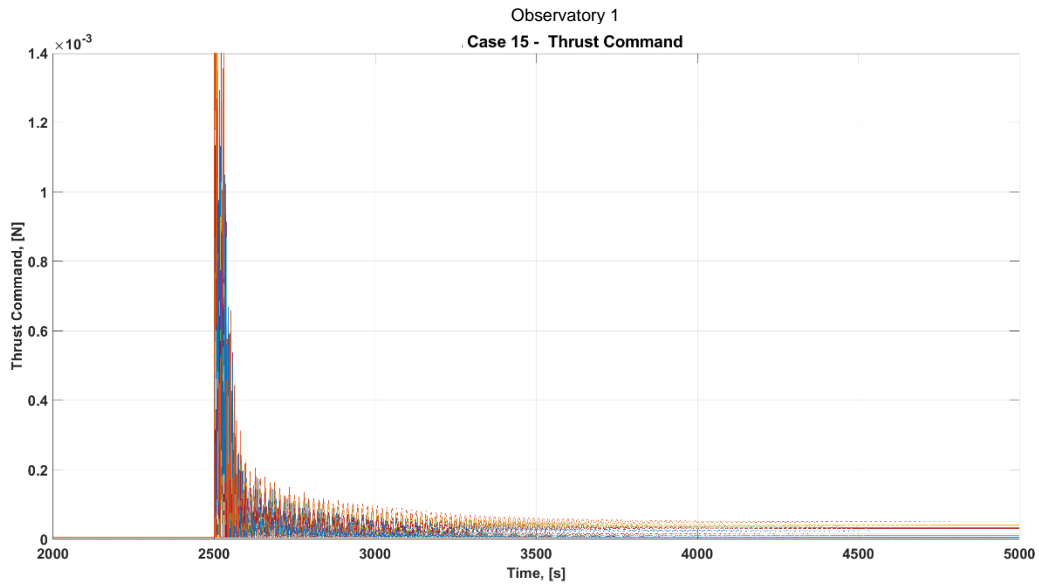- 100 RPM wheel speed bias.
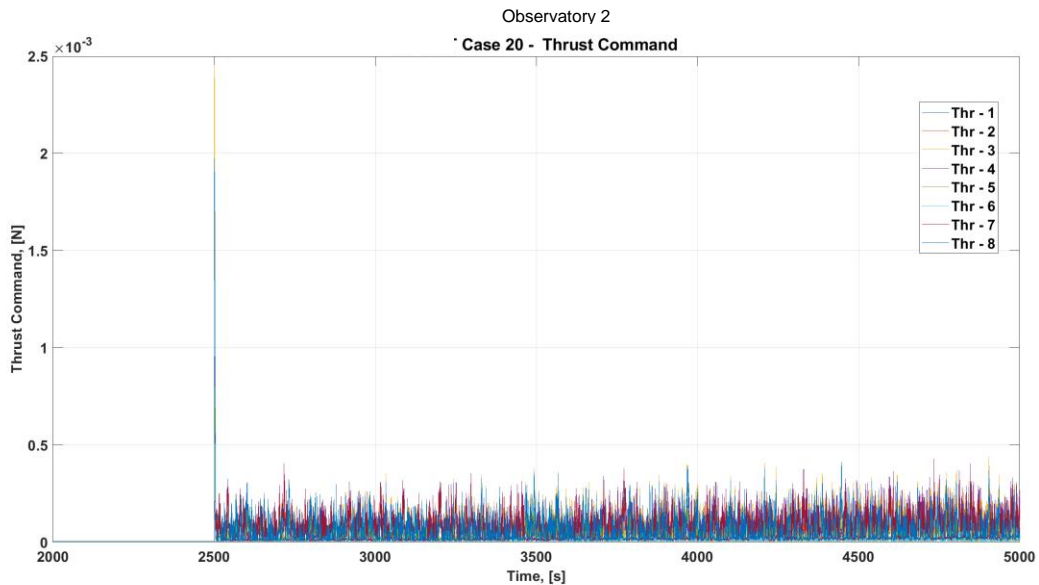
Figure A.1-20. Case 20 Thrust Command

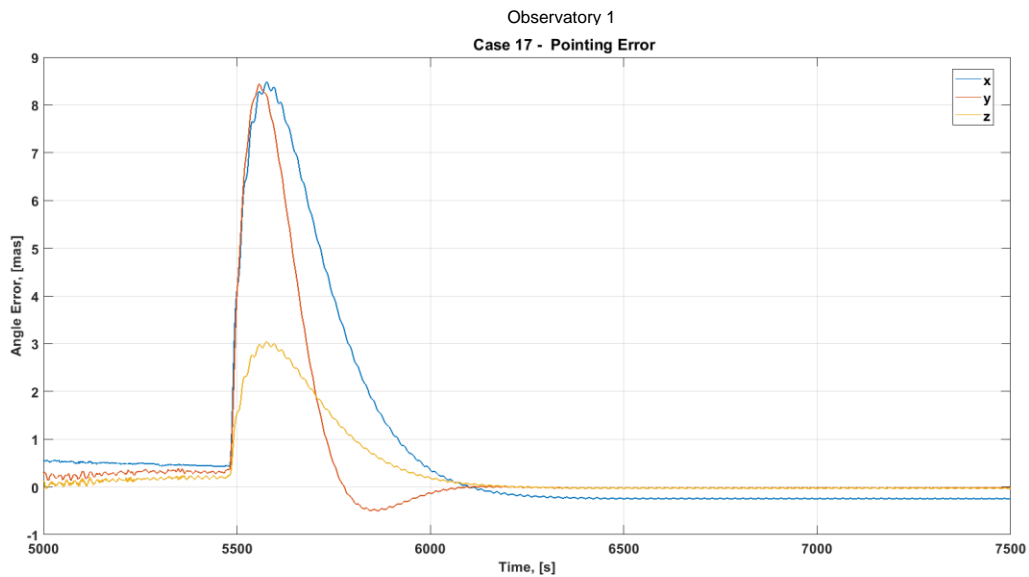**Case 22: RWA Slew to Colloid Thruster Pointing (Wheel Speed Hold)**
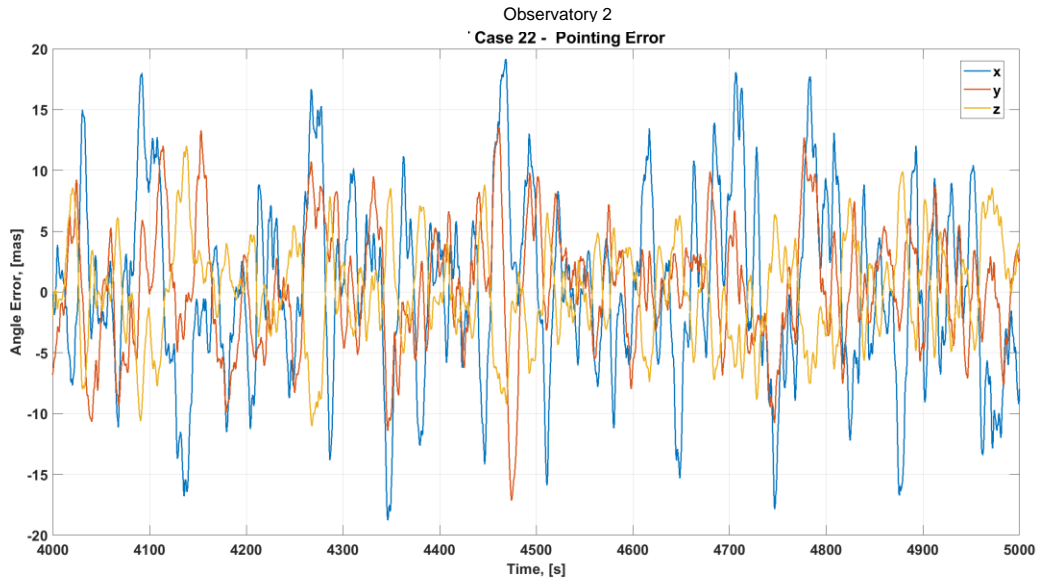
Figure A.1-.21 Case 22 Steady-State Pointing Error in mas

- Slew by RWA to [-5,10,15] deg; transition to colloid thruster fine pointing.
- 100 RPM wheel speed bias held at transition.
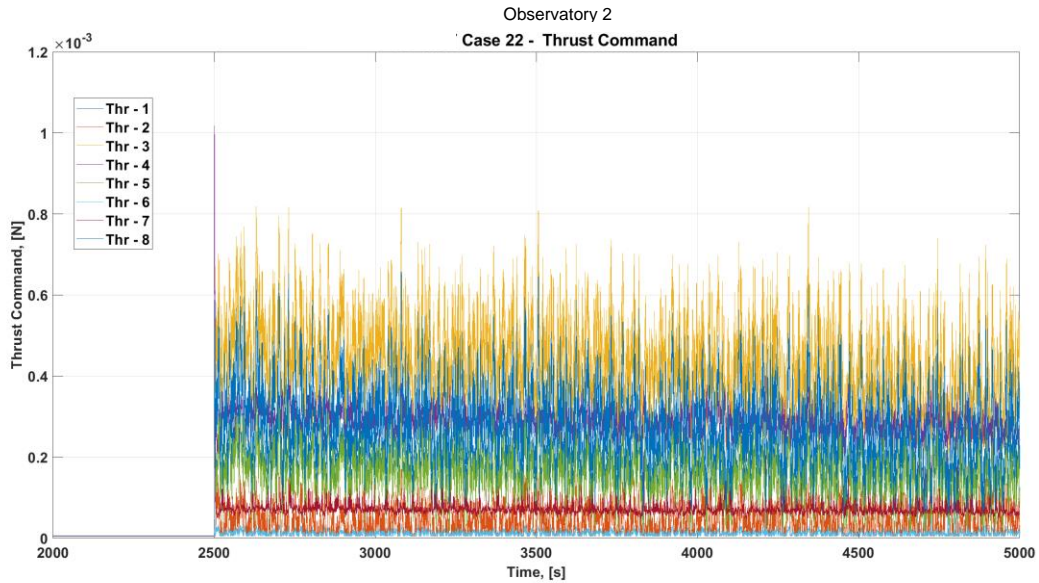
Figure A.1-22. Case 22 Thrust Command

Case 24: RCS Thruster Slew to Cold Gas Thruster Pointing

Figure A.1-23. Case 24 Steady-State Pointing Error in mas

- Slew by RCS thrusters to [-5,10,15] deg; transition to cold gas thruster pointing.
- Wheels off.
- Increased maximum thrust to avoid saturation (see below).
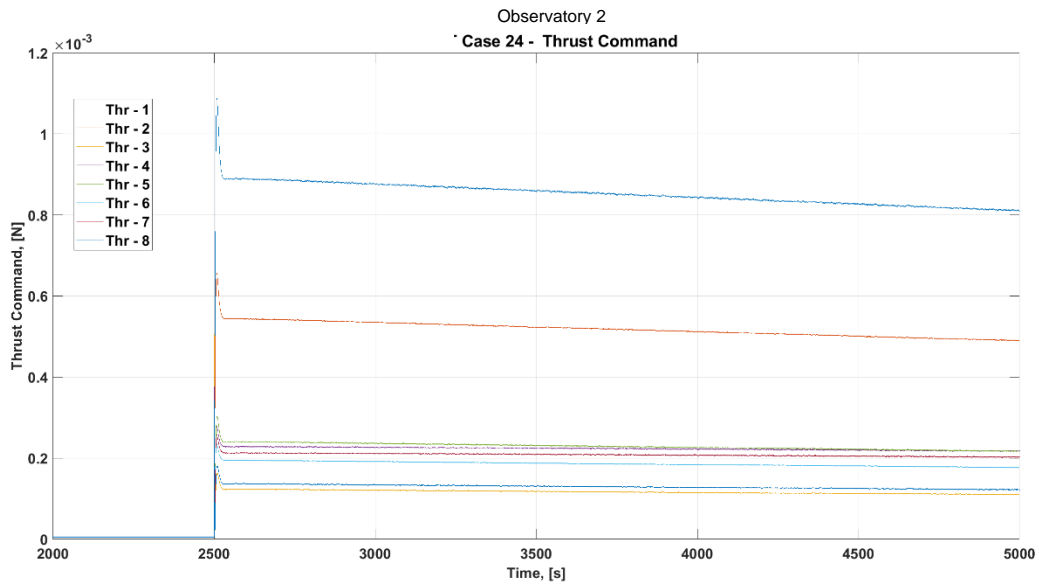
Figure A.1-24. Case 24 Thrust Command

Case 26: RWA Slew to Cold Gas Thruster Pointing (Zero Wheel Speed Bias)
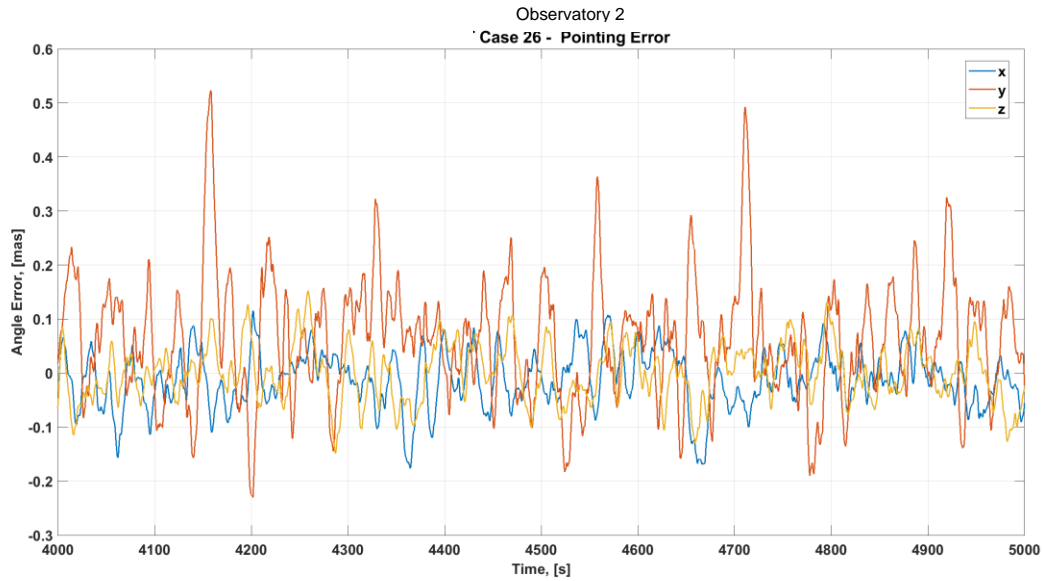
Figure A.1-25. Case 26 Steady-State Pointing Error in mas

- Slew by RWA to [-5,10,15] deg; transition to cold gas thruster fine pointing.
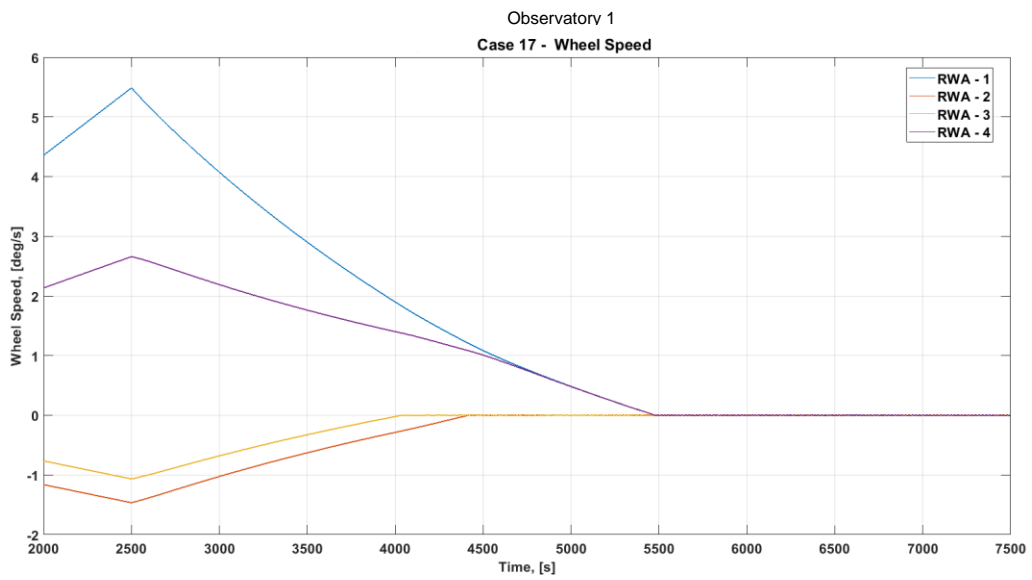- 0 RPM wheel speed bias.
- Increased maximum thrust to avoid saturation (see below).
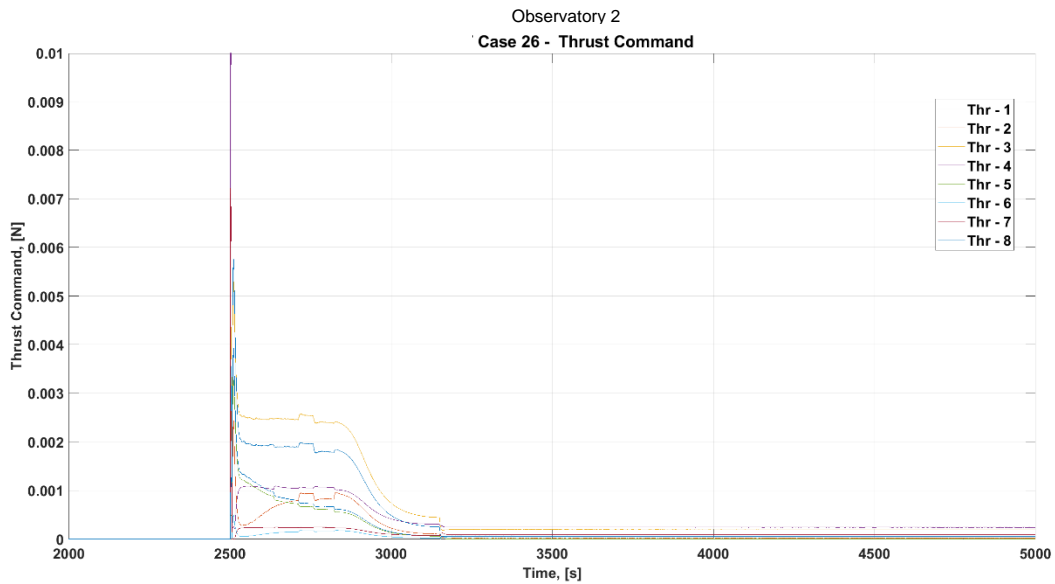
Figure A.1-26. Case 26 Thrust Command

Observatory 2
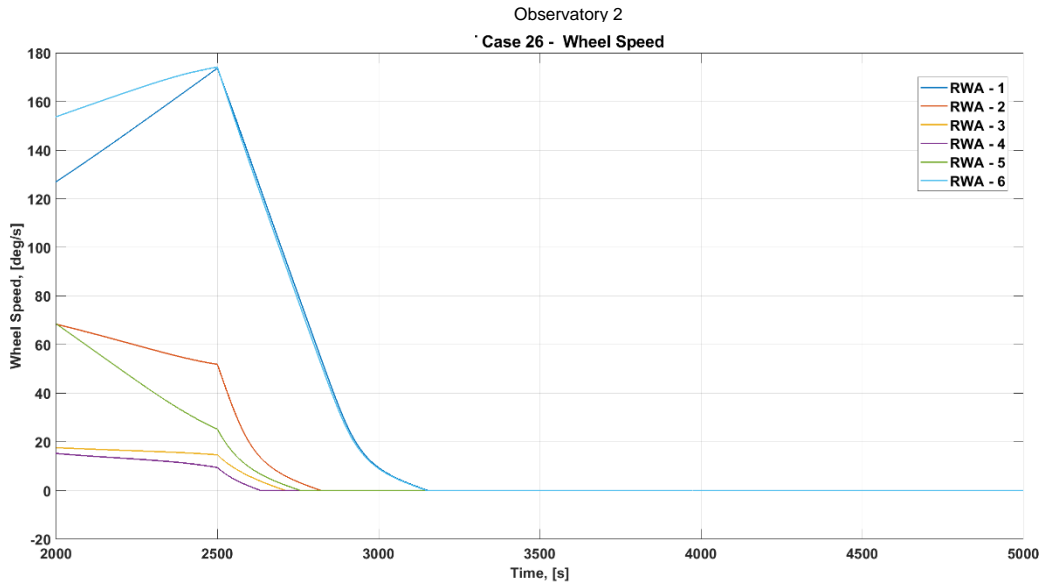
Case 26 - Wheel Speed

Figure A.1-27. Case 26 Wheel Speed

Case 28: RWA Slew to Simultaneous Cold Gas Pointing

Observatory 2
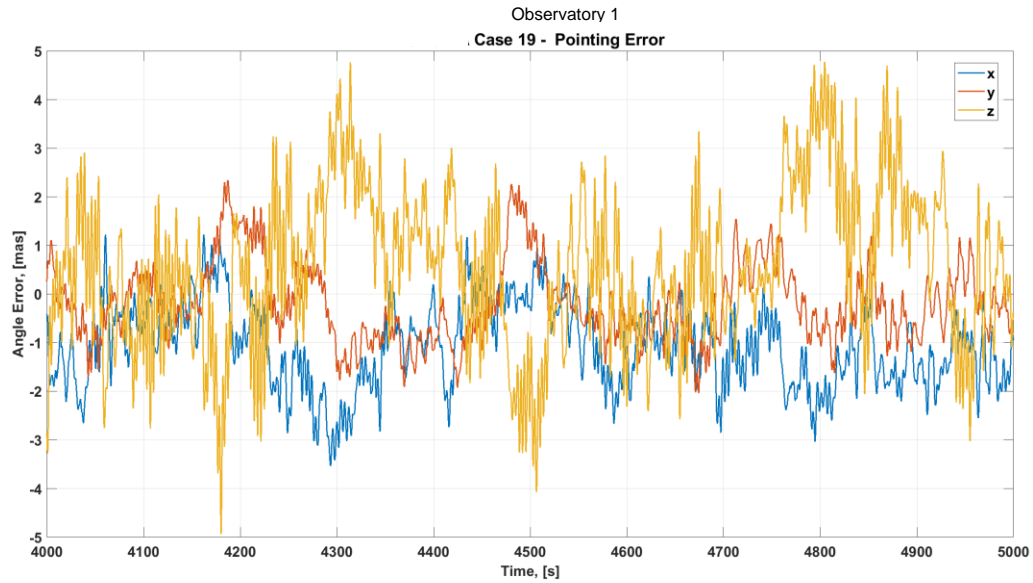
Case 28 - Pointing Error
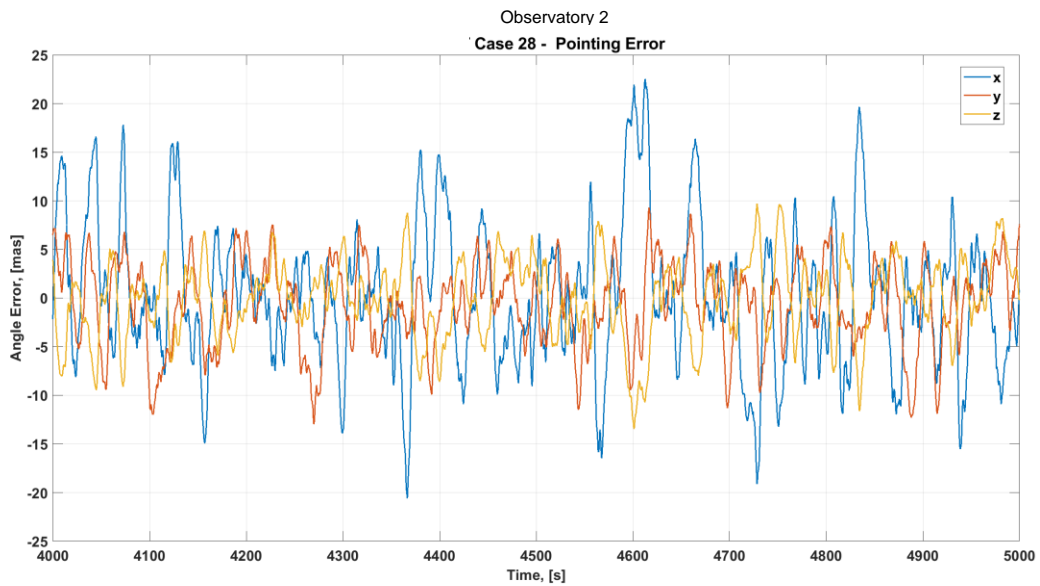
Figure A.1-28. Case 28 Steady-State Pointing Error in mas

- Slew by RWA to [-5,10,15] deg; transition to simultaneous cold gas thruster fine pointing.
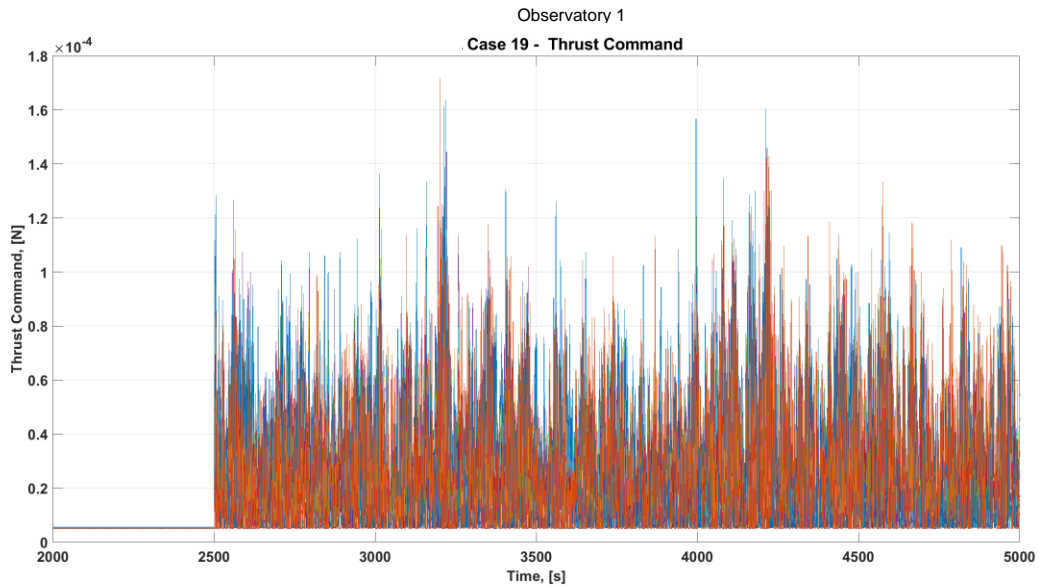- 100 RPM wheel speed bias.
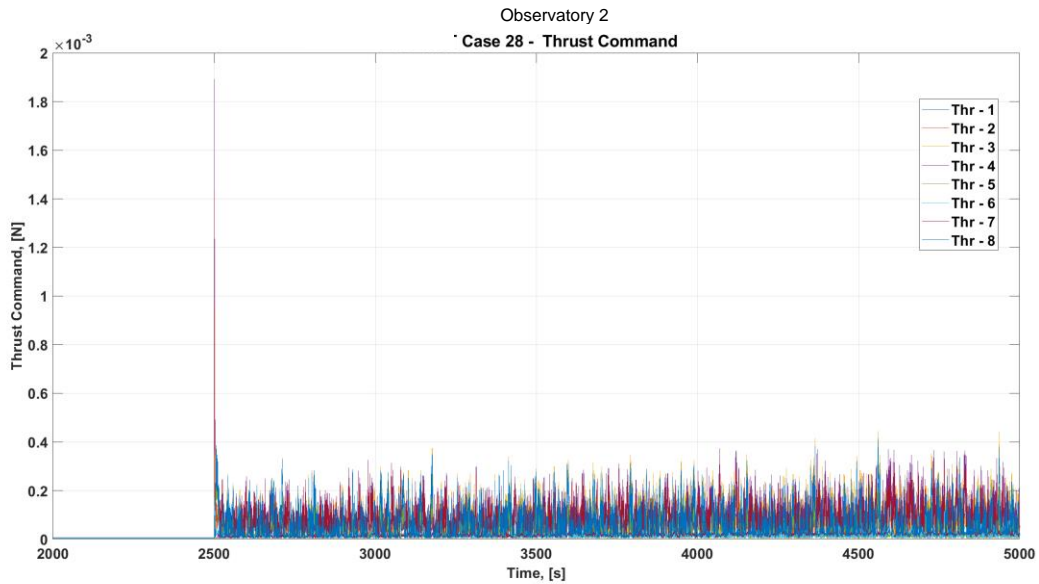
Figure A.1-29. Case 28 Thrust Command

Case 30: RWA Slew to Cold Gas Thruster Pointing (Wheel Speed Hold)
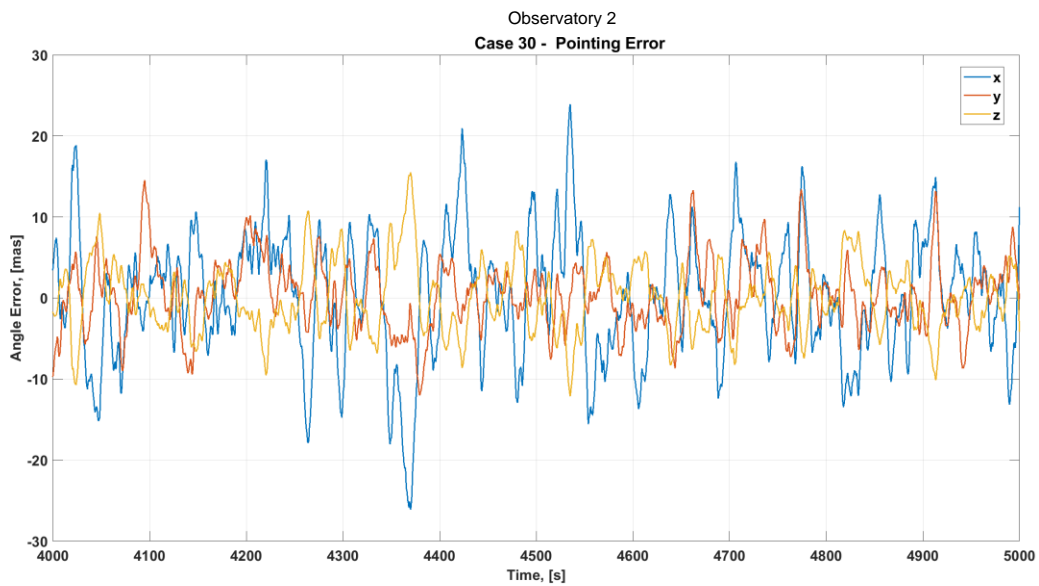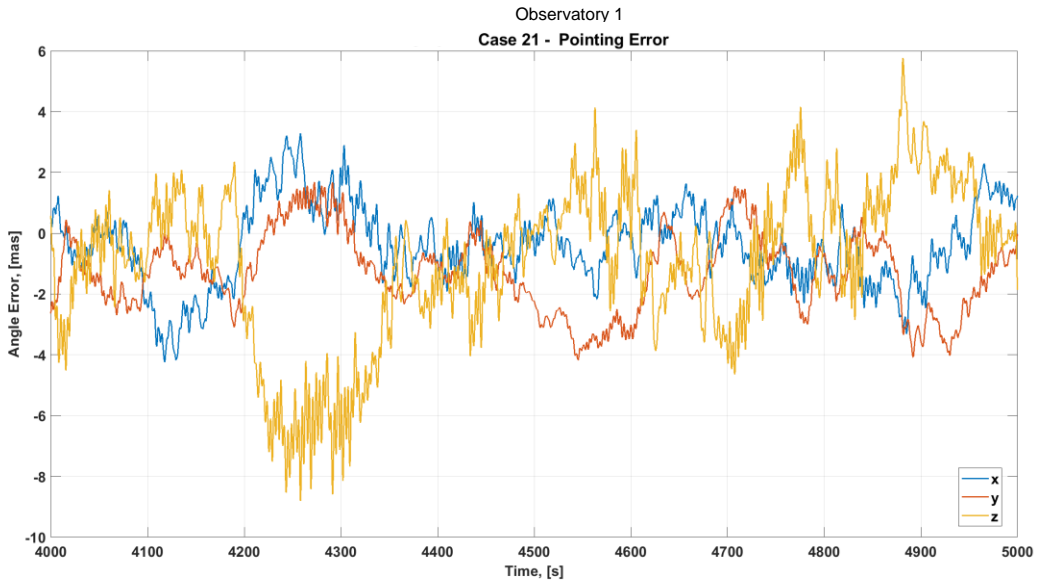

Figure A.1-30. Case 30 Steady-State Pointing Error in mas

- Slew by RWA to [-5,10,15] deg; transition to cold gas thruster fine pointing.
- 100 RPM wheel speed bias held at transition.
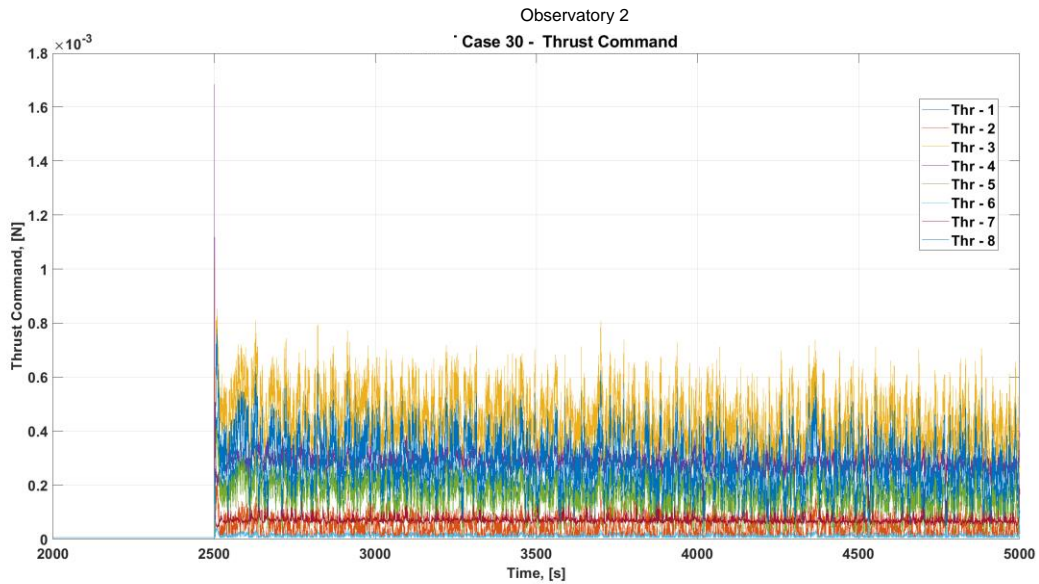
Figure A.1-31. Case 30 Thrust Command

A.2   Observatory 2 with Isolator

Case 9: Reaction Wheel Pointing
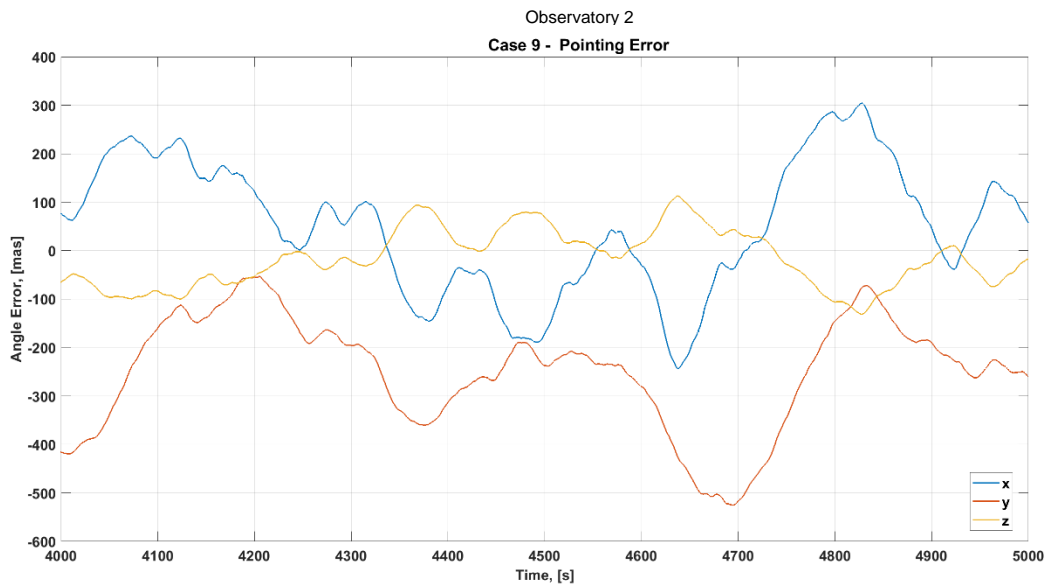
Figure A.2-1. Case 9 with Isolator Steady-State Pointing Error in mas

- No slew.
- Reaction wheel fine pointing only with 100 RPM bias; micro-thrusters off.
- With isolator.

Case 11: Colloid Thruster Pointing with Constant Wheel Speed

Observatory 2
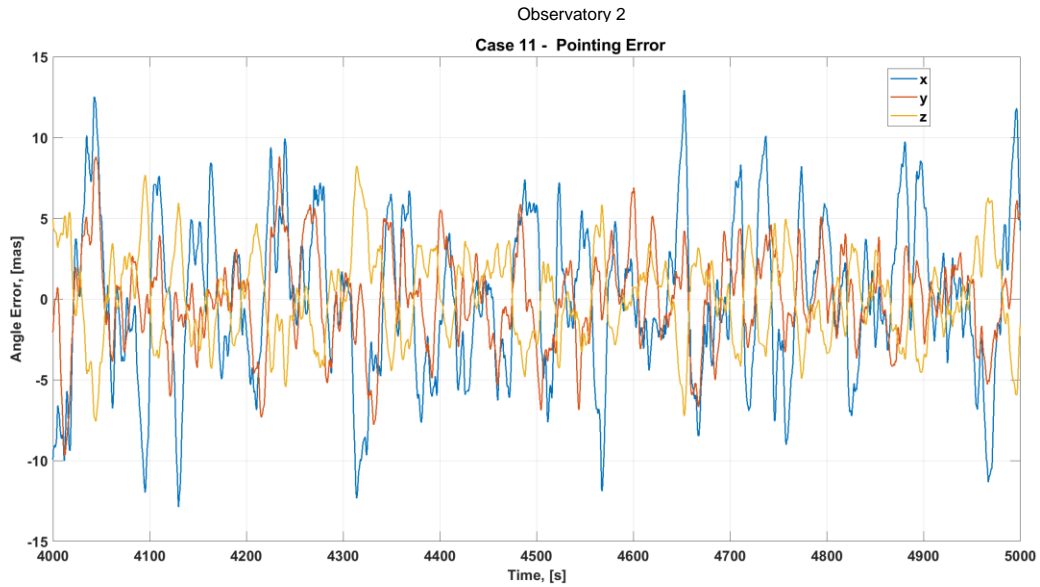
Figure A.2-2. Case 11 with Isolator Steady-State Pointing Error in mas

- No slew.
- Colloid micro-thrusters for fine pointing only; 100 RPM wheel bias.
- With isolator.

Observatory 2
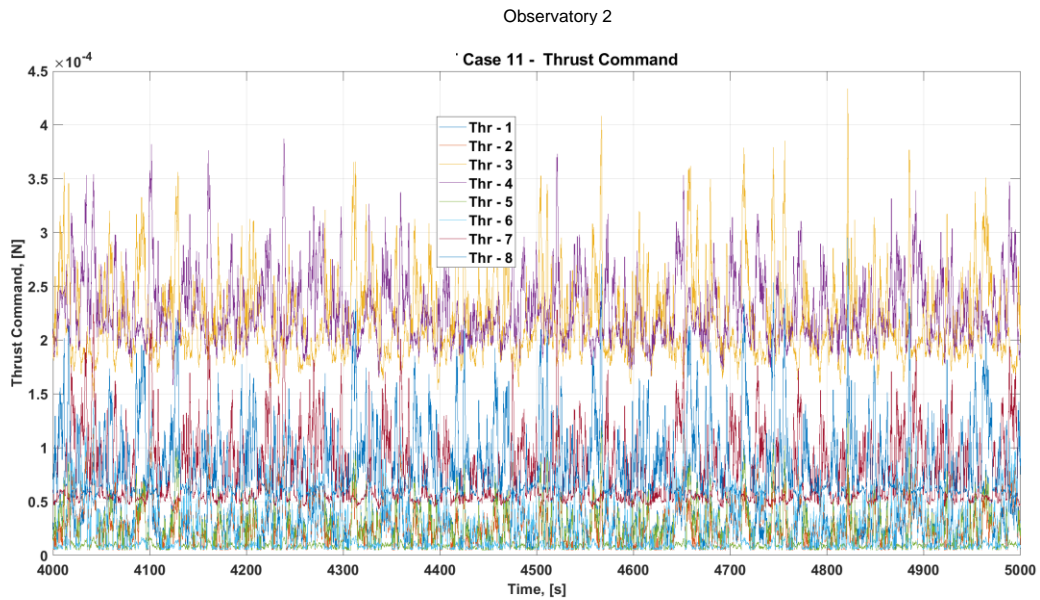
Figure A.2-3. Case 11 with Isolator Steady-State Thrust Command

Case 12: Simultaneous RWA and Colloid Thruster Pointing

Observatory 2
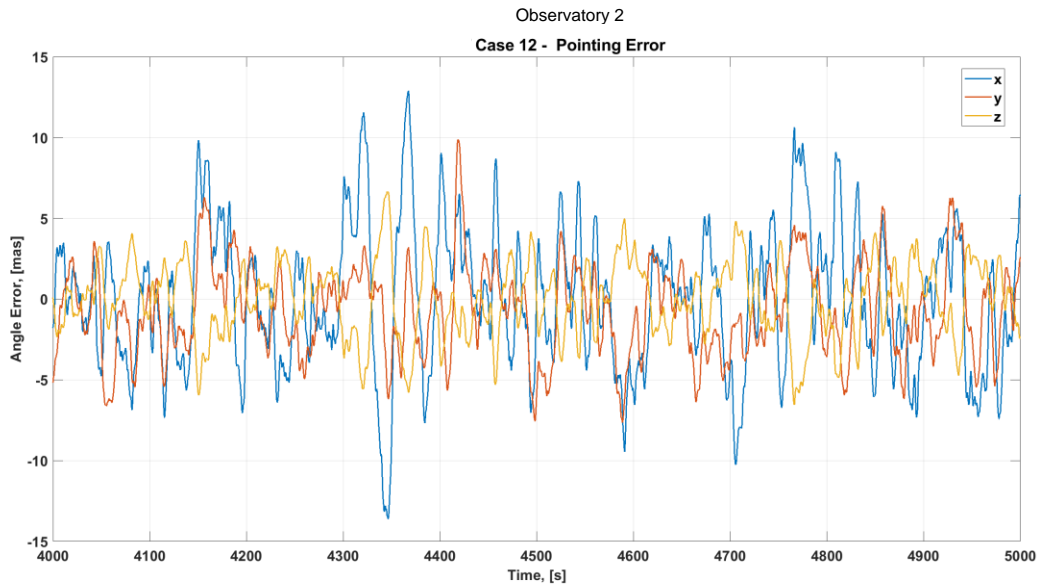
Figure A.2-4. Case 12 with Isolator Steady-State Pointing Error in mas

- No slew.
- Colloid micro-thrusters and RWA used for fine pointing; 100 RPM wheel bias.
- With isolator.

Observatory 2
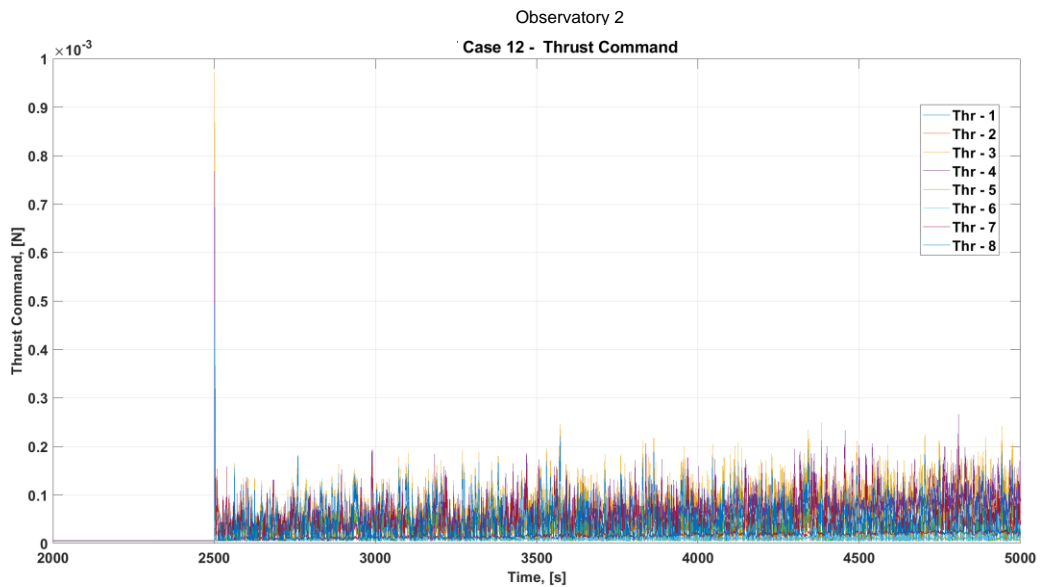
Figure A.2-5. Case 12 with Isolator Thrust Command

Case 13: Cold Gas Thruster Pointing with Constant Wheel Speed
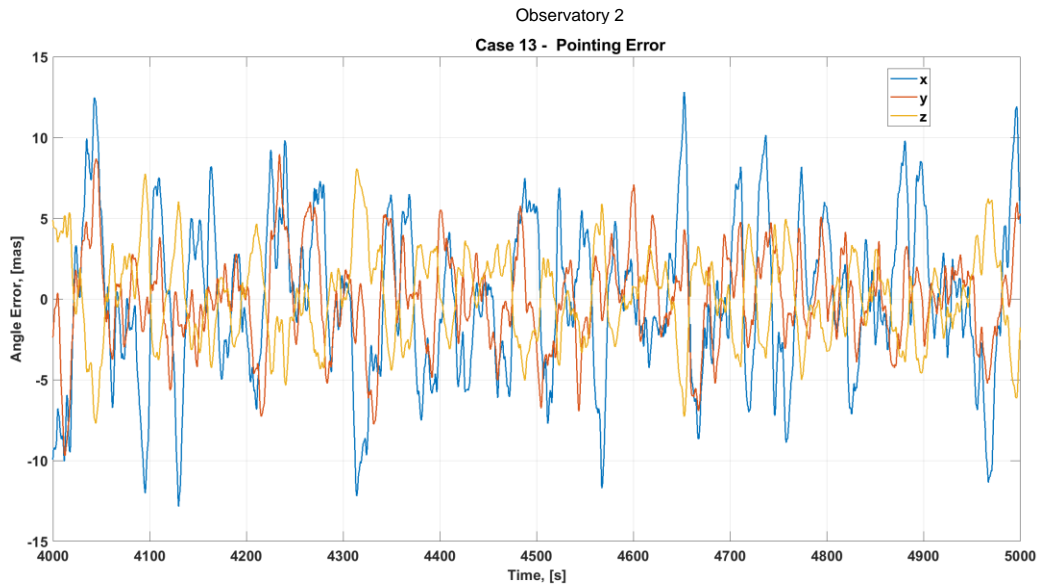
Figure A.2-6. Case 13 with Isolator Steady-State Pointing Error in mas

- No slew.
- Cold gas micro-thrusters for fine pointing only; 100 RPM wheel bias.
- With isolator.
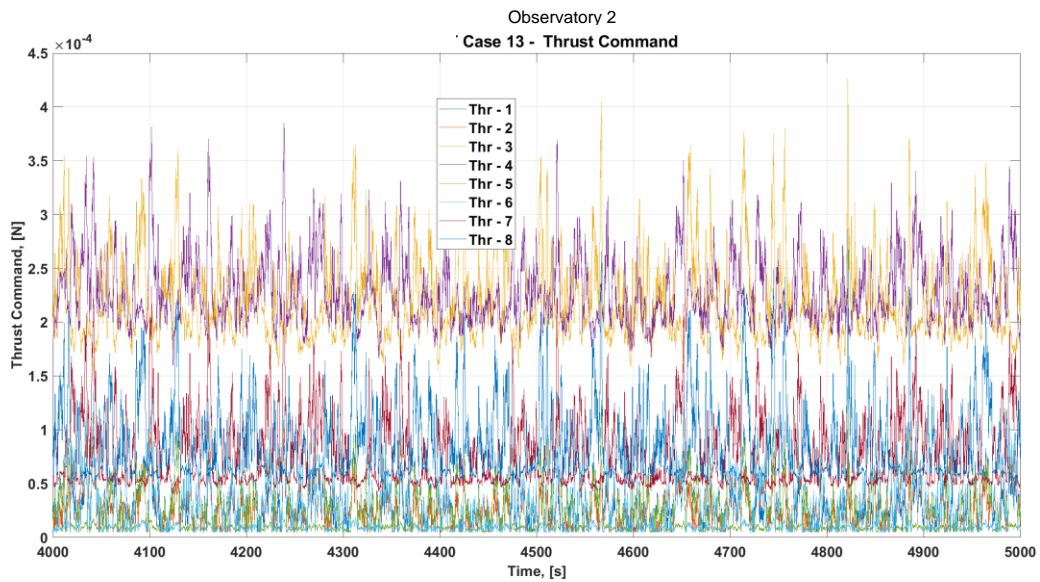
Figure A.2-7. Case 13 with Isolator Steady-State Thrust Command

Case 14: Simultaneous RWA and Cold Gas Thruster Pointing
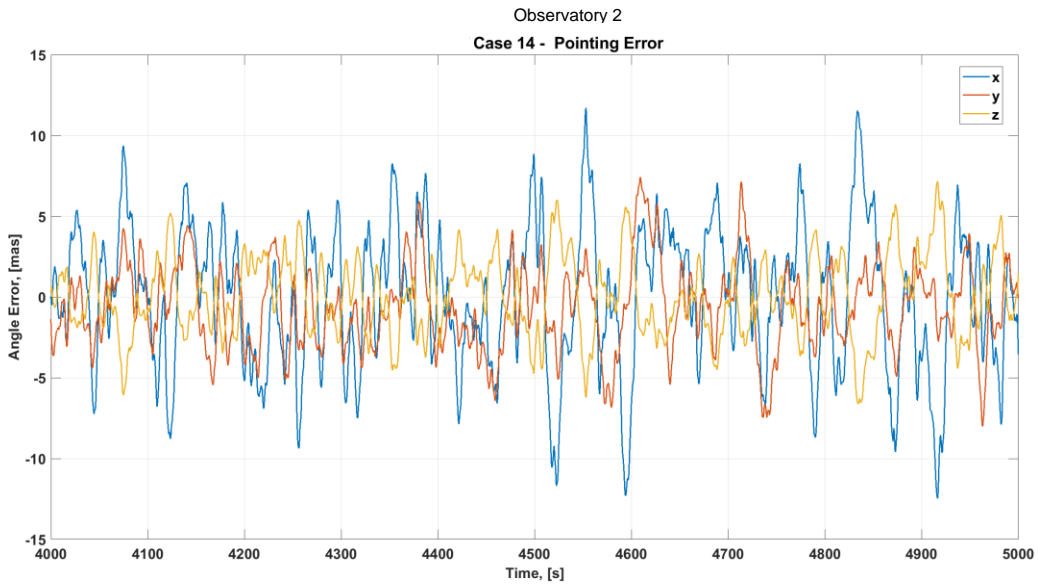
Figure A.2-8. Case 14 with Isolator Steady-State Pointing Error in mas

- No slew.
- Cold gas micro-thrusters and RWA used for fine pointing; 100 RPM wheel bias.
- With isolator.
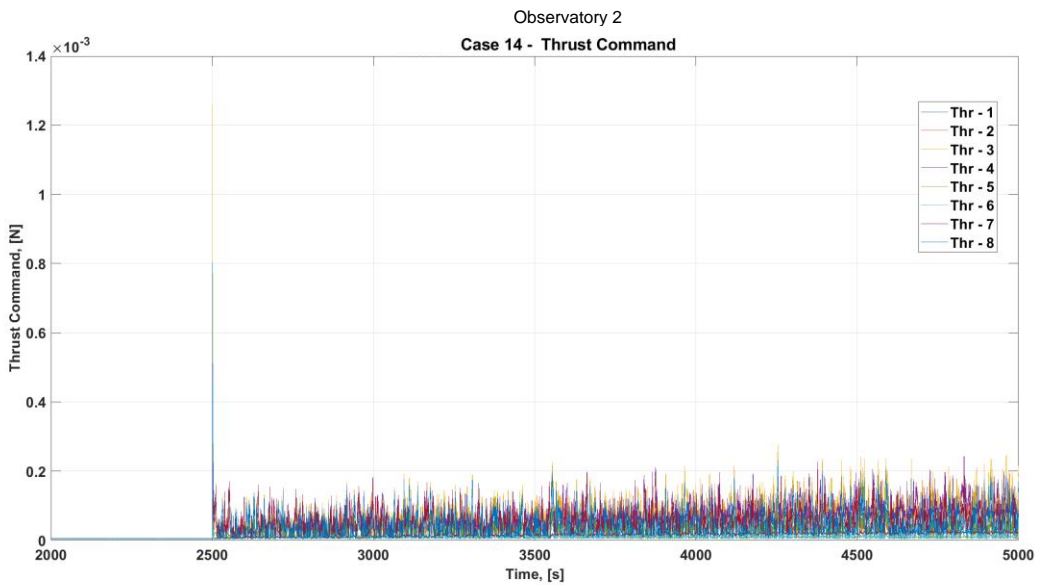
Figure A.2-9. Case 14 with Isolator Thrust Command

A.3   Observatory 1

Case 1: Colloid Thruster Pointing

Figure A.3-1. Case 1 Steady-State Pointing Error in mas

- No slew.
- Colloid micro-thrusters for fine pointing only; wheels off.

Figure A.3-2. Case 1 Steady-State Thrust Command

Case 2: Reaction Wheel Pointing

Figure A.3-3. Case 2 Steady-State Pointing Error in mas

- No slew.
- Reaction wheel fine pointing only with 100 RPM bias; micro-thrusters off.

Case 3: Cold Gas Thruster Pointing

Figure A.3-4. Case 3 Steady-State Pointing Error in mas

- No slew.
- Cold gas micro-thrusters for fine pointing only; wheels off.

Case 3 - Thrust Command

Figure A.3-5. Case 3 Steady-State Thrust Command

Case 4: Colloid Thruster Pointing with Constant Wheel Speed

Case 4 - Pointing Error

Figure A.3-6. Case 4 Steady-State Pointing Error in mas

- No slew.
- Colloid micro-thrusters for fine pointing only; 100 RPM wheel bias..

Observatory 1

Figure A.3-7. Case 4 Steady-State Thrust Command

Case 5: Simultaneous RWA and Colloid Thruster Pointing

Observatory 1

Figure A.3-8. Case 5 Steady-State Pointing Error in mas

- No slew.
- Colloid micro-thrusters and RWA used for fine pointing; 100 RPM wheel bias.

Figure A.3-9. Case 5 Thrust Command

Case 6: Cold Gas Thruster Pointing with Constant Wheel Speed

Figure A.3-10. Case 6 Steady-State Pointing Error in mas

- No slew.
- Cold gas micro-thrusters for fine pointing only; 100 RPM wheel bias.

Figure A.3-11. Case 6 Steady-State Thrust

Case 7: Simultaneous RWA and Cold Gas Thruster Pointing

Figure A.3-12. Case 7 Steady-State Pointing Error in mas

- No slew.
- Cold gas micro-thrusters and RWA used for fine pointing; 100 RPM wheel bias.

Case 7 - Thrust Command

Figure A.3-13. Case 7 Thrust Command

Case 15: RCS Thruster Slew to Colloid Thruster Pointing

Case 15 - Pointing Error

Figure A.3-14. Case 15 Steady-State Pointing Error in mas

- Slew by RCS thrusters to [-5,10,15] deg; transition to colloid thruster pointing.
- Wheels off.

Figure A.3-15. Case 15 Thrust Command

Case 17: RWA Slew to Colloid Thruster Pointing (Zero Wheel Speed Bias)

Figure A.3-16. Case 17 Steady-State Pointing Error in mas

- Slew by RWA to [-5,10,15] deg; transition to colloid thruster fine pointing.
- 0 RPM wheel speed bias.
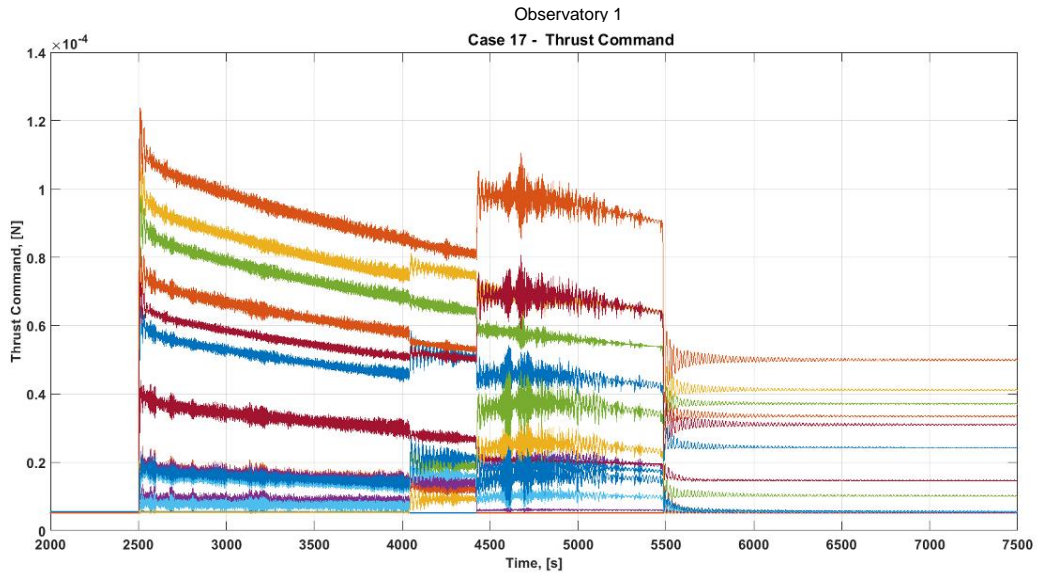
Figure A.3-17. Case 17 Thrust Command

Figure A.3-18. Case 17 Wheel Speed

Case 19: RWA Slew to Simultaneous Colloid Pointing

Observatory 1

Figure A.3-19. Case 19 Steady-State Pointing Error in mas

- Slew by RWA to [-5,10,15] deg; transition to simultaneous colloid thruster fine pointing.
- 100 RPM wheel speed bias.

Observatory 1

Figure A.3-20. Case 19 Thrust Command

Case 21: RWA Slew to Colloid Thruster Pointing (Wheel Speed Hold)

Figure A.3-21. Case 21 Steady-State Pointing Error in mas

- Slew by RWA to [-5,10,15] deg; transition to colloid thruster fine pointing.
- 100 RPM wheel speed bias held at transition.
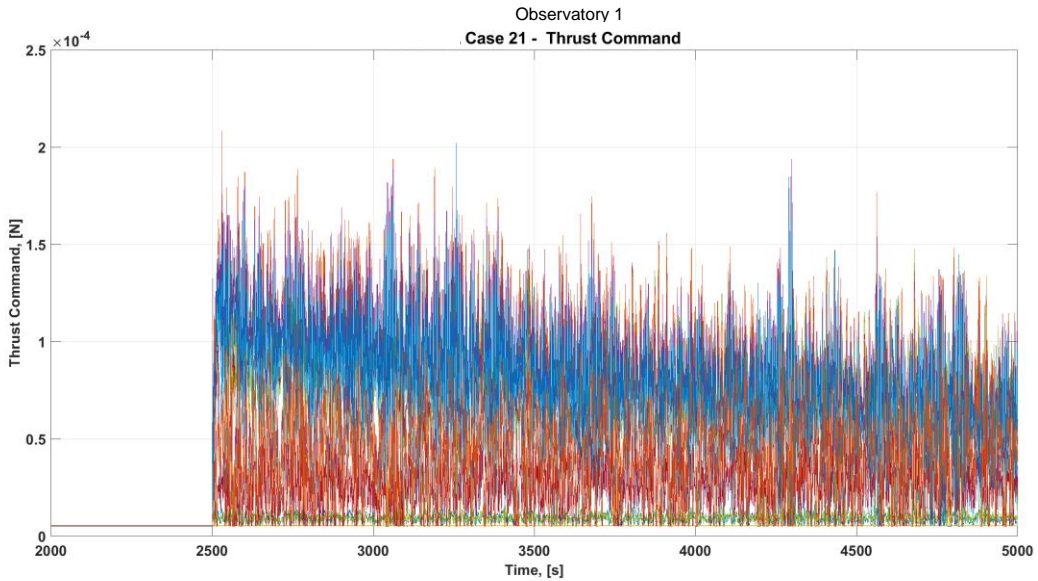
Figure A.3-22. Case 21 Thrust Command

Case 23: RCS Thruster Slew to Cold Gas Thruster Pointing
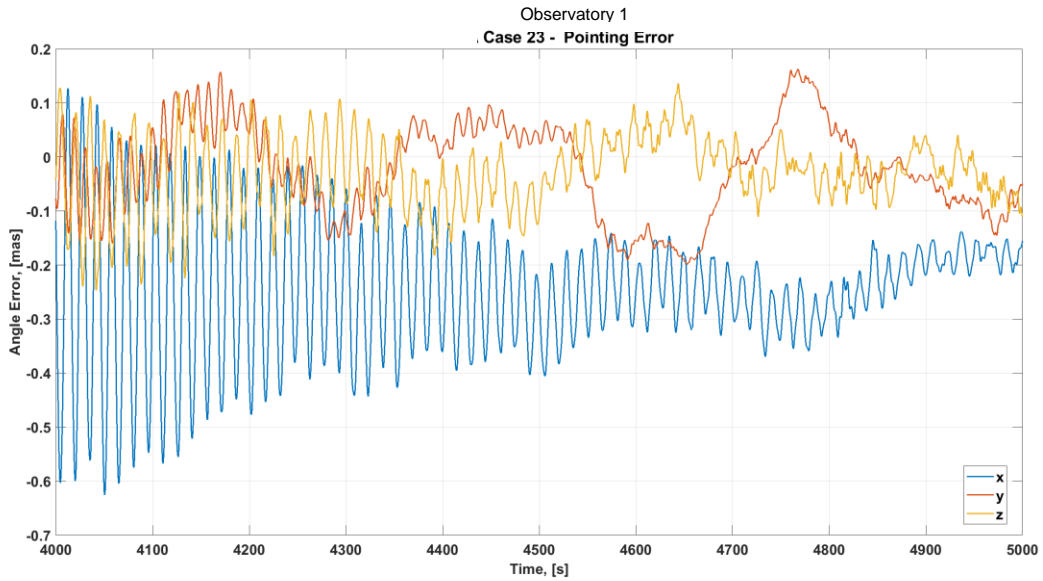
Figure A.3-23. Case 23 Steady-State Pointing Error in mas

- Slew by RCS thrusters to [-5,10,15] deg; transition to cold gas thruster pointing.
- Wheels off.
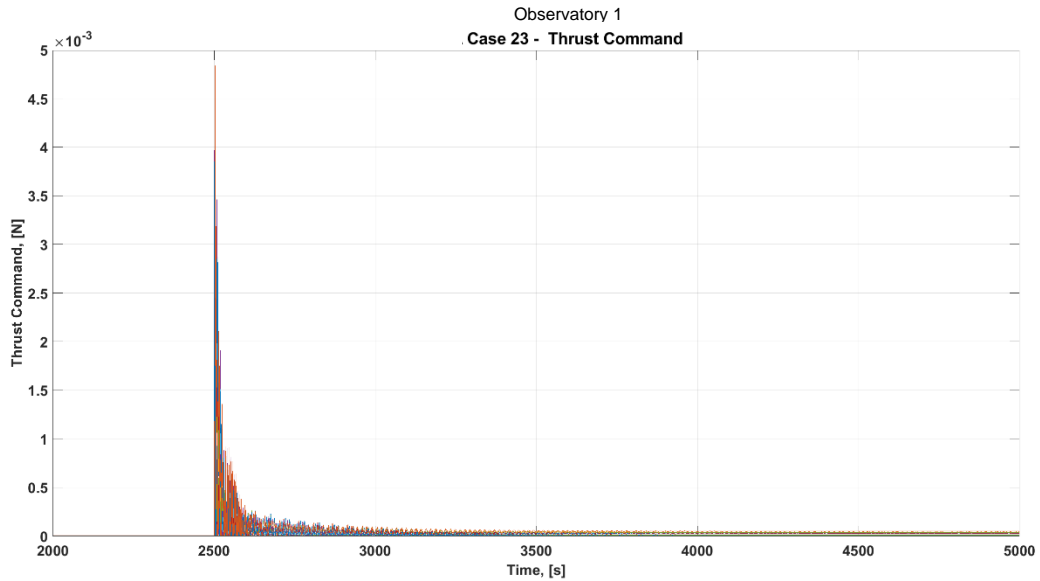
Figure A.3-24. Case 23 Thrust Command

Case 25: RWA Slew to Cold Gas Thruster Pointing (Zero Wheel Speed Bias)
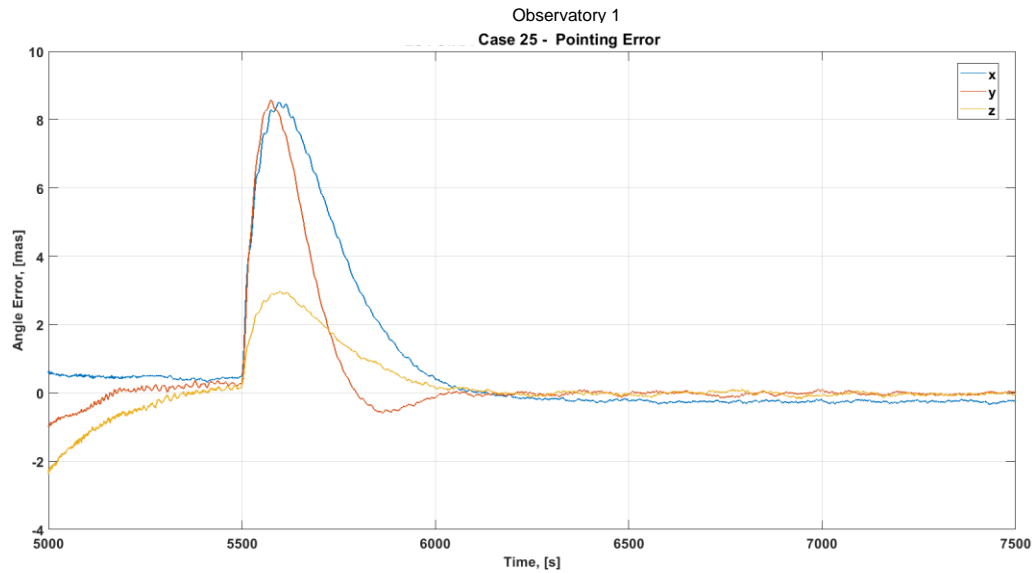
Figure A.3-25. Case 25 Steady-State Pointing Error in mas

- Slew by RWA to [-5,10,15] deg; transition to cold gas thruster fine pointing.
- 0 RPM wheel speed bias.
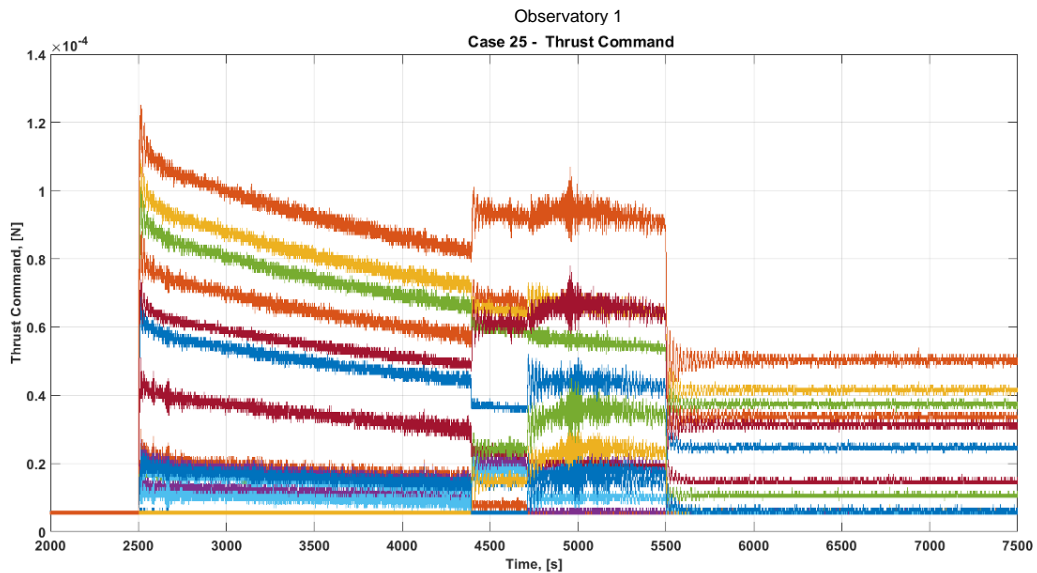
Figure A.3-26. Case 25 Thrust Command

Observatory 1
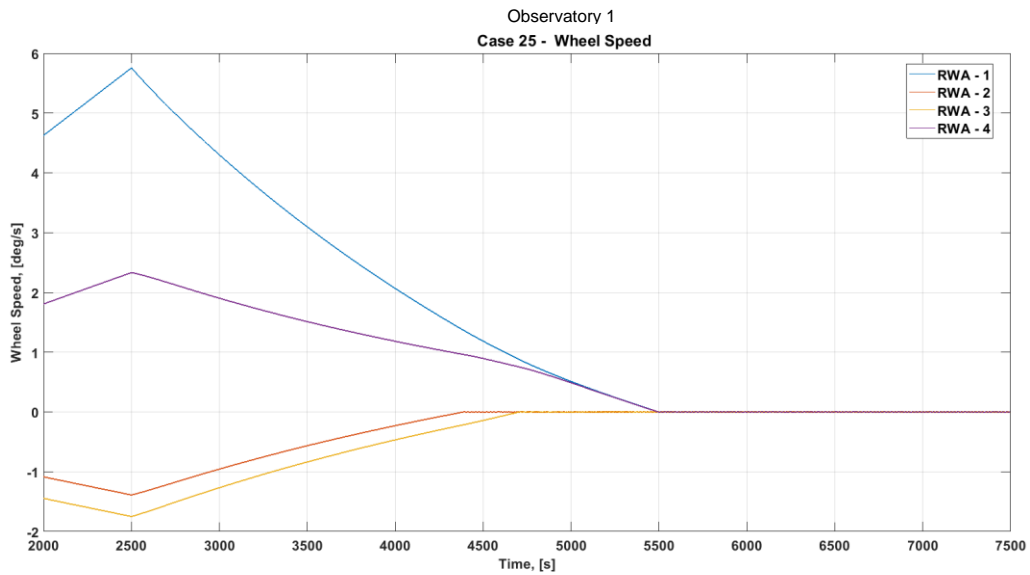
Figure A.3-27. Case 25 Wheel Speed

Case 27: RWA Slew to Simultaneous Cold Gas Pointing

Observatory 1
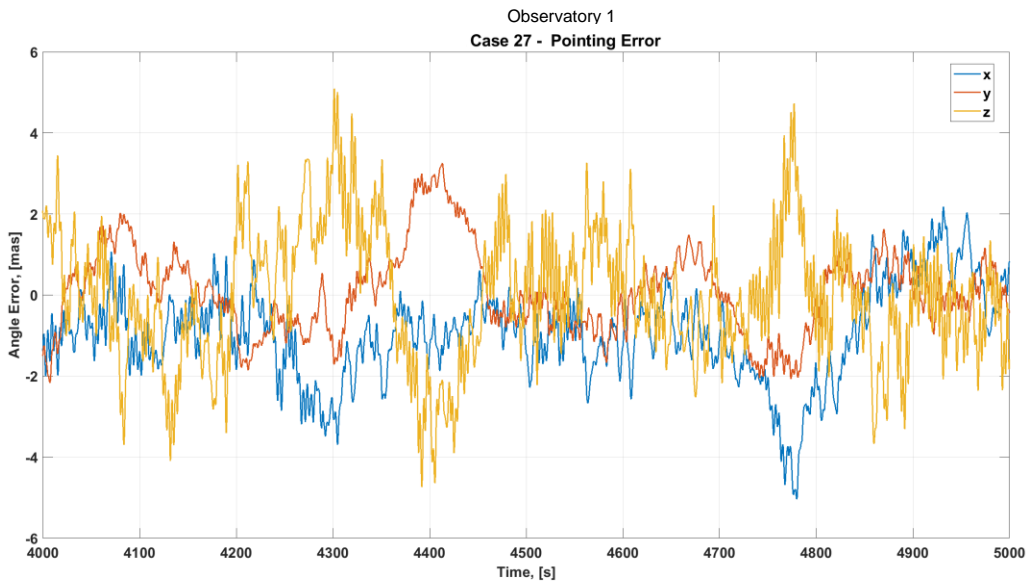
Figure A.3-28. Case 27 Steady-State Pointing Error in mas

- Slew by RWA to [-5,10,15] deg; transition to simultaneous cold gas thruster fine pointing.
- 100 RPM wheel speed bias.
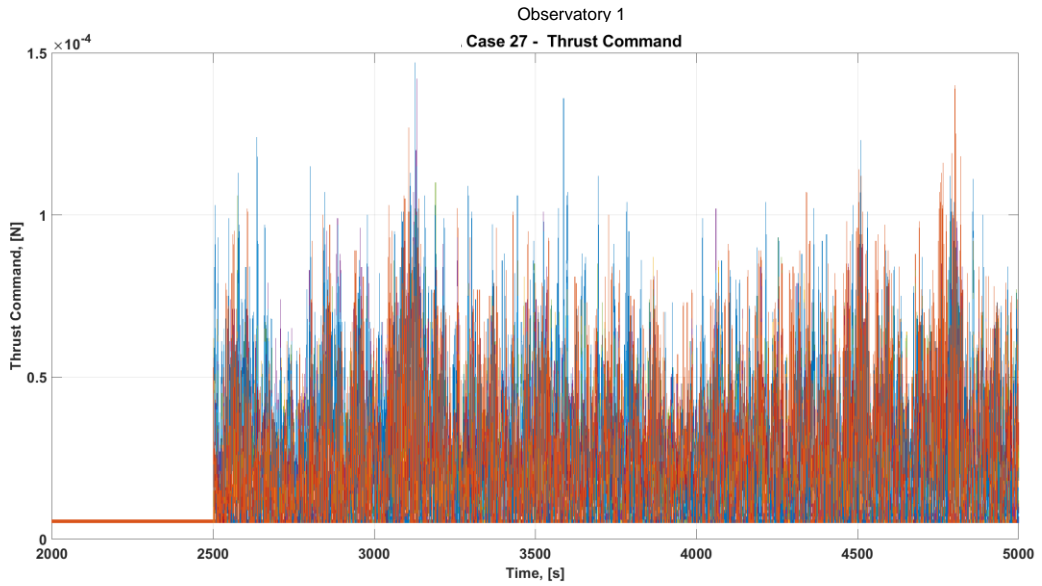
Figure A.3-31. Case 27 Thrust Command

Case 29: RWA Slew to Cold Gas Thruster Pointing (Wheel Speed Hold)
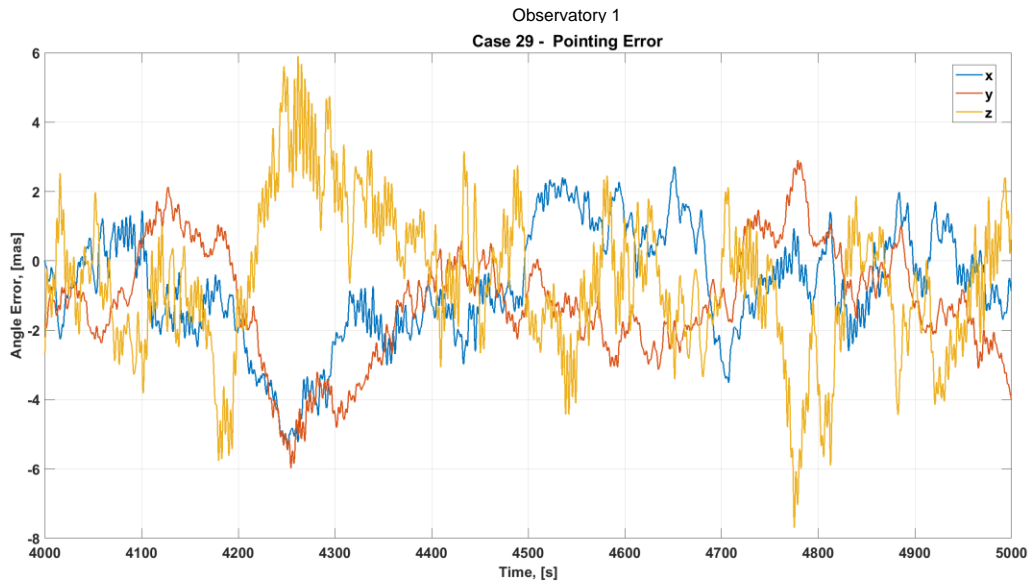
Figure A.3-29. Case 29 Steady-State Pointing Error in mas

- Slew by RWA to [-5,10,15] deg; transition to cold gas thruster fine pointing.
- 100 RPM wheel speed bias held at transition.
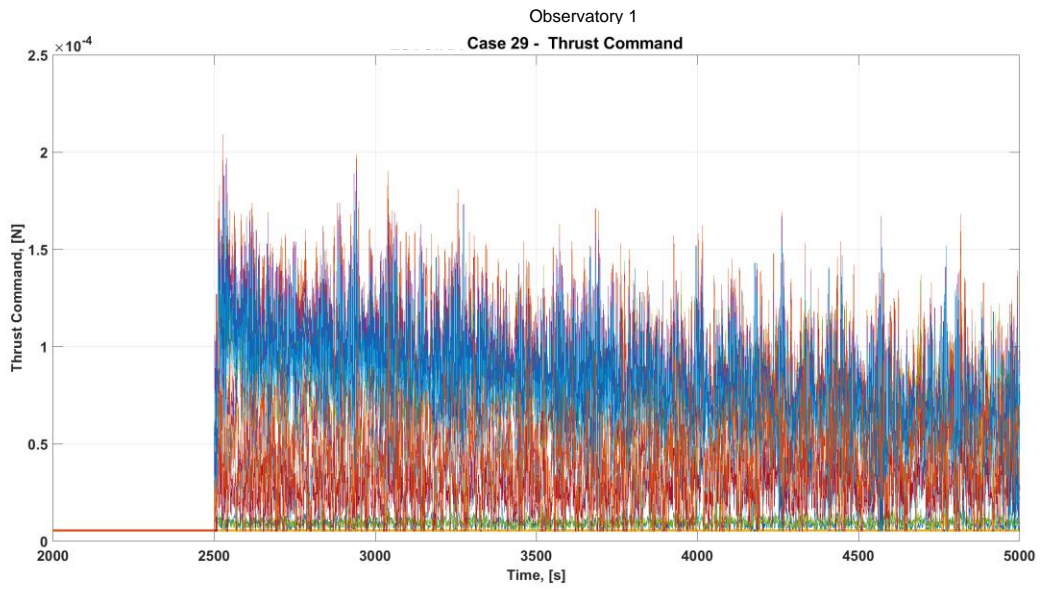
Figure A.3-30. Case 29 Thrust Commands

Appendix B: Bode and Nichols Plots for Micro-Thruster and Reaction Wheel Control

Observatory 1 Micro-Thruster Bode and Nichols Plots
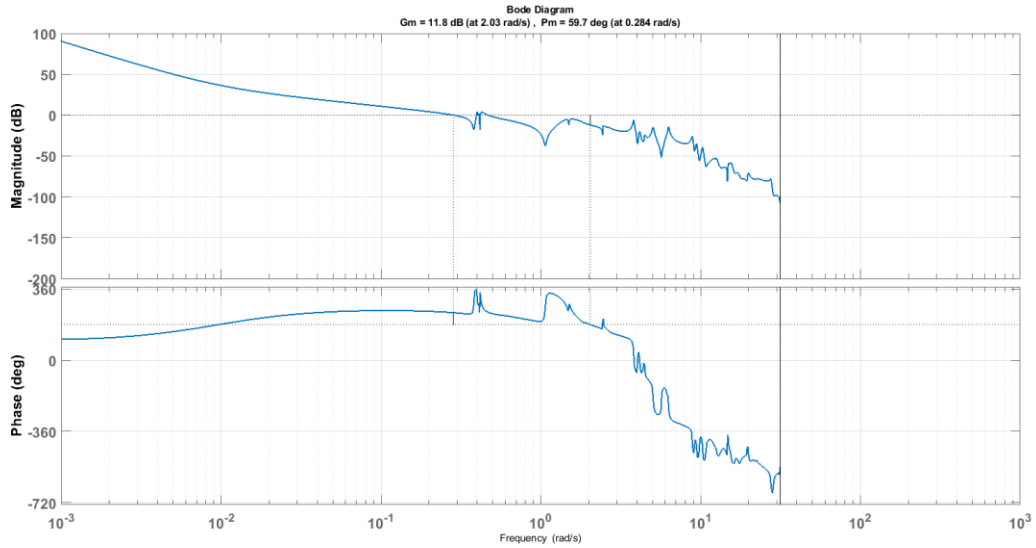
Figure B-1. Observatory 1 Micro-Thruster X-axis Bode Plot
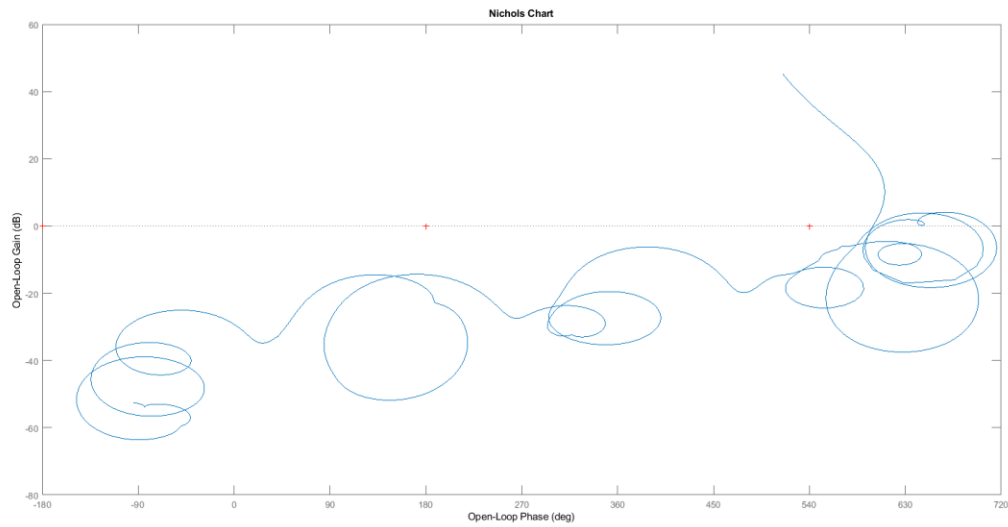
Figure B-2. Observatory 1 Micro-Thruster X-axis Nichols Plot
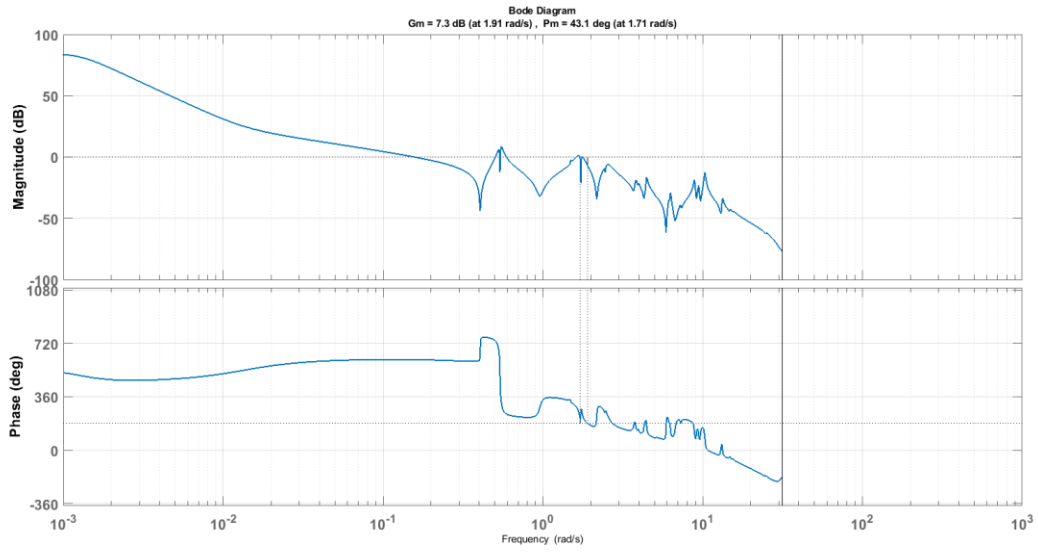
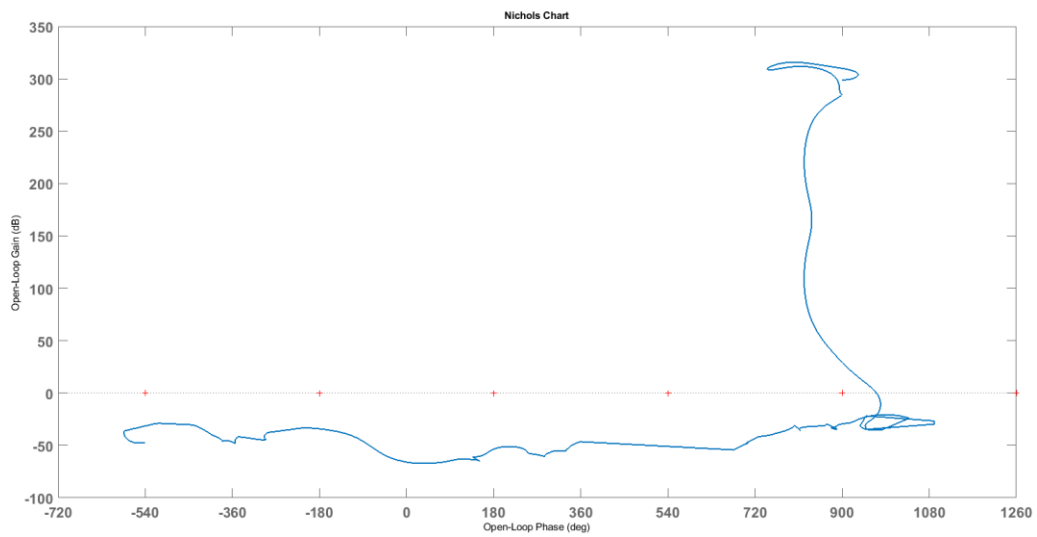*Figure B-3. Observatory 1 Micro-Thruster Y-axis Bode Plot*
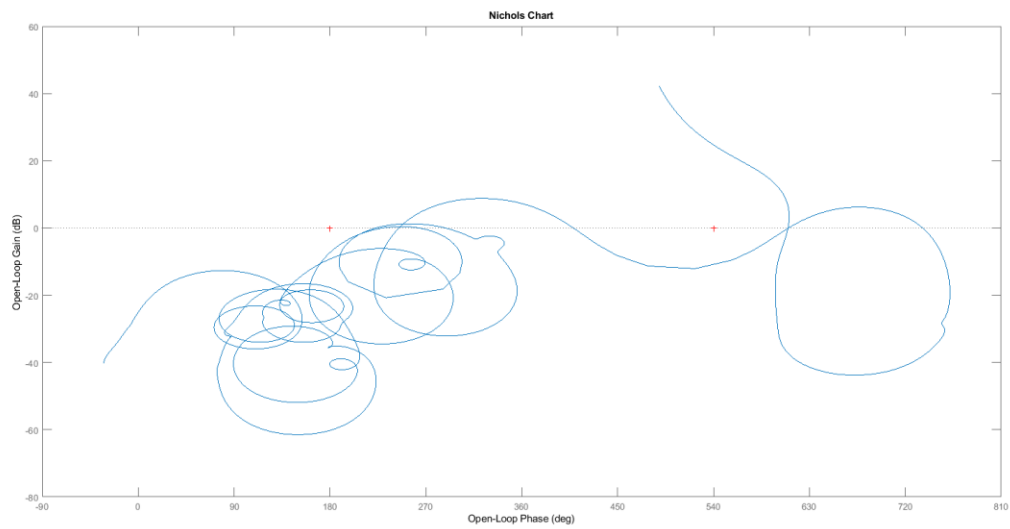
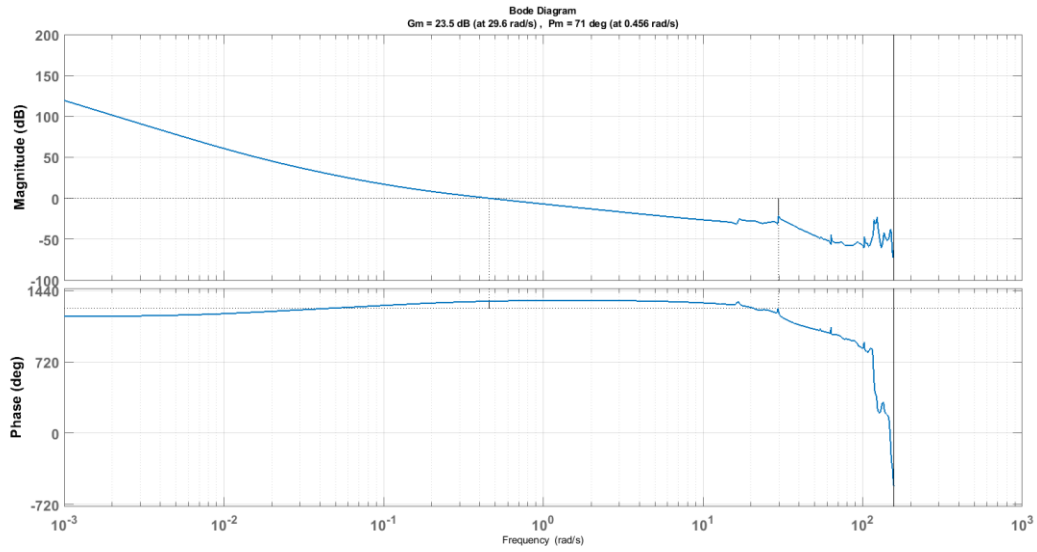*Figure B-4. Observatory 1 Micro-Thruster Y-axis Nichols Plot*
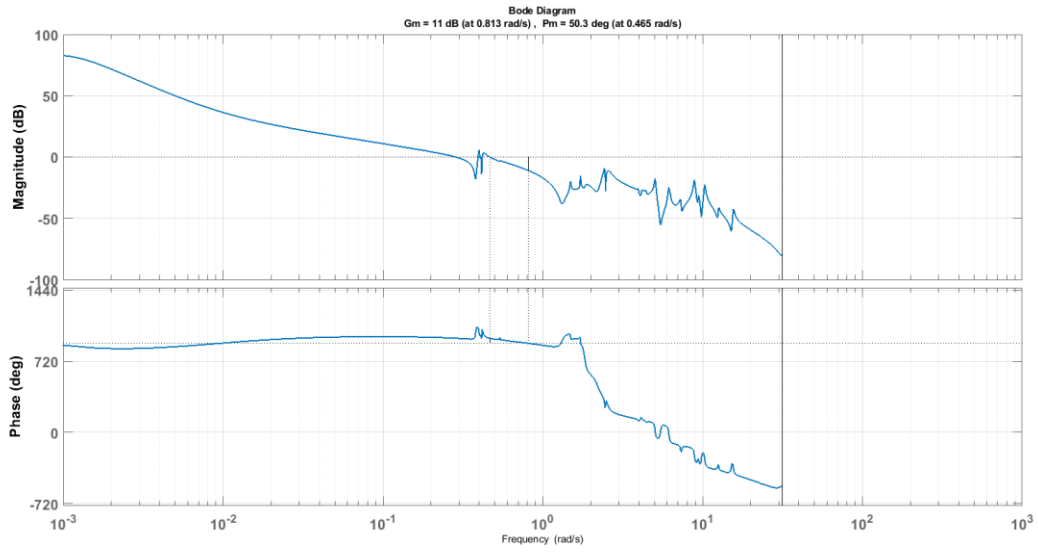
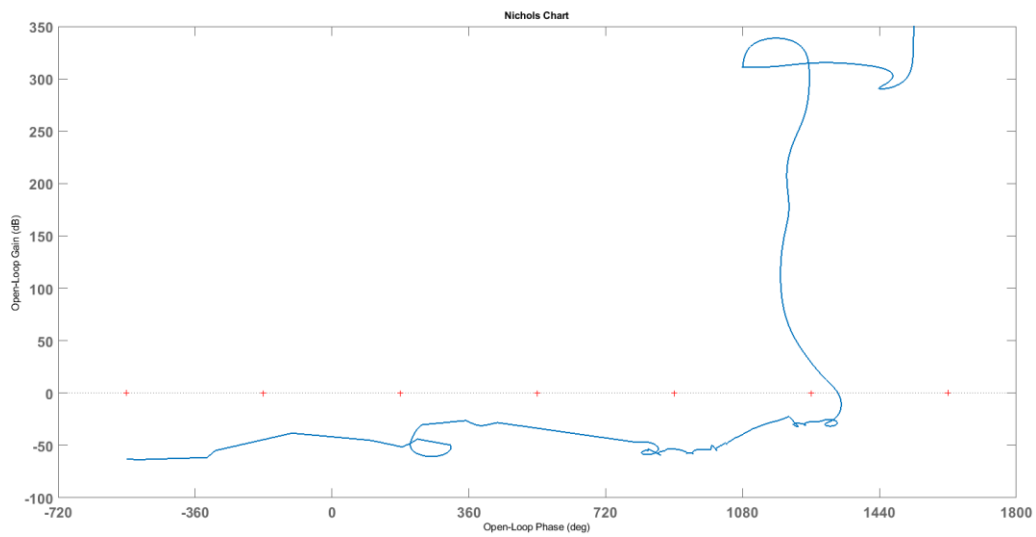*Figure B-5. Observatory 1 Micro-Thruster Z-axis Bode Plot*
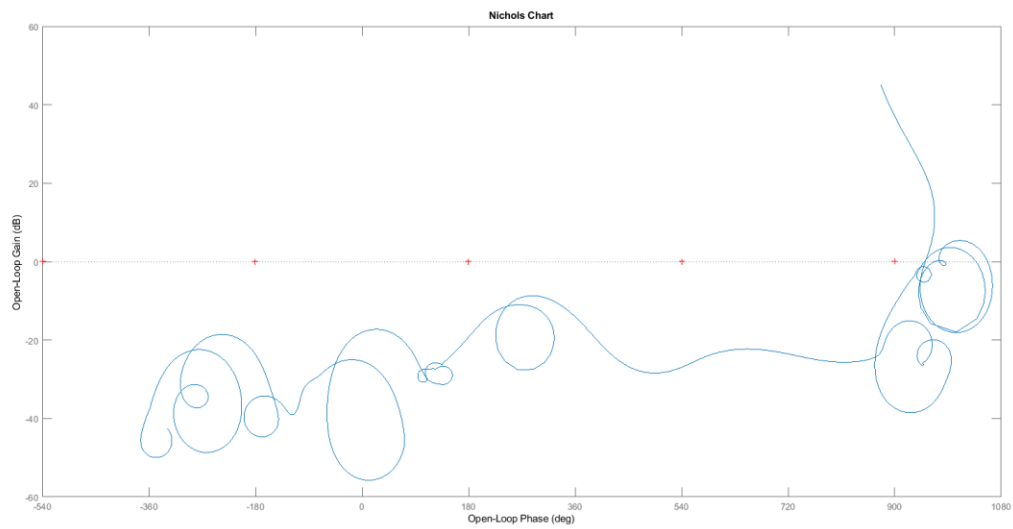
Figure B-6. Observatory 1 Micro-Thruster Z-axis Nichols Plot

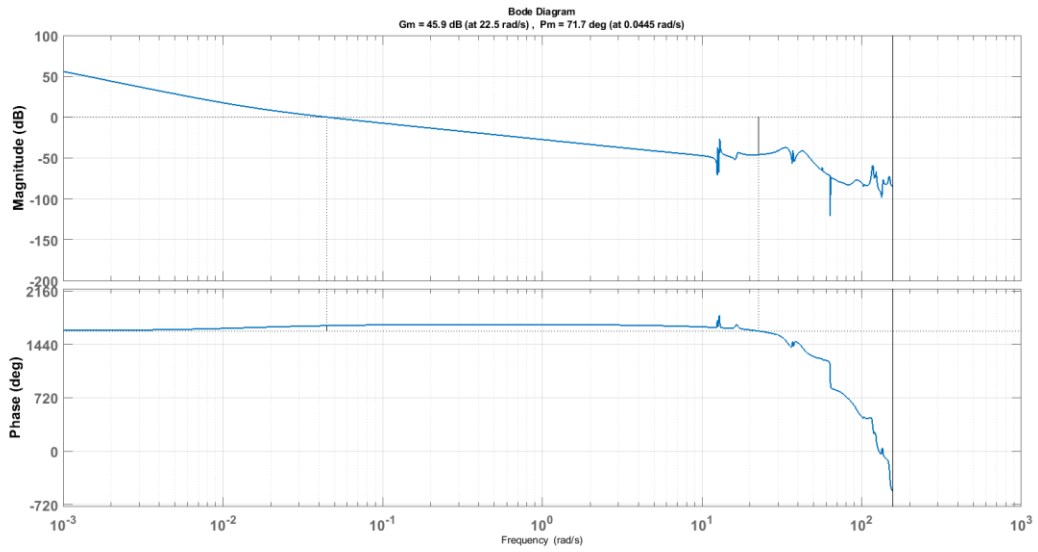# Observatory 1 Reaction Wheel Bode and Nichols Plots
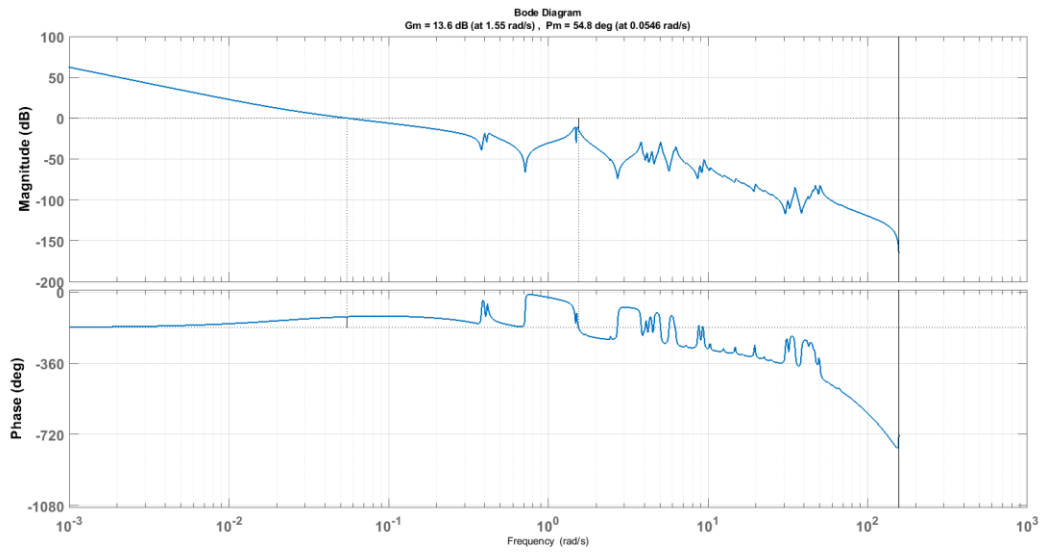
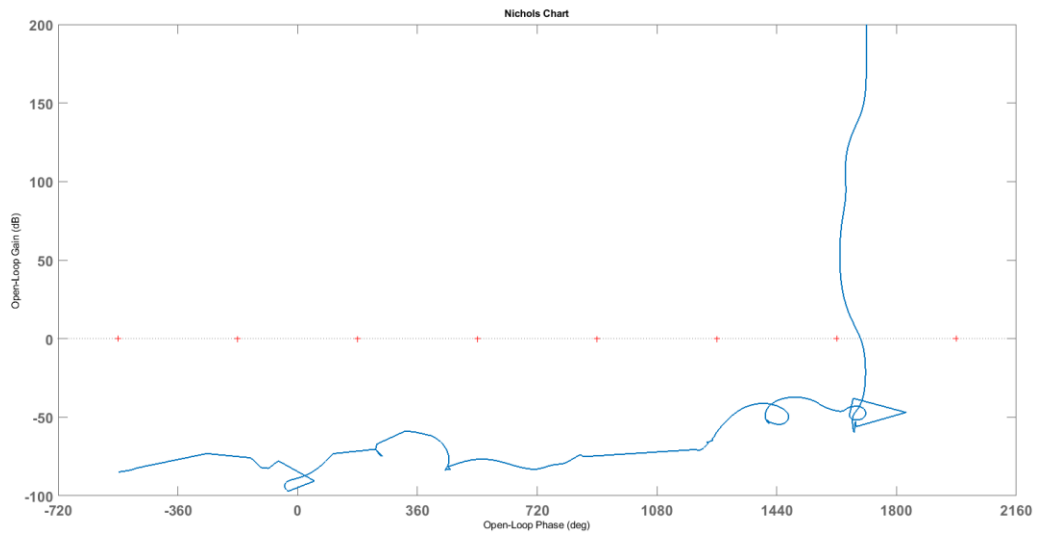
Figure B-7. Observatory 1 Reaction Wheel X-axis Bode Plot
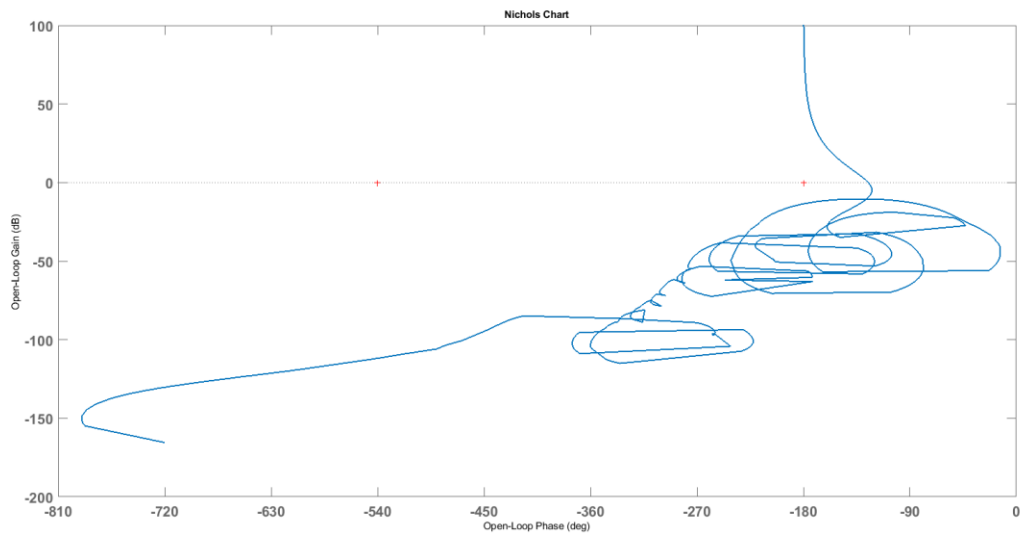
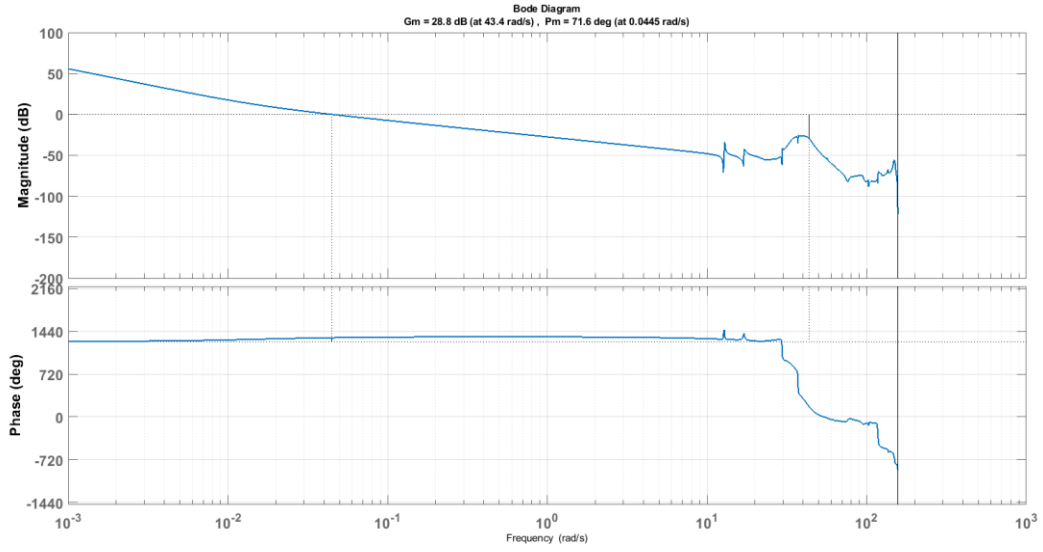*Figure B-8. Observatory 1 Reaction Wheel X-axis Nichols Plot*
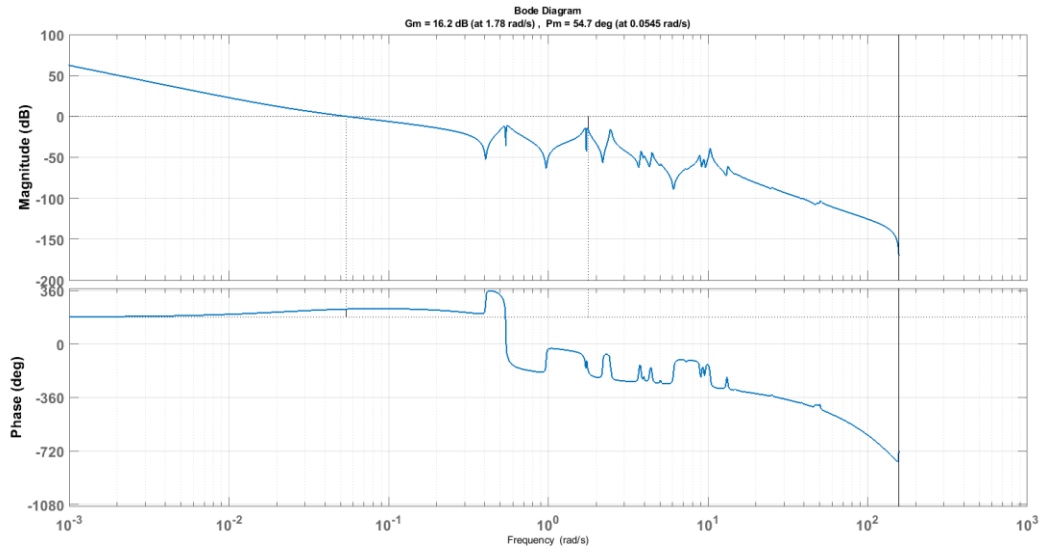
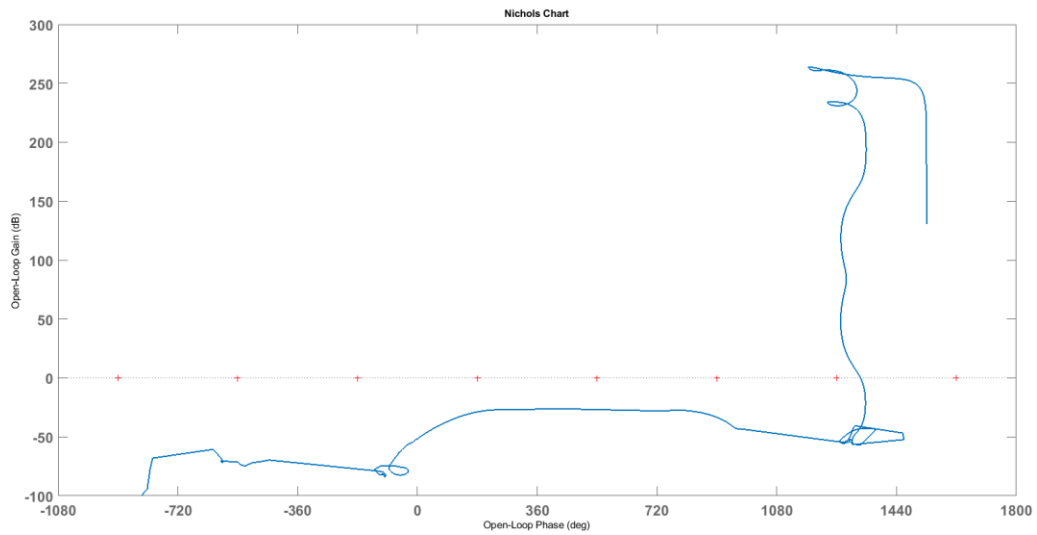***Figure B-9. Observatory 1 Reaction Wheel Y-axis Bode Plot***
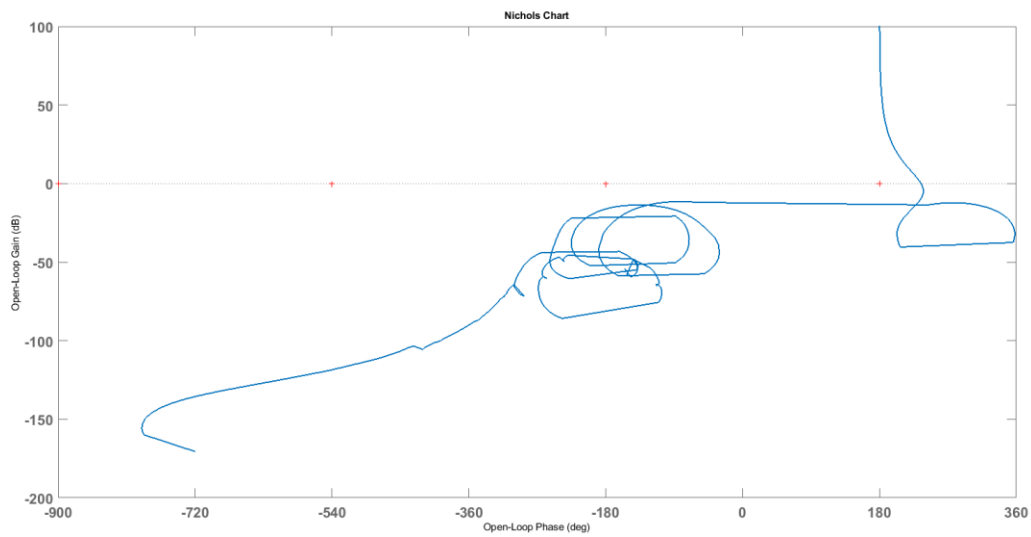
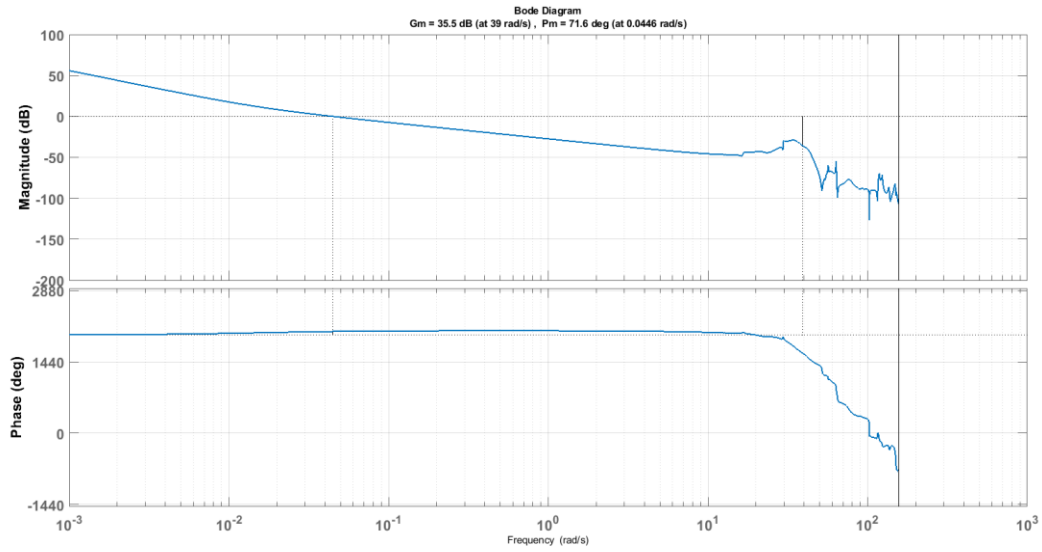***Figure B-10. Observatory 1 Reaction Wheel Y-axis Nichols Plot***
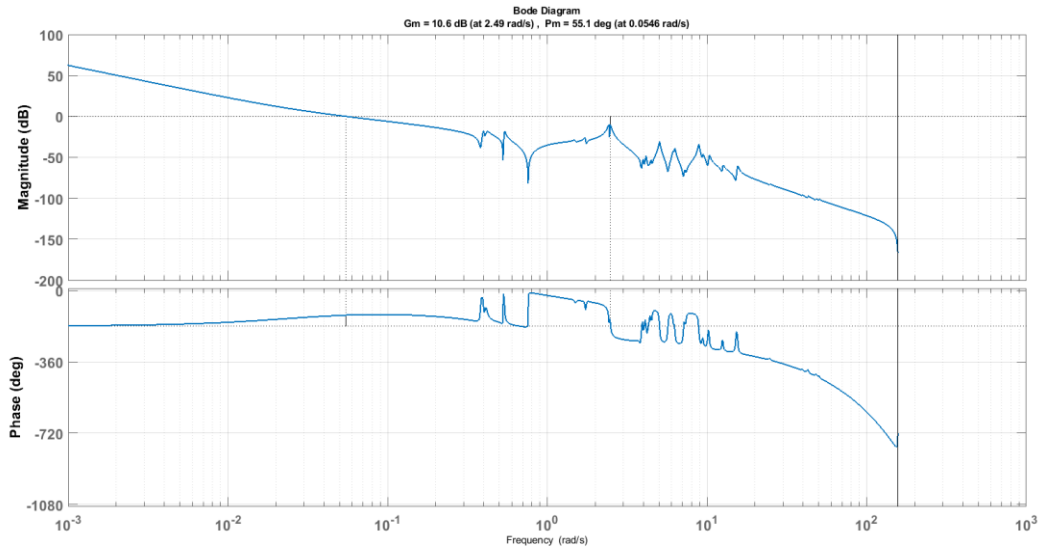
Figure B-11. Observatory 1 Reaction Wheel Z-axis Bode Plot
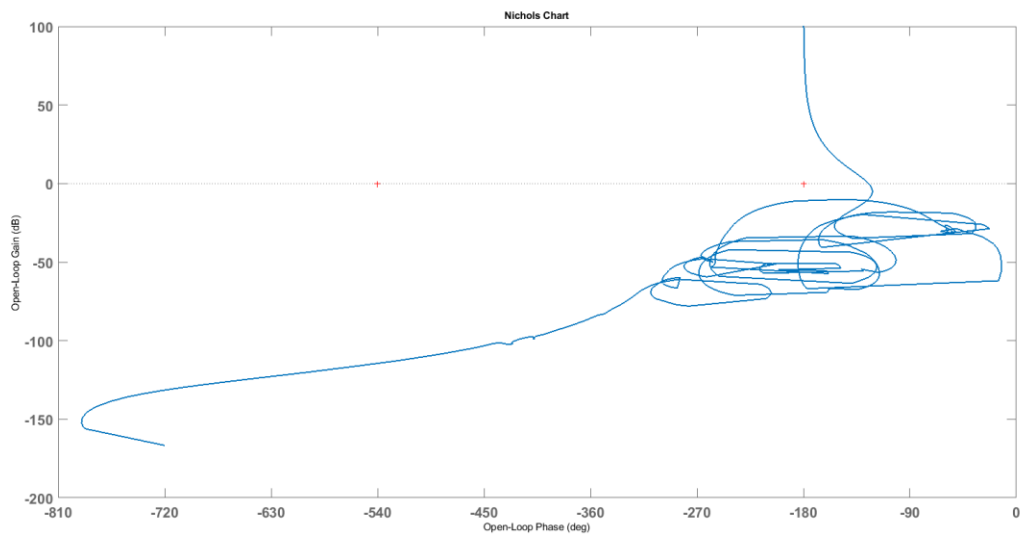
Figure B-12. Observatory 1 Reaction Wheel Z-axis Nichols Plot

Observatory 2 Micro-Thruster Bode and Nichols Plots
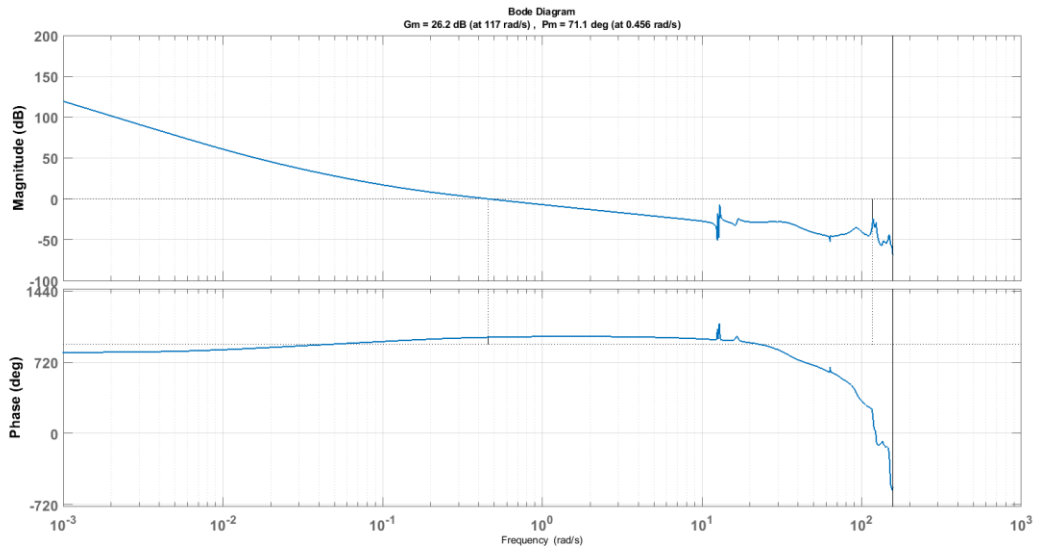
Figure B-13. Observatory 2 Micro-Thruster X-axis Bode Plot
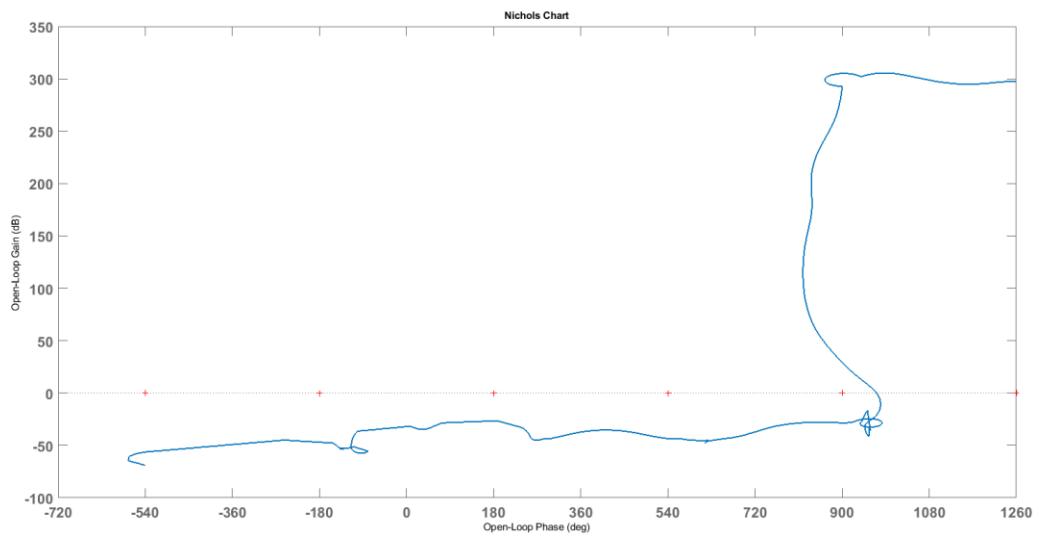
Figure B-14. Observatory 2 Micro-Thruster X-axis Nichols plot
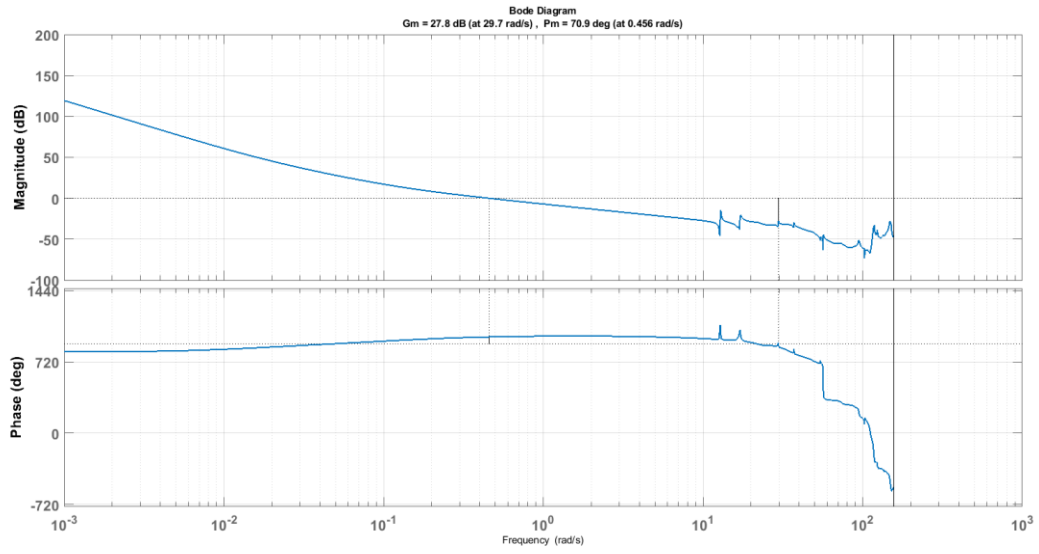
Figure B-15. Observatory 2 Micro-Thruster Y-axis Bode Plot

Figure B-16. Observatory 2 Micro-Thruster Y-axis Nichols Plot

Figure B-17. Observatory 2 Micro-Thruster Z-axis Bode Plot

Figure B-18. Observatory 2 Micro-Thruster Z-axis Nichols Plot

Observatory 2 Reaction Wheel Bode and Nichols Plots

Figure B-19. Observatory 2 Reaction Wheel X-axis Bode Plot

Figure B-20. Observatory 2 Reaction Wheel X-axis Nichols Plot

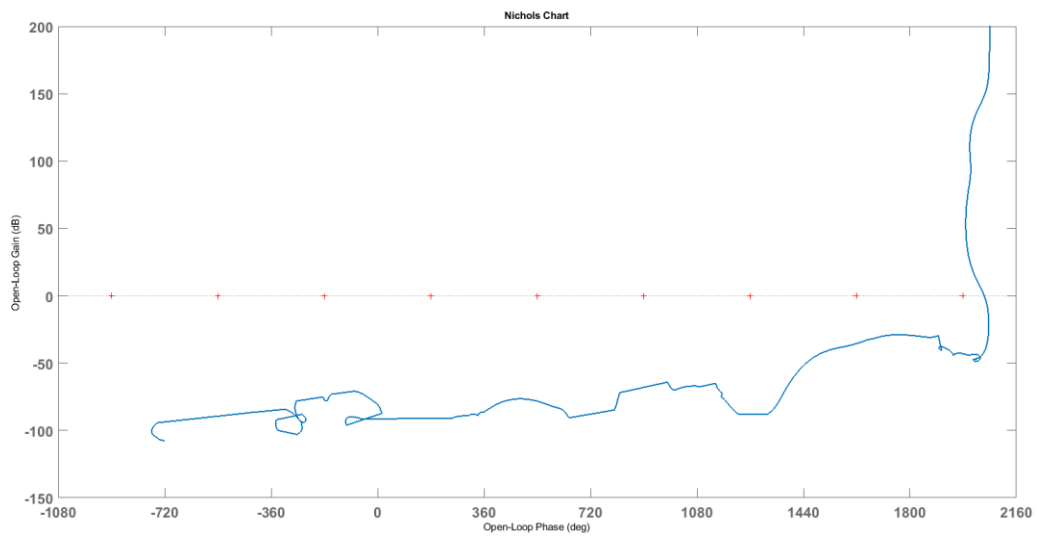***Figure B-21. Observatory 2 Reaction Wheel Y-axis Bode Plot***

Figure B-22. Observatory 2 Reaction Wheel Y-axis Nichols Plot

Figure B-23. Observatory 2 Reaction Wheel Z-axis Bode Plot

Figure B-24. Observatory 2 Reaction Wheel Z-axis Nichols Plot

REPORT DOCUMENTATION PAGE

1. REPORT DATE (DD-MM-YYYY)	2. REPORT TYPE	3. DATES COVERED (From - To)
12/15/2020	Technical Memorandum	

4. TITLE AND SUBTITLE	5a. CONTRACT NUMBER
Application of Micro-Thruster Technology for Space Observatory Pointing Stability	
	5b. GRANT NUMBER
	5c. PROGRAM ELEMENT NUMBER
6. AUTHOR(S)	5d. PROJECT NUMBER
Dennehy, Cornelius J.; Wolf, Aron A.; Chiang, Richard; Stoneking, Eric T.; Ziemer, John K.	
	5e. TASK NUMBER
	5f. WORK UNIT NUMBER
	860921.01.23.01.01

7. PERFORMING ORGANIZATION NAME(S) AND ADDRESS(ES)	8. PERFORMING ORGANIZATION REPORT NUMBER
NASA Langley Research Center Hampton, VA 23681-2199	NESC-RP-18-01375

9. SPONSORING/MONITORING AGENCY NAME(S) AND ADDRESS(ES)	10. SPONSOR/MONITOR'S ACRONYM(S)
National Aeronautics and Space Administration Washington, DC 20546-0001	NASA
	11. SPONSOR/MONITOR'S REPORT NUMBER(S)
	NASA/TM-20205011556

12. DISTRIBUTION/AVAILABILITY STATEMENT

Unclassified - Unlimited
Subject Category 16 Space Transportation and Safety
Availability: NASA STI Program (757) 864-9658

13. SUPPLEMENTARY NOTES

14. ABSTRACT

This assessment was requested by the NASA Engineering and Safety Center (NESC) Guidance, Navigation, and Control (GN&C) Technical Discipline Team (TDT), which identified the topic as an unrecognized critical need for the Agency's future space science observatory-class space platforms. An initial low-fidelity feasibility study of the use of cold-gas micro-thrusters as a replacement for reaction wheels was performed in 2017 as a GN&C TDT discretionary activity. The assessment documented in this final report was initiated in 2018 as a follow-on high-fidelity study.

15. SUBJECT TERMS

Guidance, Navigation, and Control; Micro-Thruster Technology; Space Observatory

16. SECURITY CLASSIFICATION OF:			17. LIMITATION OF ABSTRACT	18. NUMBER OF PAGES	19a. NAME OF RESPONSIBLE PERSON
a. REPORT	b. ABSTRACT	c. THIS PAGE			STI Help Desk (email: help@sti.nasa.gov)
					19b. TELEPHONE NUMBER (Include area code)
U	U	U	UU	105	(443) 757-5802